Fully Passive Wireless Acquisition of Neuropotentials

by

Helen N. Schwerdt

A Dissertation Presented in Partial Fulfillment
of the Requirements for the Degree
Doctor of Philosophy

Approved June 2014 by the
Graduate Supervisory Committee:

Junseok Chae, Chair
Félix A. Miranda
Stephen Phillips
Bruce C. Towe
Constantine A. Balanis
David Frakes

ARIZONA STATE UNIVERSITY

August 2014

ABSTRACT

The ability to monitor electrophysiological signals from the sentient brain is requisite to decipher its enormously complex workings and initiate remedial solutions for the vast amount of neurologically-based disorders. Despite immense advancements in creating a variety of instruments to record signals from the brain, the translation of such neurorecording instrumentation to real clinical domains places heavy demands on their safety and reliability, both of which are not entirely portrayed by presently existing implantable recording solutions. In an attempt to lower these barriers, alternative wireless radar backscattering techniques are proposed to render the technical burdens of the implant chip to entirely passive neurorecording processes that transpire in the absence of formal integrated power sources or powering schemes along with any active circuitry. These radar-like wireless backscattering mechanisms are used to conceive of fully passive neurorecording operations of an implantable microsystem. The fully passive device potentially manifests inherent advantages over current wireless implantable and wired recording systems: negligible heat dissipation to reduce risks of brain tissue damage and minimal circuitry for long term reliability as a chronic implant. Fully passive neurorecording operations are realized via intrinsic nonlinear mixing properties of the varactor diode. These mixing and recording operations are directly activated by wirelessly interrogating the fully passive device with a microwave carrier signal. This fundamental carrier signal, acquired by the implant antenna, mixes through the varactor diode along with the internal targeted neuropotential brain signals to produce higher frequency harmonics containing the targeted neuropotential signals. These harmonics are backscattered wirelessly to the external interrogator that retrieves and recovers the

original neuropotential brain signal. The passive approach removes the need for internal power sources and may alleviate heat trauma and reliability issues that limit practical implementation of existing implantable neurorecorders.

DEDICATION

To my family

ACKNOWLEDGMENTS

I am indebted to a number of people for their supportive influence and contribution to my doctoral studies.

I am especially grateful to my family, my mother, Sun ok Chon, and my brother, Gerald (Jerry) Chon Schwerdt, without whom I would not have been capable of pursuing research or a doctorate. I thank my mother who has always given me strength, support, and encouragement throughout my life and academic studies. I thank my brother for his friendship, generosity, wisdom, and for being someone I could rely on for sensible advice, entertainment, and a source of sanity and peace.

I have been very fortunate in having the opportunity to conduct research under the supervision of Dr. Junseok Chae. The invaluable knowledge and experiences that I obtained through his guidance over the past five years would not have been attainable elsewhere and strongly influenced my research abilities. I am thankful for his patience, enthusiasm, and always sincere and thorough advice and counsel. Working with Dr. Chae has greatly strengthened my capabilities and desire to pursue research.

I am grateful to Dr. Félix Miranda, my NASA Graduate Student Researcher Program (GSRP) mentor, for his positive influence and informed guidance throughout my doctoral studies. Dr. Miranda was a truly inspiring mentor and role model in his strong sense of responsibility and sincerity as well as his passion and knowledge for science. I am fortunate to have been able to work with Dr. Miranda and gain valuable insight from him regarding research, careers, and life.

I am thankful to my former and current lab mates, Seokheun Choi, Wencheng Xu, Xu Zhang, Ran Wang, Jennie Appel, Sangpyeong Kim, and Hao Ren, for their

friendship, amusement, and support. I am also grateful towards Dr. Craig Birtcher and Sameer Shekhar for their help with wireless testing, Patrick Larson and Daniel Gulick for their assistance with animal testing, Jaeyoong Cho at University of Michigan for his help with deposition processes, and CSSER (Center for Solid State Electronics Research) staff for their help with microsystem fabrication. I am thankful to Dr. Frederick Van Keuls and Ms. Elizabeth McQuaid of NASA Glenn Research Center (GRC) for their generous support and technical help in my research work and their friendship throughout my stays at GRC. I am grateful to Dr. Mark D. Kankam, Director of NASA GRC's University Affairs Office, for his support and interest in my research, and to Dr. Rainee N. Simons also of GRC, for his informative suggestions related to validating the clinical implications of the fully passive implant.

I am grateful towards my committee members, Dr. Constantine Balanis, Dr. Bruce Towe, Dr. David Frakes, and Dr. Stephen Phillips, for contributing their valuable time and energy towards my research studies. I thank Dr. Towe for his valuable help in benchtop wireless testing of the microsystem, including construction of the demodulator and animal testing along with his insight and feedback onto methods of improving the fully passive system and its clinical relevance. I am also thankful to Dr. Abbas Abbaspour-Tamijani, my former committee member, and a central figure in conceiving the designs and models of the fully passive neurorecording microsystem. Dr. Abbaspour-Tamijani patiently and kindly provided me considerable help and feedback during my initial studies on the system, for which I am grateful.

TABLE OF CONTENTS

Page

LIST OF TABLES

LIST OF FIGURES

Figure Page

Figure Page

Figure Page

CHAPTER 1

INTRODUCTION

1.1. Background and significance

The ability to monitor brain signals at or near single neuronal level implicates crucial challenges and aspirations subsisting the past several decades. Direct access to individual neuronal processes is requisite to uncover underlying brain operations, and consequently resolve fundamental neuro-scientific understanding to initiate remedial solutions for the numerous existing neurological disorders. Likewise, the brain's centric role in human behavior and function compel scientific revelation of its basic physiology and operation, of which are still largely unresolved. Brain based disorders may exist in a spectrum of forms and affect a significant proportion of the global population: Parkinson's disease (~ 1 million nationwide and > 4 million worldwide) (Kelley, 2011), epilepsy (~ 4 million nationwide and 50 million worldwide) (Salam, Sawan, & Nguyen, 2010), Alzheimer's (~5.4 million nationwide) (Association, 2013), paralysis (~ 6 million nationwide), and many other disorders. The causes, development, and cures for such disorders are still largely unknown, nonexistent, or generally ineffective. The clinical challenges are nearly equally matched by the lack of reliable recording technology to foremost approach and uplift these challenges. Whereas invasive stimulator devices such as deep brain stimulation (DBS) implants have been implemented in a large population– as their effectiveness in immediately suppressing severely debilitating neurologically based maladies greatly surpasses the induced trauma–the opposite is true for neurorecording; the recording functionality in itself does not directly manifest any physical benefits or remedy. Therefore, translation of implantable recording technology

to the clinical and neuroscience domains, first and foremost, demands safety and reliability, which is not entirely portrayed by current recording instrumentation. These safety barriers have gravely limited the medical applications of neurorecording systems.

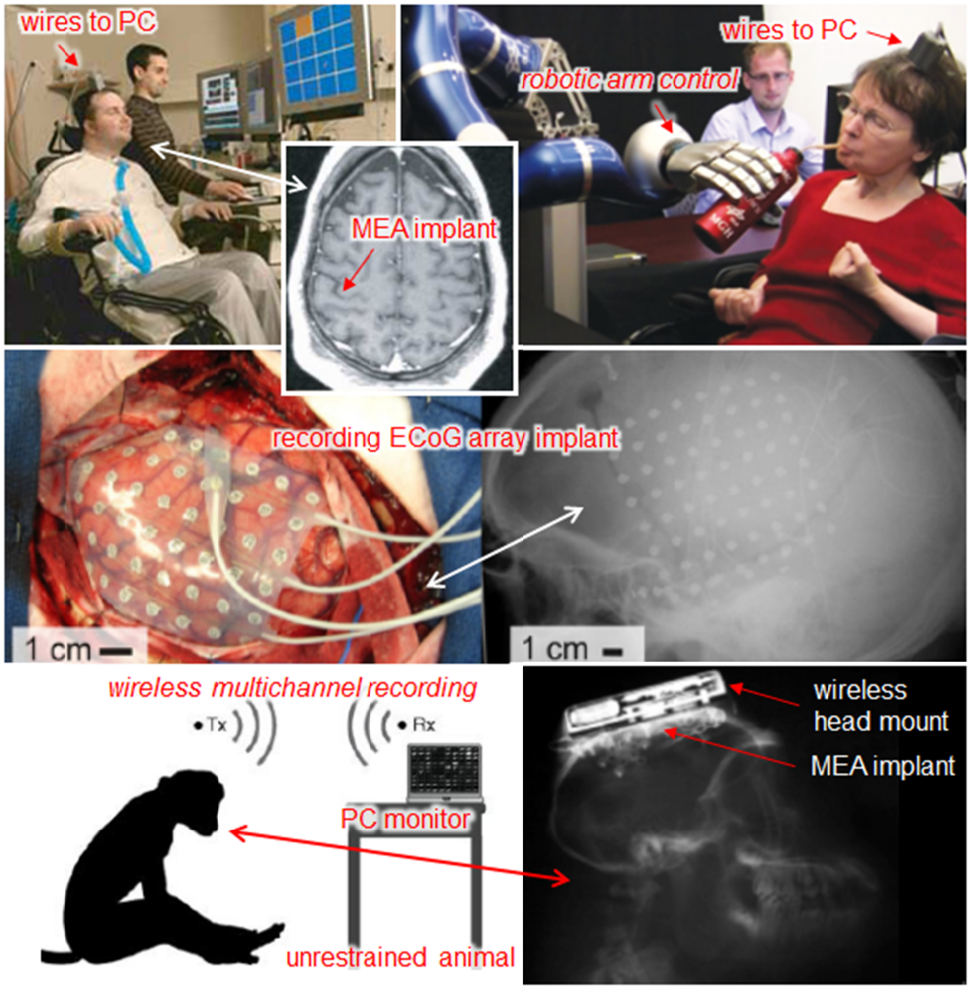

Figure 1.1. (Top row) Tethered neurorecording for brain computer interface (BCI) applications: benefits of restoring paralyzed limbs to computer control (Hochberg, et al., 2006) (top left) or prosthetic robotic arms (Hochberg, et al., 2012) (top right), but with serious limitations in subject mobility and risks associated with tethered wires connected from the brain to an external interface. Inset depicts implant location at right precentral

gyrus as indicated by arrow. (Middle row) Electrocorticography (ECoG) based wired neurorecording for epilepsy detection as implanted on exposed brain surface or cortex (Roland, et al., 2011) (Bottom row) First generation wireless implantable neurorecording BCI. Wireless neurorecording provides subject mobility and has been recently tested as safe and operationally stable as implanted in non-human primates for over a year (Borton, Yin, Aceros, & Nurmikko, 2013). However, limitations reside in implant heating and physical massiveness.

The work reported herein proposes a unique solution to potentially overcome some of these safety barriers as well as enable reliable and untethered recording of brain-derived signals. Naturally, the proposed system uses wireless telemetry to transmit internal brain signals to the outside world since the wired connection imposes numerous risks of infection and/or trauma that relegate the targeted safety requirements. Moreover, the proposed system shifts away from traditional elaborate circuit systems incorporating a profound scale of systematic analog and digital functions to record these brain signals and transmit them wirelessly to an external receiver. Instead, more recondite (in terms of brain recording applications) radar backscattering mechanisms are employed to wholly reconfigure the wireless neurorecording operation. These passive backscattering operations allow tremendous simplification of implant circuitry and eliminate the need for embedded powering schemes—both of which will directly enhance reliability and safety. Figure 1.2 outlines the present research stage of neurorecording along with their materialized forms in the medical and neuroscience fields, and highlights current non-

existent applications of neural recording that the proposed research distinctively manifests.

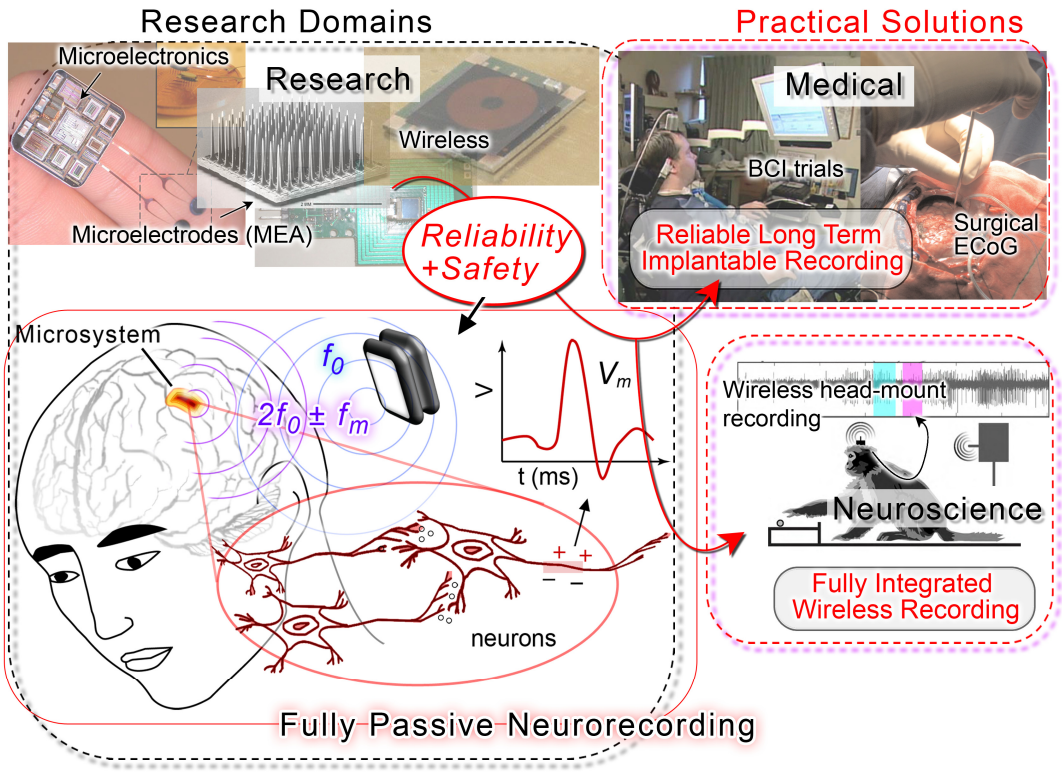

Figure 1.2. Broad overview of the proposed fully passive wireless neurorecording microsystem: Translating currently research restricted technology to reliable long-term implantable recording systems that may introduce novel cortical recording solutions that are not currently available in the medical and neuroscience fields. The fully passive implant targets reliability & safety: key parameters to enable these advancements. The recording device is implanted subdurally where cortical neuropotentials can be wirelessly backscattered to the external interrogator. Pictures of existing systems taken from (Nurmikko, et al., 2010) (Hochberg, et al., 2006) (Roland, Brunner, Johnston, Schalk, & Leuthardt, 2010) (Sodagar, Perlin, Yao, Wise, & Najafi, 2007, June).

1.2. Goals and Requirements

Establishing methods to safely monitor and record neuropotentials is crucial to lift barriers in studying underlying operations and mechanisms of the human brain and to develop treatments for its vast range of disorders. Current research emphasizes the wireless telemetry aspect of implantable sensors in order to make these devices ubiquitous and safe (Hatsopoulos & Donoghue, 2009) (Wisneski, Anderson, Schalk, Smyth, Moran, & Leuthardt, 2008) (Leuthardt, Schalk, Wolpaw, Ojemann, & Moran, 2004) (Hochberg, et al., 2012) (Wise, Sodagar, Yao, Gulari, Perlin, & Najafi, 2008) (Harrison, Design of integrated circuits to observe brain activity, 2008) (Sodagar, Wise, & Najafi, A fully integrated mixed-signal neural processor for implantable multichannel cortical recording, 2007). Furthermore, long term or chronic implants necessitate superior reliability and durability of its integrated electronics. Safety and reliability becomes of critical importance especially when associated with implantation into the brain. A biocompatible encapsulation is required to avoid evoking immune response from the body due to the material properties of the implant (Marin & Fernandez, 2010) (Ward, Rajdev, Ellison, & Irazoqui, 2009). Implant devices also require miniaturization and/or translation to more compliant materials to minimize their physical obtrusion and contortion of the brain (Kipke, et al., 2008) (Blount, Cormier, Kim, Kankirawatana, Riley, & Knowlton, 2008) (Wise, Sodagar, Yao, Gulari, Perlin, & Najafi, 2008). In addition to mechanically instilled perturbation, a major safety concern associated with operation of the implanted device relates to heat dissipated by embedded electronics as well as permeating wireless electromagnetic (EM) fields into the surrounding tissue (Vidal & Lopez, 2010). Minimizing heat generation caused by the cortically implanted

device is imperative, as temperature rises greater than 1 °C may irreversibly damage the brain (LaManna, McCracken, Patil, & Prohaska, 1989). Therefore, it is crucial to limit the impact of heat emanated by integrated circuit as well as impinging EM waves in the human body. The power consumption of implanted electronics must be limited to within several *milliwatts* to *microwatts* to minimize heat trauma in the human body. To evaluate heat dissipated by permeating and absorbed EM radiated waves, the specific absorption ratio (SAR) value is commonly applied to quantify the safety of mobile communication devices and is regulated by the U.S. Federal Communications Commission (FCC) (SAR $\leq$ 1.6 W/kg averaged over 1 g of tissue) (Means & Chan, 2001). An entirely passive and wireless microsystem for recording neuropotentials may help address these severe requirements for safety and reliability. The passive approach removes the need for internal power sources and may alleviate heat trauma and reliability issues that limit practical implementation of many existing implantable neurorecorders. The goals and requirements of the fully passive neurorecording device are tabulated in Table 1.1. Besides the safety enhancements that will be made possible through a fully passive scheme, a few major functional limitations are foreseen as depicted in Figure 1.3. Attempts to recover these functions will be considered in later sections of this thesis.

Table 1.1. Goals and requirements of the fully passive neurorecording system.

Aspect	**Requirement**
Heat dissipation	$\Delta T < 2$ °C (~10 mW for 70 mm^3 IC)
Specific absorption ratio (SAR)	< 1.6 W/kg over 1 g head volume (FCC regulation)

Detect neuropotentials (ie. spikes & local field potentials)	30 µV sensitivity/threshold (min. noise input)
Integrity of neuropotentials (accuracy)	±10 µV to ±1 mV dynamic range 300 Hz – 5 kHz (spikes) 10 Hz – 250 Hz (LFPs)
Wireless read range	> 1 cm range (sustain free movements of subject)
Risk of physical trauma	Biocompatible encapsulation & minimal footprint

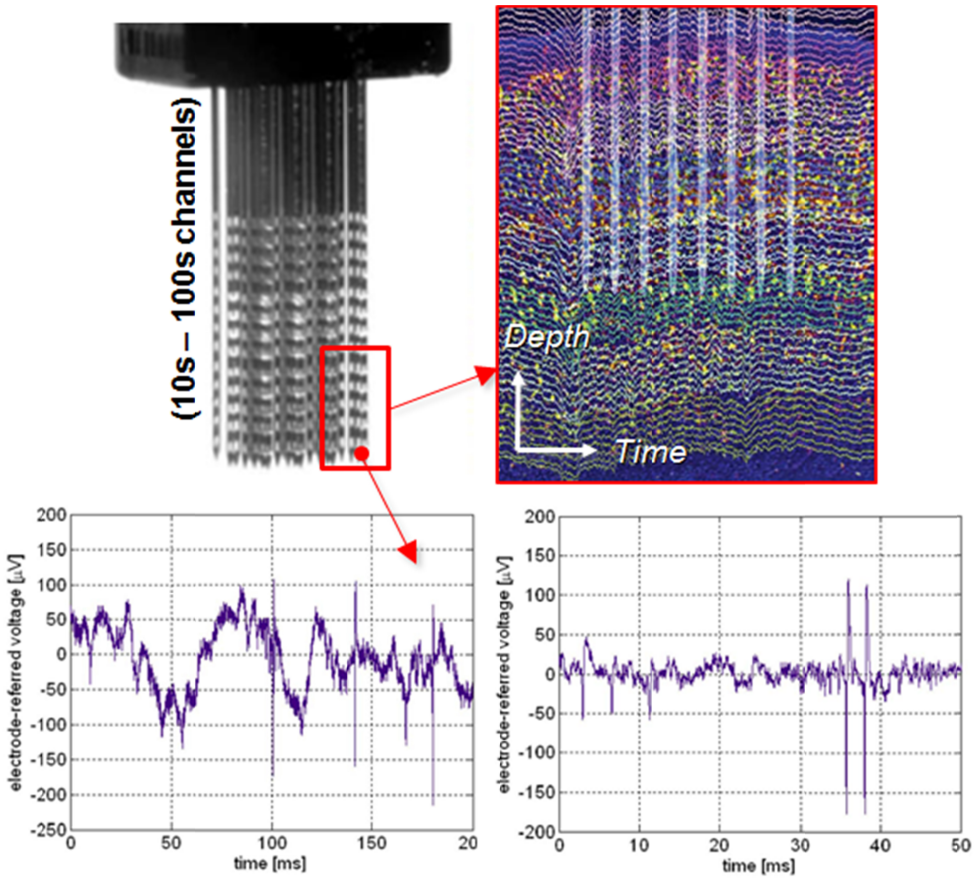

Figure 1.3. Functional challenges foreseen in fully passive approach: (Top) Multichannel capabilities may be difficult to realize without active switching or multiplexing circuit operations and provide important information onto the spatio-temporal physiology of the

brain operations (Blount, Cormier, Kim, Kankirawatana, Riley, & Knowlton, 2008). (Bottom) In addition to the low level magnitudes of targeted neuropotential signals (*microvolts*), noise will undoubtedly accompany targeted neuropotentials and cannot be suppressed on the fully passive circuit void of active filtering, amplification, and/or algorithmic processing usually integrated onto active recorders (Harrison, Design of integrated circuits to observe brain activity, 2008).

1.3. Wireless recording of neuropotentials

Neurorecording denotes measuring of the varying electrical potentials (ie. neuropotentials) originating from neurons that make up the fundamental building blocks of the brain and nervous system (Figure 1.4). Intracellular potentials of "excited" neurons have amplitudes in the range of ~ 100 mV_{pp} with a frequency near kHz regime as depicted in Figure 1.3. On the other hand, due to limitations in surgical installation and placement of implant electrodes, practical recording sites are often extracellular, wherein electrical potentials range few orders of magnitude lower, spanning ~ 5 – 1000 μV_{pp}. The manner in which these signals may be recorded varies depending on the application and requirements. A majority of the commercially available and clinically implemented recording tools are non-invasive (Figure 1.5); popular non-invasive tools include electroencephalography (EEG) whereby the recording electrodes are placed relatively far (atop the scalp) from the actual originating sites of the neuropotentials to measure a largely integrated function of electrical activity from the brain, and functional magnetic resonance imaging (fMRI) to image large-scale regional activation of a network of neurons via strong magnetic fields that detect areas of blood flow in the brain coinciding

with electrically active neurons. However, these non-invasive tools are severely limited in spatial resolution or their inability to capture single-unit or near single-unit level action potentials. This spatial selectivity is obligated for building useful prosthetics, mapping and understanding specific workings of neural populations, and correlating behavior, thoughts, and actions to specific neural connections. Higher spatial resolution is therefore only achieved with a more invasive approach. Semi-invasive recording may be contrived via electrocorticography (ECoG) whereby neuropotentials are recorded from the cortex (brain's outermost and most active layer) (Nicolelis, 2008). Intracortical recording has revealed important discoveries of fundamental brain processes as implemented in animal models (Nurmikko, et al., 2010), manifested into early stage clinical remedies for paraplegic patients (Hochberg, et al., 2006), and been used in surgical procedures for treatment of epilepsy (Blount, Cormier, Kim, Kankirawatana, Riley, & Knowlton, 2008). Recording from deeper brain tissue matter is also possible using more invasive techniques, such as microelectrode array (MEA) technology (Wise, Sodagar, Yao, Gulari, Perlin, & Najafi, 2008).

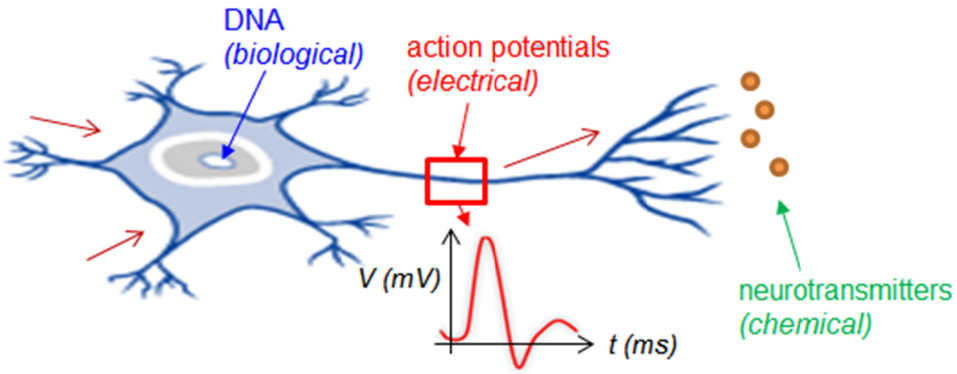

Figure 1.4. Illustration of neuron and operational signaling modalities of biological (~ days – years response time), chemical via neurotransmitters in the synapse (~ minutes – days response time), and electrical via action potentials (~ msec – sec response time).

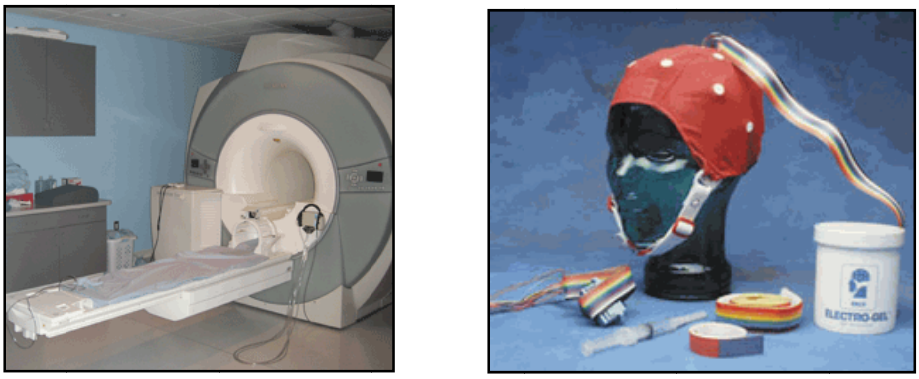

Figure 1.5. (Left) Equipment used for fMRI (Applied fMRI Institute, 2010). The patient lies on the sliding tray to be inserted into the cylindrical chamber where imaging takes place. (Right) EEG-cap worn on a head model. The individual EEG electrodes are situated underneath the cap and each of these is connected to the ribbon cables, which would then be interfaced with another machine or computer (Biopac Systems, 2010).

Standard wireless implantable neurorecording microsystems typically comprise microelectrodes to access clusters of neighboring neurons, large scale circuitry to amplify

low level neuropotentials and to process and prepare these signals for wireless telemetry, and a wireless link (antenna or inductive coil) to transmit the neuropotential signals (Wise, Sodagar, Yao, Gulari, Perlin, & Najafi, 2008) (Figure 1.6). The integrity of the recording and wireless telemetry necessitates sophisticated mixed-signal circuitry (Harrison, et al., 2009) (Sodagar, Wise, & Najafi, A fully integrated mixed-signal neural processor for implantable multichannel cortical recording, 2007). The level of circuit complexity is multiplied for multichannel operation, and practical applications often require tens to hundreds of channels. Likewise, the number of channels is directly related to power consumption levels, which is proportional to the generated heat. Temperature rise must be limited to 1 – 2 °C in the cortex to avoid potential detriment (LaManna, McCracken, Patil, & Prohaska, 1989). For a typical CMOS circuit with a volume of 70 mm^3 placed on the cerebral cortex, these temperature thresholds effectively limit maximum allowable heat dissipation from the circuit to 10 mW (Harrison, Design of integrated circuits to observe brain activity, 2008). In order to prevent heat emanation into the brain tissue, the microelectronics are usually embedded subcutaneously and outside of the brain. This extracranial chip is then physically wired into the skull to connect with the electrodes penetrating the cortex (Song, et al., 2009) (Harrison, et al., 2007). However, physical trauma may be attributed to the tethering forces and associated movement caused by the surgical wiring through the skull (Wise, Sodagar, Yao, Gulari, Perlin, & Najafi, 2008) (Kim, et al., 2009). To remove this surgically-burdening and possibly traumatizing wiring, circuits may be monolithically integrated onto the electrodes, or physically incorporated with the electrodes by other means (Ho, Chen, Tseng, Yeh, & Lu, 2007) (Perlin & Wise, 2009, January). Nevertheless, the need for a

highly complex and dense array of circuit elements and functions on the recording circuit may diminish the potential longevity and robust properties of the implant system (Constantinescu, 2003).

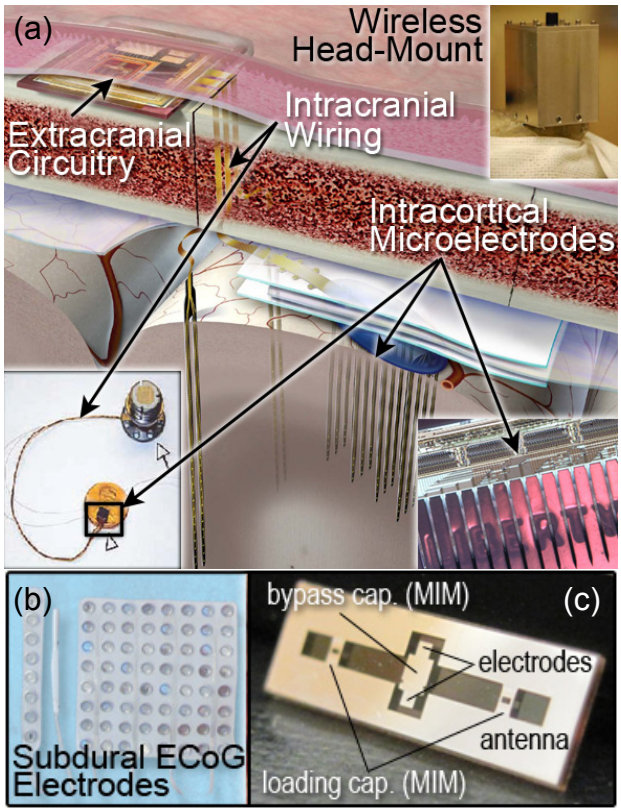

Figure 1.6. Overview of standard and fully passive neurorecording technology. (a) Existing neurorecording microsystem technology: (left) microelectrode arrays (MEA) comprising of multiple rows of penetrating recording sites on individual electrodes, and (right) placement and wiring between wireless recording components in a surgical implant (Nurmikko, et al., 2010) (Wise, Sodagar, Yao, Gulari, Perlin, & Najafi, 2008). (b) Wired subdural ECoG arrays used by clinicians, usually for epilepsy detection (Blount, Cormier, Kim, Kankirawatana, Riley, & Knowlton, 2008). These are implanted

on the surface of the brain and wired to an external monitor for large scale neurorecording. (c) Fully passive neurorecording microsystem of this thesis.

1.4. Wireless telemetry schemes

The manner in which wireless transmission is realized in implant devices may be realized through active, passive, and/or fully-passive schemes. Active devices have an internal energy source, such as a small rechargeable battery, energy harvester, etc., supplying all power needed to operate enclosed circuitry (Song, et al., 2009) (Chestek, et al., 2009) (Rizk, et al., 2009). For application as an in-body implant, a few challenges are made immediately apparent; the integrated power supply increases overall implant dimensions, batteries need to be recharged or replaced, and power harvesting sources require additional power regulation circuitry that again enlarges the implant footprint.

More recently, passive methods have been adopted in an attempt to lessen heat dissipation, shrink footprint, and prolong implant operation lifetime (Harrison, et al., 2009) (Sodagar, Perlin, Yao, Wise, & Najafi, 2007, June) (Holleman, Yeager, Prasad, Smith, & Otis, 2008, November). Passive systems extract power exclusively from external sources and activate instantaneously upon coupling of incident electromagnetic (EM) radiated waves or magnetic flux. Coupled time-varying power is rectified and regulated to activate onboard circuitry only while the implant is interrogated by an external interrogator supplying the EM propagated waves or inductively coupled magnetic flux. In result, internal batteries, harvesters, or other forms of power supplies are not needed. Passive systems are increasingly employed in RFID (Radio Frequency IDentification) technology, where low-cost and long-term qualities are targeted. Active and passive schemes are adopted for the large part of existing wireless neurorecording

microsystems and their capabilities successfully demonstrated as implanted in a number of live animal and even human subjects (Chen, Wu, Hyland, Lu, & Chen, 2008) (Rizk, et al., 2009) (Borton, Yin, Aceros, & Nurmikko, 2013).

Here, "fully" passive describes a more particular type of passive system precluding any type of formal energy source. A fully passive device does not need to regulate or rectify externally supplied power in order to activate onboard circuitry. Instead, targeted data from the fully passive device is wirelessly communicated to an external interrogator by means of the innate variable nature of the fully passive circuit. Wireless telemetry of targeted information (in this case, the neuropotentials) is achieved by the ability of the circuit to electrically transform itself as a function of the coupled targeted biological signal. These changes in the fully passive circuit are then wirelessly detected upon interrogation by an external interrogator. In other words, the fully passive device simply acts as a tag that converts the targeted biological signal to a wirelessly detectable nature. As a result, sophisticated circuitry is entirely excluded. As the fully passive circuit dissipates little of the induced power (theoretically zero for a purely reactive circuit), the fully passive system may reduce risks associated with power dissipation and heat emanation into tissue. For the application at hand, wireless telemetry of neuropotential signals transpire solely by means of the intrinsic nonlinear properties of embedded varactor elements whose impedance varies as a function of the inputted neuropotentials and externally provided wireless carrier signal. The varactors' nonlinear variation are conveyed upon the wireless carrier in the form of amplitude modulation that are backscattered and detected by an external interrogator that can demodulate and recover the original neuropotential data. This backscattering effect has been employed in

both the active and passive schemes, and is pervasive in RFID technology (Penttila, Keskilammi, Sydanheimo, & Kivikoski, 2006) (Nikitin & Rao, 2006). However, in the fully passive case, the backscattering effect becomes of predominant interest since the fully passive circuit, by itself, cannot generate any radio frequency (RF) signals. Furthermore, as will be seen, given the minimalistic nature of the fully passive implant, the technical burden lies heavily on the external receiver system to perform all signal conditioning and processing operations, conventionally assumed by the internal implant circuit for the active and some passive systems. A notable example of successful implementation of fully passive methods was demonstrated in the widely-commercialized arterial pressure sensors that have been implanted in over a hundred patients (Fonseca, Allen, Kroh, & White, 2006, June). Fully passive systems have also found application in monitoring *in vivo* bioelectrical signals as generated by the heart, electrocardiography (ECG), or the brain, ECoG or electroencephalography (EEG) (Towe, 2007, May) (Abbaspour-Tamijani, Farooqui, Towe, & Chae, 2008, August) (Riistama, Aittokallio, Verho, & Lekkala, 2009).

The first narrated idea of using voltage sensitive elements for wireless biological telemetry dates back to 1965 (Honig, 1965) and was reintroduced in 2007 when the idea was materialized through the use of off-shelf varactors combined to an inductor coil for wireless fully passive transmission of emulated biopotentials (Towe, 2007, May). More recently, the technique was used to wirelessly monitor ECG from epidermal electrodes on humans (Riistama, Aittokallio, Verho, & Lekkala, 2009). In the latter system, a resonance detection scheme was applied to monitor the shift in impedance of the varactor in response to ECG voltage. Both sensors relied on inductive coupling for wireless

telemetry. Inductive coupling is an attractive wireless telemetry technique because of its relatively high efficiency as compared to EM propagation. Inductive coupling is usually an obvious choice for operation at low frequencies, i.e., below 1 GHz, where the equivalent EM operating antenna may become too large for practical implantation. The efficiency of inductive coupling is mainly determined by the geometry of both coils, the magnetic properties (permeability) of the transmission media, and the relative placement of the coils. The amount of tissue pervading incident magnetic flux is not affected by the surrounding transmission media since the permeability of biological and free-space matter is nearly unity and the flux is not a function of the dielectric properties (permittivity) of the medium. However, the amount of flux carried to the implant is very sensitive to the relative placement of the primary and secondary coils (Wansch, 2001). At higher frequencies, inductive coils may be replaced by antennas where RF energy propagates as EM waves. Although the traversing EM waves experience greater attenuation through tissue at increasing frequency, the internal efficiency of the antenna also increases (Abbaspour-Tamijani, Farooqui, Towe, & Chae, 2008, August) (Poon, O'Driscoll, & Meng, 2010). Due to these opposing trends, migrating to a higher frequency can potentially improve the overall efficiency of the wireless link for a given area. Optimal frequency will ultimately depend on the specific design of the antenna as well as the thickness and electrical properties of the striated tissue layers between the interrogator and implant. Prototypes of fully passive recorders implementing EM propagation modes for wireless transmission were previously created on a printed circuit board (PCB), and produced encouraging results as operated for an interrogation frequency of 2.48 GHz (Abbaspour-Tamijani, Farooqui, Towe, & Chae, 2008, August).

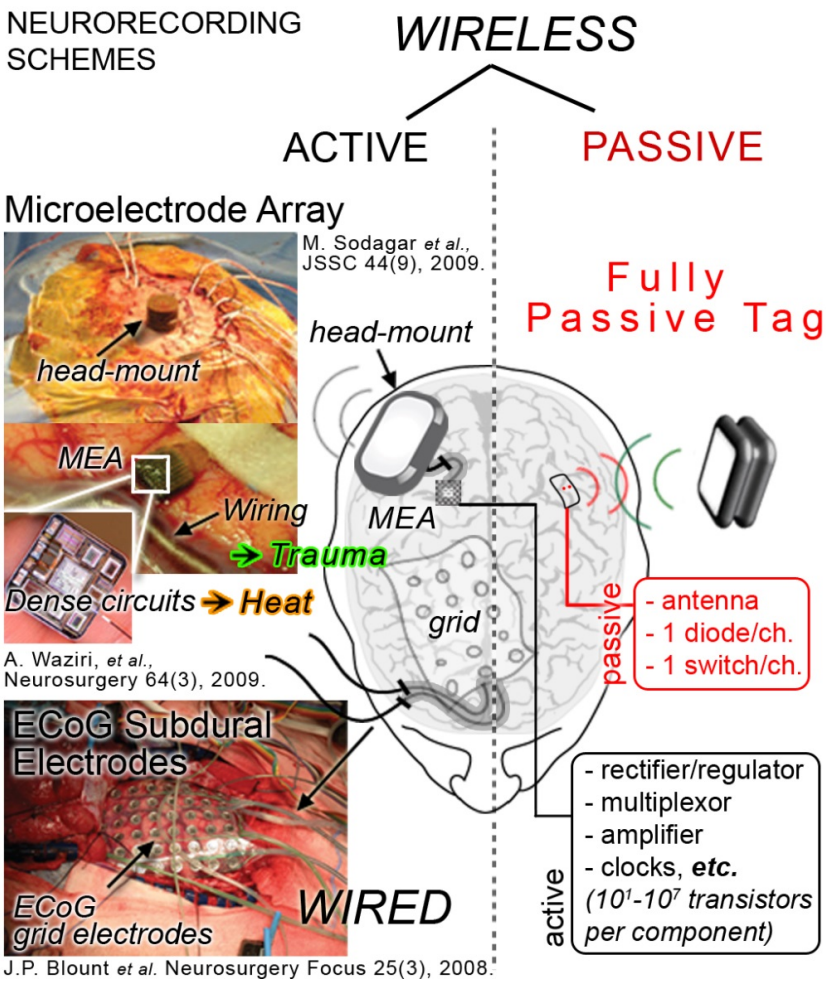

Figure 1.7. Overview and comparison of standard active wireless neurorecording and fully passive neurorecording schemes (Sodagar, Perlin, Yao, Najafi, & Wise, An Implantable 64-Channel Wireless Microsystem for Single-Unit Neural Recording, 2009) (Blount, Cormier, Kim, Kankirawatana, Riley, & Knowlton, 2008) (Waziri, Schevon, Cappell, Emerson, McKhann, & Goodman, 2009).

In consequence, the fully passive approach favors enhanced safety features for chronic monitoring of electrophysiological signals inside the brain while manifesting a

very simple and reliable structure (few diode and capacitor elements along with a wireless antenna link). This thesis first describes the theory and methodology for realizing a basic single channel fully passive implantable neurorecording device. Despite its fundamentally simple circuit structure, computational design is necessary to optimize wireless backscattering and harmonic generation of the nonlinear diode elements that collectively provide the fully passive recording functionality. The theoretical and computational models are discussed in chapter 2. Physical realization of the wireless neuropotential recording device is achieved using standard microfabrication processes (chapter 3). The fabricated device is tested under a variety of conditions to evaluate its performance in physiologically relevant environments (chapter 4). Finally, safety of the single channel device is analyzed to ensure that it can be implanted in its intended brain tissue environment without endangering the subject, and to substantiate its underlying fully passive benefits (chapter 5). After realizing and confirming the basic capabilities and safety features of the single channel device, methods to record from multiple channels while employing and maintaining the same fully passive operations are investigated (chapter 6). Optical modalities are supplemented onto the original RF backscattering operation to attain multi-site recording functionality, and a wireless prototype of this fully passive multichannel neurorecording system is produced and tested to validate its performance. In this multichannel scheme the recording operation is different in that the varactors are replaced with forward conducting diodes to tune the harmonic generation behavior of these nonlinear mixer elements in response to light. This substitution in mixing operation and design is performed primarily because it is easier to manipulate generated backscatter harmonics containing neuropotential using the resistive

mixing diodes (schottky diodes) rather than reactive mixing varactor diodes. In succession, the current challenges of the fully passive systems are discussed along with potential methods to mitigate and overcome these (chapter 7). Finally, the thesis is concluded in chapter 8.

CHAPTER 2

DESIGN OF A FULLY PASSIVE NEURORECORDER

The wireless neurorecording system consists of two components: 1) the neurorecording and backscattering microsystem, and 2) the external dual band interrogator (Figure 2.1). Wireless backscattering in the form of radiating EM waves strongly depends on the electrical properties of the media through which the waves propagate, especially at microwave frequencies. These properties alter the impedance of the internal antenna and govern a major portion of the path loss experienced by the wireless signal (Balanis, Advanced Engineering Electromagnetics, 1989). Furthermore, path loss increases with decreasing wavelength (increasing frequency) and increasing depth of tissue penetration. On the other hand, higher microwave frequencies are used to minimize the size of the antenna integrated onto and dominating overall microsystem footprint. As the antenna impedance is a function of the medium in which it is operating, the properties of the biological tissue must be taken into account in the design of the backscattering system. The complete wireless system was designed using a hybrid simulation of harmonic balance circuit mixing in ADS (Advanced Design System, Agilent) and antenna and wireless radiation in HFSS (High Frequency Structure Simulator, Ansoft).

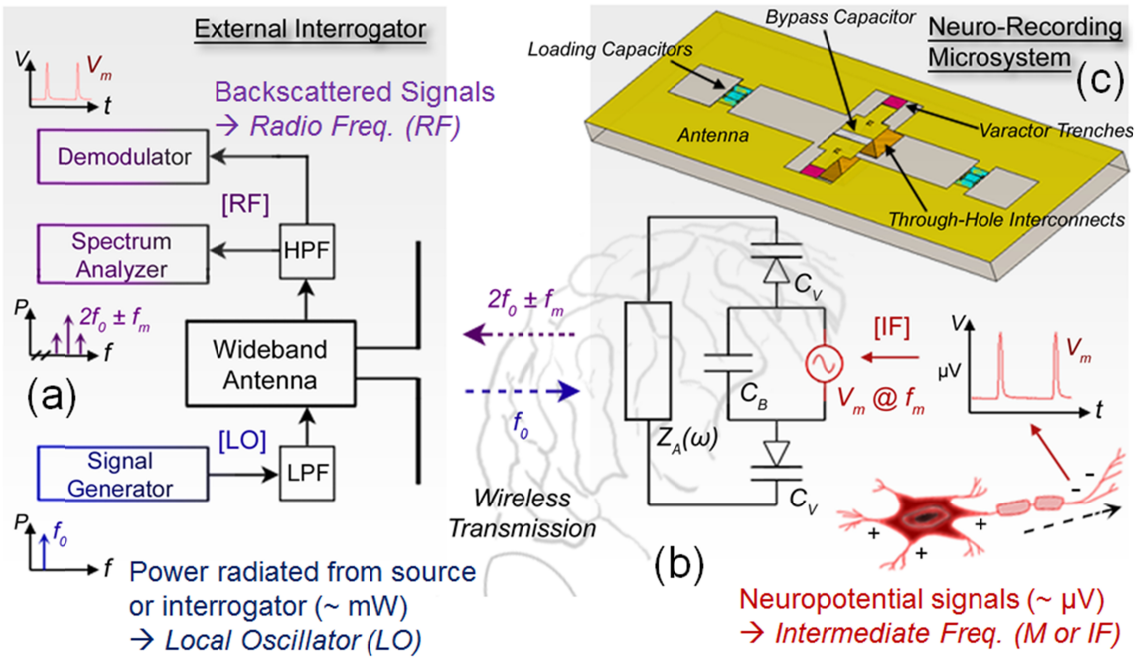

Figure 2.1. Overview of wireless fully passive neurorecording. (a) Block diagram of external interrogator. The signal generator (bottom left) supplies the exciter at f_0 that is fed into an LPF at the LO port of the external interrogator. This carrier is wirelessly transmitted to the microsystem, which backscatters third-order harmonics at $2f_0 \pm f_m$. These wireless third-order harmonics are retrieved by the external interrogator and fed into an HPF at the RF output. The RF signals ($2f_0 \pm f_m$) can be monitored on a spectrum analyzer, where the modulating $\pm f_m$ components are visualized in a spectral plot, and/or through downconversion and demodulation, where the RF signals are downconverted to baseband (f_m) and V_m temporal waveforms are reconstructed. (b) Basic schematic of neurorecording microsystem circuit with illustration of source of neuropotentials (neuron). Dashed black arrow indicates direction of propagating action potentials down the axon. Neuropotentials are conveyed as an ac source (IF) with an amplitude of V_m and frequency of f_m that are directly supplied to the neurorecording circuit. (c) Layout of the

neurorecording microsystem. The on-chip planar slot antenna is loaded by capacitors at both ends of the slot. The bypass capacitor and varactors on the topside connect directly to targeted neuropotentials via backside through-hole interconnects.

2.1. Fully passive neurorecording circuit

The neurorecording circuit comprises of two M/A-COM MA46H120 varactors (C_V), a bypass capacitor (C_B), and an integrated antenna that can be represented by an impedance component (Z_A), as depicted in Fig. 1b. The varactor pair acts as a nonlinear mixer that is responsible for generating harmonic mixing products of the neuropotentials and externally supplied carrier. This mixer inputs the neuropotential signals and incident microwaves at the intermediate frequency (IF) port and local oscillator (LO) port, respectively. The mixer combines these two signals (f_m at IF and f_0 at LO) and upconverts them to $2f_0 \pm f_m$, at the radio-frequency (RF) port. The third order intermodulation (IM3) products, $2f_0 \pm f_m$, are wirelessly backscattered to the external interrogator in the form of amplitude modulated (AM) transmission where they are downconverted and demodulated (Fig. 1a). Although, a more straightforward mixing scheme may be applied to generate second order harmonics, $f_0 \pm f_m$, neuropotentials have very low frequencies (1 Hz to several kHz) and amplitudes (10s of microvolts) in comparison to the supplied LO. EM waves physically reflect from surrounding surfaces (Galejs, 1969) and these structural reflections manifest into electrical noise causing interference and desensitization especially near the LO band (f_0). The on-chip antenna acts as both the LO and RF interfaces for the mixer, while the through hole recording electrodes that interface tissue and retrieve neuropotentials acts as the IF port. C_B decouples the RF and LO signals from

the IF port, effectively short circuiting the electrode interface at high frequencies. The antenna itself has a near zero impedance at DC, which effectively short circuits the radiation ports at low frequencies. The antenna is implemented as a capacitively-loaded slot antenna to allow proper optimization of its impedance at LO and RF frequencies.

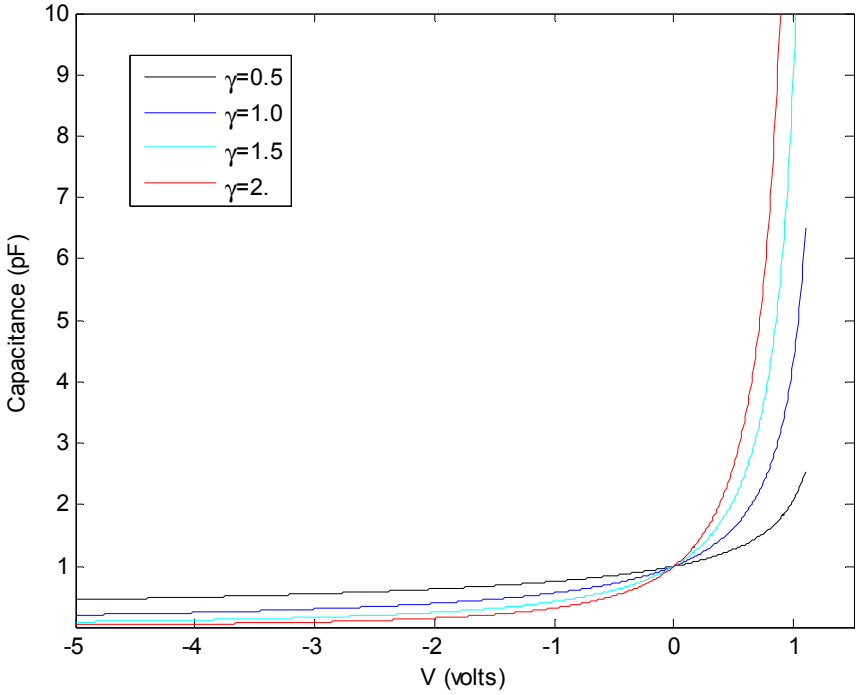

Figure 2.2. Ideal nonlinear variation of capacitance as a function of applied voltage for ideal varactors using Equation (2.1) for different γ, depicting steeper C variation with increasing γ.

A varactor is essentially a voltage-variable capacitor and its capacitance as a function of applied voltage is expressed as,

$$C_v(V_r) = \frac{C_j}{\left(1 + V_r / V_j\right)^{\gamma}} + C_p \tag{2.1}$$

where V_r is the reverse-bias applied voltage, V_j is the junction voltage intrinsic to the device, γ is the gamma coefficient associated with doping parameters, C_p is the parasitic capacitance of the package, and C_j is the junction zero-bias capacitance (Maas, 2003). The gamma coefficient, γ, controls the nonlinear characteristics. As a result, this variable nonlinear capacitor produces nonlinear mixing products, including the 3rd order terms at $2f_0 \pm f_m$, whose amplitude is proportional to $V_0^2 V_m$ and constitute the desired backscattering signals. The input of the mixer system may be described as a superposition of the incident microwaves and input neuropotentials; $V = V_0 \cos(\omega_0 t) + V_m \cos(\omega_m t)$. Equation (2.1) may be expanded into a Taylor Series and substituted into the current-voltage relation, $I = dC(V)V/dt$, to approximate the harmonic current output of the varactor approximating an operating point near zero volts;

$$I = \left(C(V=0) + \frac{\frac{dC}{dt}(V=0)}{1!} V + \frac{\frac{d^2C}{dt^2}(V=0)}{2!} V^2 + \frac{\frac{d^3C}{dt^3}(V=0)}{3!} V^3 + \ldots \right) \frac{dV}{dt}$$

$$I = \frac{d}{dt}\left(\sum_{n=1}^{\infty} c_n V^n \right) V$$

$$I = \frac{d}{dt}\left(c_1 + c_2 V + c_3 V^2 + \ldots \right) V$$

$$I = (c_{1a} + c_{3a})\sin(\omega_0 t) + (c_{1a} + c_{3a})\sin(\omega_m t)$$

$$+ c_{2a}\sin(2\omega_0 t) + c_{2b}\sin(2\omega_m t) + c_{2c}\sin(\omega_0 t \pm \omega_m t)$$

$$+ c_{3b}\sin(2\omega_0 t \pm \omega_m t) + c_{3b}\sin(\omega_0 t \pm 2\omega_m t) + \ldots \tag{2.2}$$

where the coefficients, c_n, determine the magnitude of the respective nth-order harmonics, and the subscripts, a and b, denote the combination of the capacitance coefficient with the given amplitude, V_0 and V_m, of the inputted harmonics. As mentioned earlier, this IM3 mixing scheme is used instead of more straightforward second order mixing to avoid the large interference around the carrier frequency f_0 as the modulating signals of f_m occupy a very low frequency band of less than few kHz. A high c_3 is desirable to augment the magnitude of the third-order backscattering signals, $c_{3b}\sin(2\omega_0 t \pm \omega_m t)$, and is determined by γ, V_m, and V_0. By expanding the Taylor Series terms, the magnitude of these harmonics are approximately,

$$c_{2c} = \frac{C_j \gamma}{V_j} \cdot \left(\frac{V_0 V_m (\omega_0 + \omega_m)}{2} \right)$$

$$c_{3b} = \frac{C_j (\gamma^2 + \gamma)}{4 V_j^{\,2}} \cdot \left(\frac{V_0^{\,2} V_m \omega_m}{4} + \frac{V_0 V_m (V_0 \omega_0 + V_m \omega_m)}{2} \right) \tag{2.3}$$

for the IM2 and targeted IM3 harmonics, respectively. The conversion gain of the system, defined as the ratio of the power in IM3 backscattering terms to that of information signal (V_m), is a function of the LO power, varactor's γ, and impedance values seen by the diode at different frequencies. This conversion gain is generally used to describe the efficiency of a mixer system. The choice of the varactor, design of the antenna, bypass capacitor and loading capacitors, electrode-tissue interface, and the biological media all impact that value of the conversion gain.

Although the varactor nonlinearity generally can produce all of the possible harmonics and mixing products of ω_0 and ω_m, it can be shown that the use of two

varactors in back-to-back configuration helps reduce even-order harmonics and mixing terms, particularly the $2\omega_0$ term that interferes with the targeted third-order mixing products. This interference is mostly due to the phase noise associated with the second-order harmonic causing the magnitude of this signal to "jitter" around this frequency band and, in this case, into the nearby targeted modulating $\pm f_m$ components of the $2f_0$ signal. Ideally, the use of matched back-to-back varactors leads to a an even expression for *C(V)*, guaranteeing that the varactor current, $I = dC(V)V/dt$, is an odd function of the voltage. In such circumstances the diode current will only contain odd-order harmonics and mixing products, and will exclude terms such as $2\omega_0$. In practice, any mismatch between the diodes or asymmetry in their placement in the circuit can impair this condition, giving rise to a finite output at $2\omega_0$ and other even mixing terms. This behavior is conveyed by replacing V in Equation (2.2) with a differential input of V_+ and V_-, where $V_+ = V_0\cos(\omega_0 t) + V_m\cos(\omega_m t)$ and $V_- = -[V_0\cos(\omega_0 t) + V_m\cos(\omega_m t)]$. The output in this differential scheme is modified to,

$$I = \frac{d}{dt}\left(\sum_{n=1}^{\infty} c_n V_+^{n+1} - c_n V_-^{n+1}\right)$$

$$I = \frac{d}{dt}\left(c_1 V_+ - c_1 V_- + c_2 V_+^2 - c_2 V_-^2 + c_3 V_+^3 - c_3 V_-^3 + \ldots\right)$$

$$I = (c_{1a} + c_{3a})\sin(\omega_0 t) + (c_{1a} + c_{3a})\sin(\omega_m t)$$
$$+ c_{3b}\sin(2\omega_0 t \pm \omega_m t) + c_{3b}\sin(\omega_0 t \pm 2\omega_m t) + \ldots \qquad (2.4)$$

The coefficients, c_{1a}, c_{3a}, and c_{3b} will have a different value than those associated with Equation 2.2. As seen in the expanded form of Equation 2.4, the even-order harmonics, associated with 2ω, 4ω, *etc.,* cancel out. It should be noted that Equations 2.2 to 2.4 are

simplified and approximate expressions, since the real harmonic output cannot be expressed in closed-form. The varactor's ability to produce third-order harmonics will influence the design of the integrated antenna and its overall backscattering response, which will be described in the next section.

2.2. Integrated antenna and wireless backscattering

A sub-resonant slot antenna is integrated onto the neurorecording microsystem to operate at an incident frequency (f_0) around 2.25 to 2.45 GHz and a backscatter frequency ($2f_0$) around 4.5 to 4.9 GHz. The antenna's slot is 10 mm in length and 1 mm in width and is loaded with a pair of MIM capacitors, used to optimize the impedance of the antenna for the best conversion gain. These MIM capacitors effectively lengthen the dimensions of the slot at the LO frequency and shorten it at the RF frequency. In free-space media the wavelength of the incident microwave signals at 2.45 GHz is approximately 12.2 cm. For a resonant antenna, the slot size should equal half the wavelength ($\lambda/2$), 6.1 cm (Balanis, Antenna Theory: Analysis and Design, 2005). The half-wavelength slot antenna impedance can be estimated using Babinet's principle to define the EM field distribution of its complementary structure, the dipole, which has an impedance of Z_{dipole} = 73 + j42 Ohm, in free-space. The basic $\lambda/2$ slot antenna impedance is then given as $Z_{slot} = \eta^2/4Z_{dipole}$, where η is the intrinsic impedance of the propagation medium or ~ 377 Ohm for free-space, resulting in Z_{slot} = 363 – j211 Ohm. Although this capacitive impedance presents a mismatch for the varactor mixer circuit which is also capacitive, other planar single layer conductor antennas such as dipole and loop antennas

exhibit a much smaller real part of impedance meaning that they are not efficient radiators, despite their ability to match with the reactive part of the varactor (ie. they display an inductive impedance at *λ/2*). Further, the real parts of antenna impedances are reduced inside the lossy tissue environment, which would diminish radiation efficiency. One reason the slot antenna was selected for this application is that its aperture geometry is useful for embedding circuits within the antenna without increasing overall footprint and was conducive to a planar microfabrication process. To increase operating bandwidth or dual band operation, impedance tuning may be provided by introducing tuning capacitors inside the slot. In addition, it is possible to reconfigure the slot geometry and dimensions to generate an inductive impedance and reduce mismatch losses to the capacitive mixer circuit in a lossy tissue environment (Marrocco, 2007). When EM waves pervade through biological transmission media, the permittivity (ε) increases, and as a result, wavelength decreases by a factor of $\varepsilon^{-0.5}$. For the slot radiating inside the biological tissue, including layers of cerebrospinal fluid (CSF), bone, fat, and skin, the effective wavelength is a fraction of this value , but still large enough to make the 1 cm-long slot sub-resonant. The effective wavelength may be estimated using the ε of the dura mater that is ~ 45 at 2.45 GHz and ~ 42 at 4.9 GHz (Table 2.1) for a $\lambda = c/\left(f\sqrt{\varepsilon}\right)$, which is $\lambda_{2.45GHz}$ ~ 17 mm and $\lambda_{4.9GHz}$ ~ 9 mm.

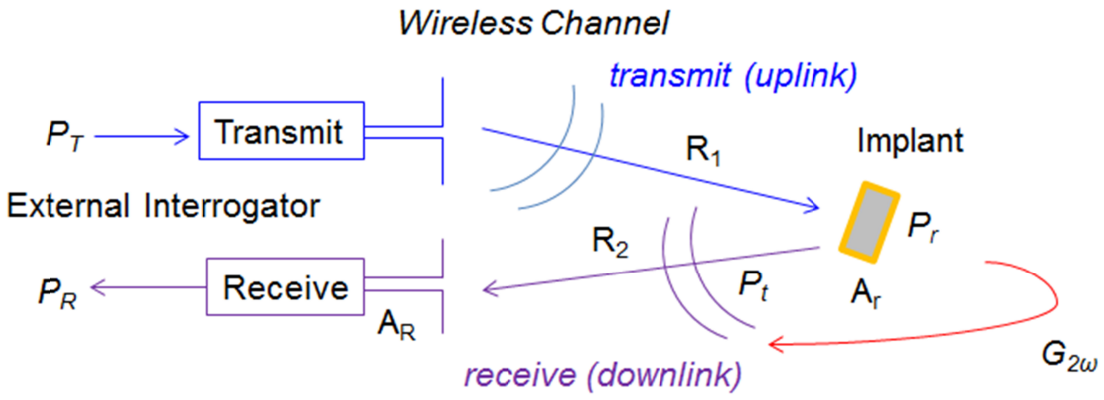

Figure 2.3. Diagram of wireless backscattering parameters.

For an electrically small antenna (ESA), where the maximum dimension is less than $\lambda/2\pi$ (about 1.94 cm for 2.45 GHz in free space), bandwidth and gain are severely compromised (Wheeler, 1947) (Harrington, 1960). The directivity of a short slot antenna with infinite ground is 1.76 dBi. The overall gain is usually 1-3 dB lower than this value, due to losses in the metal and silicon substrate. In order to effectively transmit neuropotential signals, the external interrogator needs to emit a sufficient amount of incident power and the neurorecorder should efficiently modulate and reflect this power. An antenna's ability to reflect power may be evaluated by its radar cross section (Balanis, Antenna Theory: Analysis and Design, 2005),

$$\sigma_R = 4\pi R^2 \frac{S_t}{S_r} = G_{2\omega} \frac{\lambda^2}{4\pi} D_r D_t e_r e_t \tag{2.5}$$

where the lowercase subscripts r and t correspond to receive and transmit modes of the neurorecorder, respectively. R is the distance between the external interrogator and the neurorecorder, S_t and S_r represent the incident and backscattered power flux densities, respectively (magnitude of the Poynting vector or cross product of electromagnetic

waves; $S=|\vec{E}\times\vec{H}|$), $G_{2\omega}$ represents the conversion gain of wireless transmission from f_0 to $2f_0 \pm f_m$ and its value is less than unity for passive systems, and λ is the wavelength of the EM wave transmitted to the neurorecorder in the media that surrounds it. D_r and e_r are the directivity and efficiency of the antenna at f_0, and D_t and e_t are those at $2f_0$. Power received by the microsystem antenna (P_r) may be described by,

$$P_r = S_T A_r$$

$$P_r = \frac{P_T G_T}{4\pi R_1^{\,2}} \cdot \frac{\lambda_1^{\,2}}{4\pi} G_r \tag{2.6}$$

where lowercase subscript r corresponds to reader antenna mode of the microsystem and uppercase subscript T corresponds to transmit antenna mode of the external interrogator. A_r represents the aperture of the receive antenna. R_1 represents distance between transmitting external interrogator and the microsystem receive antenna. λ_1 represents the wavelength at the fundamental f_0 within the transmitting medium. G corresponds to gain and is equal to the product of D and e. Power backscattered or transmitted from the microsystem back towards the external interrogator may be described by,

$$P_t = P_r G_{2\omega} G_t$$

$$P_t = \sigma_R \frac{P_T G_T}{4\pi R_1^{\,2}} \tag{2.7}$$

Finally, power received by the external interrogator (backscattered power) may be described by,

$$P_R = S_r A_R$$

$$P_R = \frac{P_t G_t}{4\pi R_2^{\,2}} \cdot \frac{\lambda_2^{\,2}}{4\pi} G_R$$

$$P_R = \frac{P_T G_T}{4\pi R_1^{\,2}} \cdot \frac{\lambda_1^{\,2}}{4\pi} G_r \cdot \frac{G_t}{4\pi R_2^{\,2}} \cdot \frac{\lambda_2^{\,2}}{4\pi} G_R G_{2\omega} G_t$$

$$P_R = \sigma_R \frac{P_T G_T}{4\pi R_1^{\,2}} \cdot \frac{G_t}{4\pi R_2^{\,2}} \cdot \frac{\lambda_2^{\,2}}{4\pi} G_R \tag{2.8}$$

where λ_2 represents the wavelength at the backscatter $2f_0$ and R_2 represents the distance between the microsystem transmit antenna and the external interrogator receive antenna (in this work, $R_2 = R_1 = R$, since transmit and receive antennas are integrated on the same antenna). It may be seen that in order to increase the power of the backscattered signal, σ needs to be maximized. From Equation (2.5), this may be accomplished by increasing the directivities (D_t and D_r), efficiencies (e_t and e_r), or conversion gain ($G_{2\omega}$) associated with the strength of the nonlinear mixing of the varactors and impedance properties of the antenna and substrate. These parameters were optimized through the design of the respective antennas in HFSS. As was mentioned earlier, the directivity of short slot antennas is constrained to a maximum of 1.76 dBi, and there is little room to improve the efficiency besides changing the frequency. Nevertheless, $G_{2\omega}$ can be increased by stronger nonlinear properties of the varactors and optimizing the impedance of the antenna at f_0 and $2f_0$. The purpose of the MIM capacitors introduced towards the ends of the slot (Figure 2.1(c)) is to provide the degrees of freedom needed to allow this optimization. It should be noted that the above equations (2.5 – 2.8) are valid only for far-field radiation or when the distance separating the two antennas is $R > 2D^2/\lambda$, where D represents the maximum dimension of any of the backscattering microsystem antenna (Balanis, Antenna Theory: Analysis and Design, 2005), which is the mode of wireless transmission the system originally targeted. When the distance is approximately less than

$R \sim 32$ mm, the system may more likely be operating in the radiative near-field where the distribution of EM fields may more accurately be estimated in computational simulation models. Furthermore, enhancing the parameters of the external antenna will relieve some of the limitations associated with the integrated microsystem antenna, as will be discussed in chapter 7.

In its realistic application as implanted in lossy biological media, wireless attenuation becomes a significant factor in backscattering performance. Transmission media include the several organic layers enclosing the brain as well as free-space (air). The relative permittivity (ε_r) of the subcutaneous tissue (skin, fat, and muscle), bone, dura, cerebrospinal fluid (CSF), and the cerebral cortex, can vary from 30 to 65 and depends on the frequency of the pervading microwave signals (Ito, Furuya, Okano, & Hamada, 2001) (Gabriel & Gabriel, 1996). Variations in ε_r directly alter the wavelength and phase velocity of the wireless signals. The conductivity, σ, varies from 0.5 to 2 S/m accounting for real power losses in the radiating waveform. In frequency ranges above the MHz regime, dipolar orientation of water molecules in tissues tends to dominate the dielectric properties (permittivity) of the material. The frequency dependence of the complex permittivity can be modeled using the Cole-Cole equation (Cole & Cole, 1941),

$$\hat{\varepsilon}(\omega) = \varepsilon_\infty + \frac{\varepsilon_s - \varepsilon_\infty}{1 + (j\omega\tau)^{1-\alpha}} + \frac{\sigma}{jw\varepsilon_0} \tag{2.9}$$

where ε_∞ is the permittivity at $\omega\tau >> 1$, ε_s is the permittivity at $\omega\tau << 1$, ε_0 is the permittivity of free-space ($\approx 8.854 \times 10^{-12}$ F/m), α is the distribution parameter, and τ is the relaxation time. From (2.9), radiation losses through the materials surrounding the cortex can be computed for a given frequency. As the frequency increases, signal loss, due to

material or volume conductivity, increases, and this can be estimated by the electromagnetic skin depth, defined as the depth at which current density decreases by *1/e* ≈ *0.37* compared to its value at the surface and given by (Balanis, Advanced Engineering Electromagnetics, 1989),

$$\delta = \frac{1}{\omega\sqrt{\mu\varepsilon}}\left\{\frac{1}{2}\left[\sqrt{1+\left(\frac{\sigma}{\omega\varepsilon}\right)^2}-1\right]\right\}^{-1/2} \approx \sqrt{\frac{2}{\omega\sigma\mu}} \tag{2.10}$$

Therefore, a clear trade-off exists; higher frequencies allow miniaturization of the antenna or implant whereas lower frequencies allow minimization of signal loss in the body. The roundtrip path loss associated with backscattering microwaves through the human head has been modeled, indicating the existence of an optimal frequency of operation near 3 GHz (Poon, O'Driscoll, & Meng, 2010) (Abbaspour-Tamijani, Farooqui, Towe, & Chae, 2008, August).

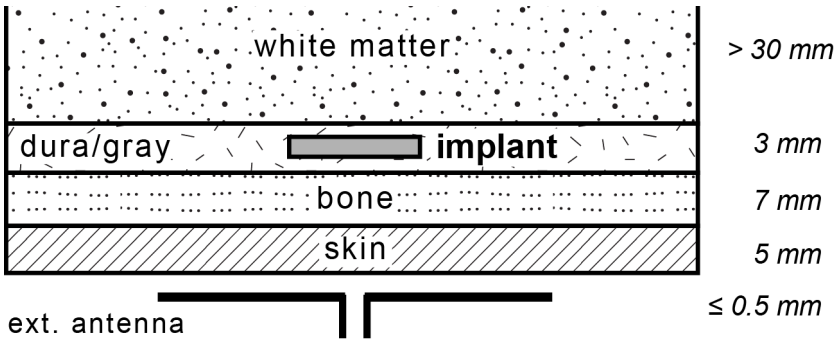

Figure 2.4. Arrangement of head tissue layers, implanted microsystem, and external antenna, with indicated thicknesses of individual biological tissue layers.

Table 2.1. Dielectric properties of human head tissue layers.

Layer		f_0 = 2.45 GHz		f_{IM3} = 4.9 GHz	
		Theory	Measured	Theory	Measured
skin	ε_r	38.0	39	35.8	35
	σ	1.46 S/m	1.5 S/m	2.97 S/m	3.9 S/m
bone	ε_r	11.4	10	10.1	9.4
	σ	0.392 S/m	0.25 S/m	0.945 S/m	0.85 S/m
dura mater	ε_r	42.1	45	39.0	42
	σ	1.67 S/m	1.5 S/m	3.48 S/m	3.9 S/m
gray matter	ε_r	48.9	48	45.3	45
	σ	1.81 S/m	1.5 S/m	3.99 S/m	4.2 S/m
white matter	ε_r	36.2	36	33.5	32
	σ	1.23 S/m	1.5 S/m	2.78 S/m	3.6 S/m

Measured values from coaxial based reflection measurements for phantom tissue layers made for emulating real human head layers for subsequent tests of wireless neurorecording microsystem performance in a physiological relevant dissipative medium. Theoretical values from (Gabriel & Gabriel, 1996).

2.3. Simulation

Simulation of the fully passive wireless backscattering neurorecording system was performed in ADS (Advanced Design System, Agilent) and HFSS (High Frequency Structure Simulator, Ansoft). The work in this section furthers the ground work and analysis originally developed by Dr. Abbas Abbaspour-Tamijani in regards to optimizing wireless neurorecording operation. A brief summary of the basic design and simulation is given here to show how the model is devised for such a fully passive system and how theoretical performance estimates were generated. The physical microsystem less the loading capacitors, varactors, and bypass capacitor was created in HFSS (Figure 2.5) to use a finite element analysis (FEA) to simulate radiation between external interrogator and microsystem in the presence of biological tissue media and obtain antenna

parameters required to analyze harmonic output in subsequent models. This simulation generated s-parameters for the IF port (feed-through electrodes), the pair of varactor ports (trench pads for mounting varactors and connection to antenna), the pair of loading Metal-Insulator-Metal (MIM) capacitor ports (across antenna slot), and the LO and RF port (the latter two are integrated as a single wave port positioned just above the surface of the modeled scalp), which were then imported back into the ADS schematic environment to optimize the value of the loading capacitors for maximal backscattering at the RF frequency. These s-parameters were incorporated into a circuit model in ADS that includes the mixer circuit components: varactors, bypass capacitor, and parasitic elements. Harmonic balance simulations are then performed to verify generation of targeted IM3 harmonic mixing products ($2f_0 \pm f_m$). Figure 2.6 displays the simplified ADS schematic (not including ports for loading capacitors) including a 4-port s-parameter element used to import the high frequency characteristics from the varactor ports, IF port, and mutual LO and RF port, from HFSS simulated results. The estimated spectral response from simulating the ADS circuit is shown in Figure 2.6. The response is for an optimized microsystem with an input (IF) sinusoidal neuropotential of V_m of 100 μVpp sinusoidal at f_m of 1 kHz, and LO incident power of P_0 of 1 mW (0 dBm) at f_0 of 2.4 GHz. The plot shows the targeted third-order mixing products $2f_0 \pm f_m$, demonstrating a signal-to-noise ratio (SNR) of 30 dB (assuming a noise floor of -135 dBm). The simulations do not take into account various wireless environmental disturbances, such as noise or structural reflections along with a large amount of loss caused by fabrication related imperfections that would add considerable parasitics to the overall circuit and diminish SNR.

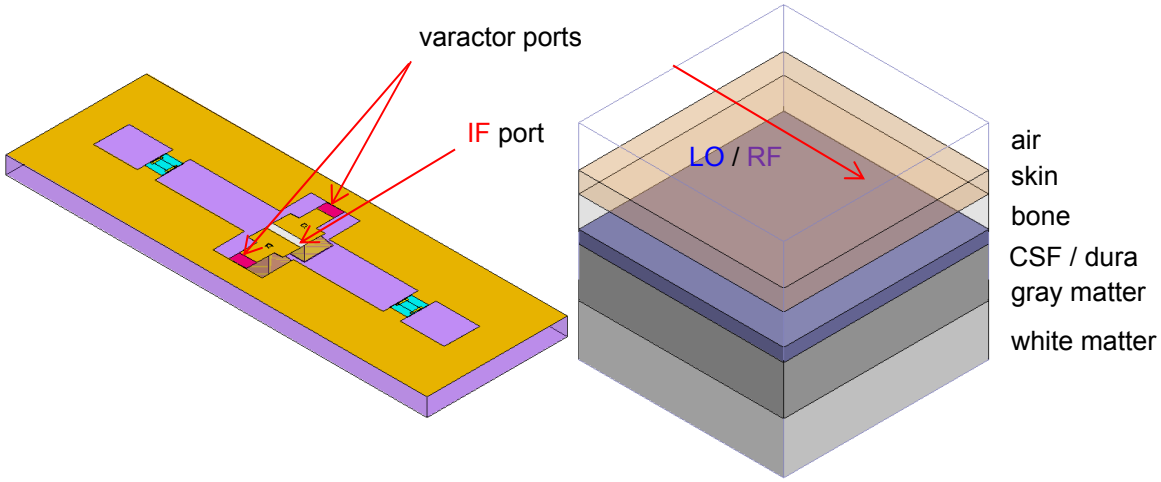

Figure 2.5. HFSS layout figures. The microsystem (left) is simulated in HFSS as embedded inside a striated box of tissue layers and air (right) representing the various human head tissue layers that wireless signals will traverse. The LO/RF radiation port is placed on the topmost air boundary surface to supply LO excitation and concurrently measure reflected RF signals.

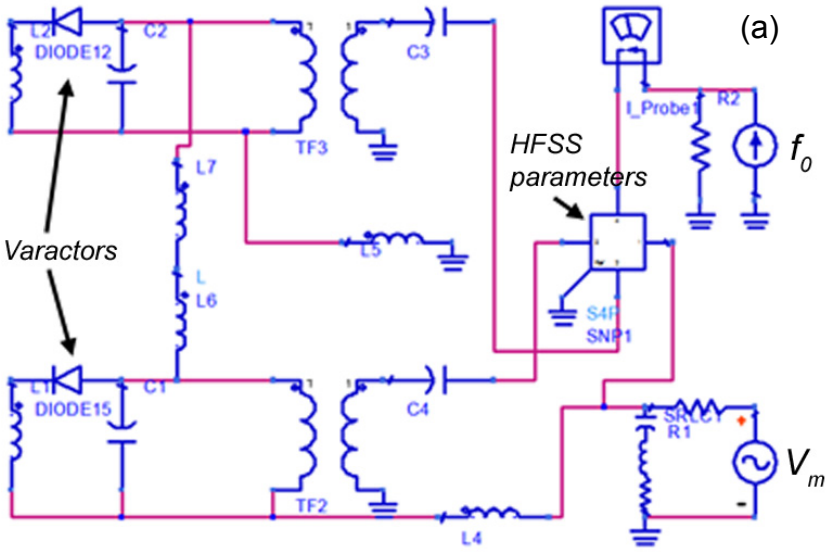

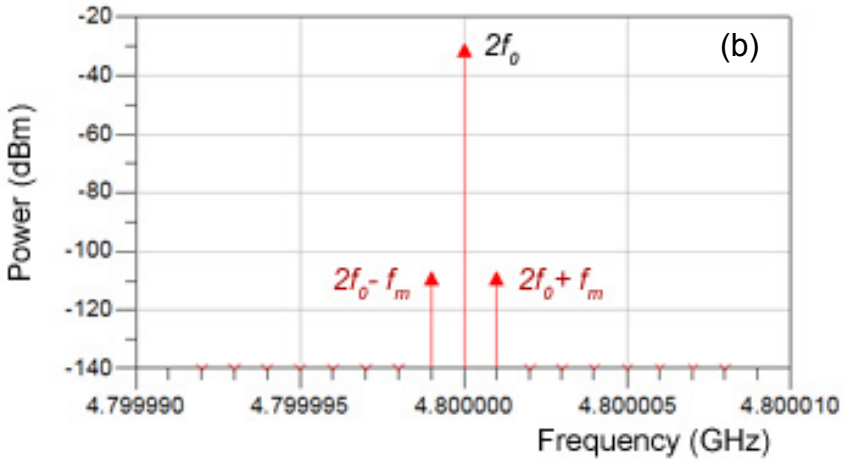

Figure 2.6. Circuit model and harmonic balance simulation in ADS. (a) Simplified ADS harmonic balance circuit schematic of the microsystem. Varactors are represented as nonlinear diodes with parasitic elements. The 4-port s-parameter element imports values from HFSS to model the high-frequency characteristics of the microsystem. The LO (f_0) is modeled on the top right and the neuropotentials (V_m) as an AC-source (bottom right). (b) Simulated backscattering spectral response with V_m of 100 μV_{pp} sinusoidal at f_m (IF) of 1 kHz, incident radiated power, P_0, of 1 mW (0 dBm) at f_0 of 2.4 GHz. Targeted IM3 harmonics $2f_0 \pm f_m$ are clearly seen around the $2f_0$ carrier and have amplitudes of ~ -115 dBm (SNR ~ 20 dB for a noise floor of ~ -135 dBm).

CHAPTER 3

FABRICATION OF A FULLY PASSIVE NEURORECORDER

The neurorecording microsystem was fabricated on a high resistivity (10 kΩ·cm) p-type (100) silicon wafer. The cross-sectional fabrication process flow is depicted in Figure 3.1. Standard photolithography and micromachining techniques were used for fabrication in a class 100 cleanroom at the Center for Solid State Electronics Research (CSSER) in ASU.

Initially, a low-stress non-stoichiometric 600 nm thick silicon nitride (SiN_x) followed by an 800 nm thick silicon dioxide (SiO_2) films were deposited using low-pressure chemical vapor deposition (LPCVD) at 250 mTorr and 800 °C and thermal wet oxidation at 1050 °C, respectively or radio frequency chemical vapor deposition (RPCVD) at 300 °C. These layers serve as electrical isolation to prevent conductive paths of subsequent layers to the silicon substrate. Reactive ion etching (RIE) process parameters that were consistent throughout the fabrication process, for SiN_x etching were a pressure of 50 mTorr, RF power of 150 W, CHF_3 flow rate of 50 sccm, and O_2 flow rate of 5 sccm, and for SiO_2 etching were 30 mTorr, 200 W, CHF_3 at 25 sccm, and Ar at 25 sccm. Process uniform photoresist-based photolithography involved precleaning in acetone + IPA + distilled (DI) H_2O + N_2 spray, dehydration bake (100°C, 20 min.), spinning 2000 rpm AZ4330 photoresist (~ 4.5 μm thick), curing on a hot plate (100°C, 90 sec.), UV exposure through a mask (EVG620) at 400 mJ/cm^2, developing in 300MIF developer for ~ 3 – 3.5 min, and rinsing in DI H_2O for 1 min + N_2 dry for 1 min. The fabrication process is detailed in the following list.

1) Trenches for off-chip varactor mounting: Shallow trenches (50 μm deep) were etched into the substrate using RIE of the SiN_x and SiO_2

films, and 30% wt. potassium hydroxide (KOH) anisotropic etching of the silicon substrate. These trenches are for mounting off-chip varactors for subsequent assembly. The trenches were then insulated by depositing another 600 nm thick SiO_2 film on the topside using plasma-enhanced chemical vapor deposition (PECVD) at 500 mTorr and 300 °C.

2) Feed-through electrodes (from backside): Si exposing windows for patterning through-hole interconnects were formed on the backside by RIE of backside SiO_2 and SiN_x layers. Through-hole interconnects were routed by anisotropic etching using 30% wt. KOH solution at 100°C for an etch rate of about 3.5 μm/min for 180 minutes, until the topside SiN_x was exposed. The exposed silicon vias on the backside were insulated by a 600 nm thick SiO_2 film (PECVD at 500 mTorr and 300 °C).

3) Neuropotential recording electrodes: A conductive Cr/Au (40/200 nm) film was deposited on the backside using thermal evaporation. The layer was thickened to ~ 10 μm by electroplating (TSG-250) at a rate of 1 mA/cm^2 at ~ 60°C. The conductive layers were patterned using wet etchants (1020, GE-8148) to form the two backside terminals to directly attach to tissue and interface neuropotentials.

4) Feed-through electrodes (from topside): 50 μm wide square via holes were etched into the topside SiN_x and SiO_2 films by RIE to uncover the backside deposited Cr/Au layer.

5) Neuropotential recording electrodes (topside contacts) and bottom MIM capacitor bottom electrode: Cr/Au (40/200 nm) films were thermally evaporated onto the topside to close the electrical path from backside terminals to topside contacts, completing the through-hole interconnects and allowing neuropotentials acquired from backside electrodes to connect to circuitry on the topside. These topside Cr/Au films also serve as bottom contacts for soon after generated MIM capacitors.

6) MIM capacitor dielectric: A SiO_2 film (200 nm) was deposited and patterned on the topside using PECVD at 500 mTorr and 150 °C and RIE, respectively, to form the dielectric layer of the MIM capacitors.

7) Antenna and MIM capacitor top electrode: Cr/Au films (40/200 nm) were evaporated thermally on top of the preceding SiO_2 layer and patterned to form the top contacts of the MIM capacitors as well as the slot antenna.

Following fabrication, circuit assembly simply involved mounting of flip chip varactors into the trenches of the fabricated microsystem using silver epoxy (Epo-Tek H22) (cured at 160°C for 20 minutes), installing sufficiently thin steel wires onto the backside electrical terminals for ease of subsequent testing, and supplying neuropotential signals to the microsystem. Following assembly, a conformal 4 – 10 μm thick parylene was coated to encapsulate the microsystem in a biocompatible package. The fabricated neurorecording microsystem is shown in Figure 3.2.

During post-fabrication inspection, peeling of topmost conductive Au film (antenna and top MIM electrodes) and DC leakage through MIM capacitors on several dies were frequently observed. The metal peeling and leakage were due to poor adhesion and non-uniformity of the PECVD SiO_2 film, respectively. These shortcomings were mitigated by increasing the thickness of the Cr seed layer and better controlling the uniformity of PECVD SiO_2, respectively.

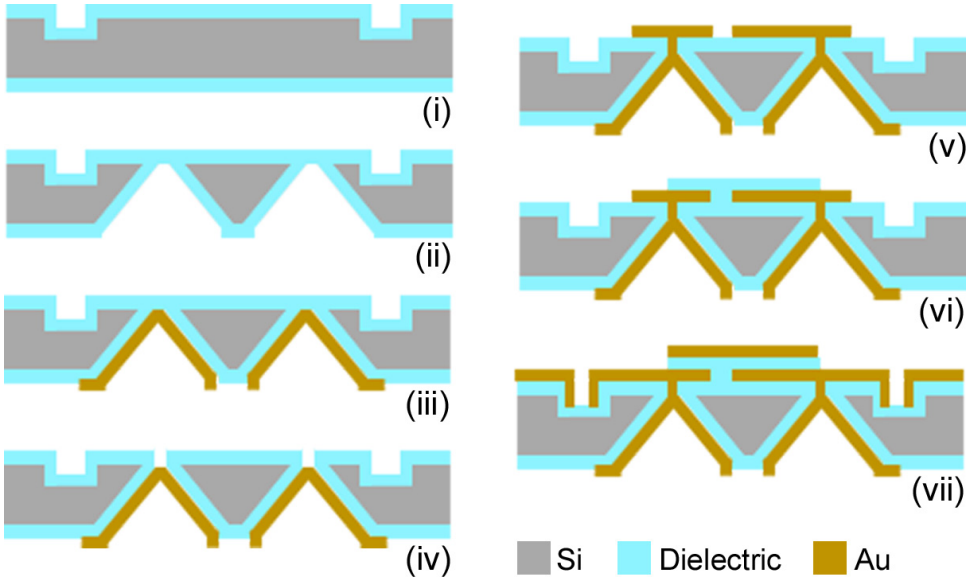

Figure 3.1. Cross-sectional process flow. (i) patterning/insulation of topside trenches, (ii) bulk etching/insulation of backside through-hole interconnects, (iii) deposition of conducting terminals from backside, (iv) topside etching of vias to expose backside conducting terminals, (v) topside deposition of conductive interconnect to bottom terminals and bottom MIM capacitor electrodes, (vi) topside deposition of SiO_2 dielectric for MIM, and (vii) deposition and patterning of antenna, top MIM electrodes, and varactor pads in trenches.

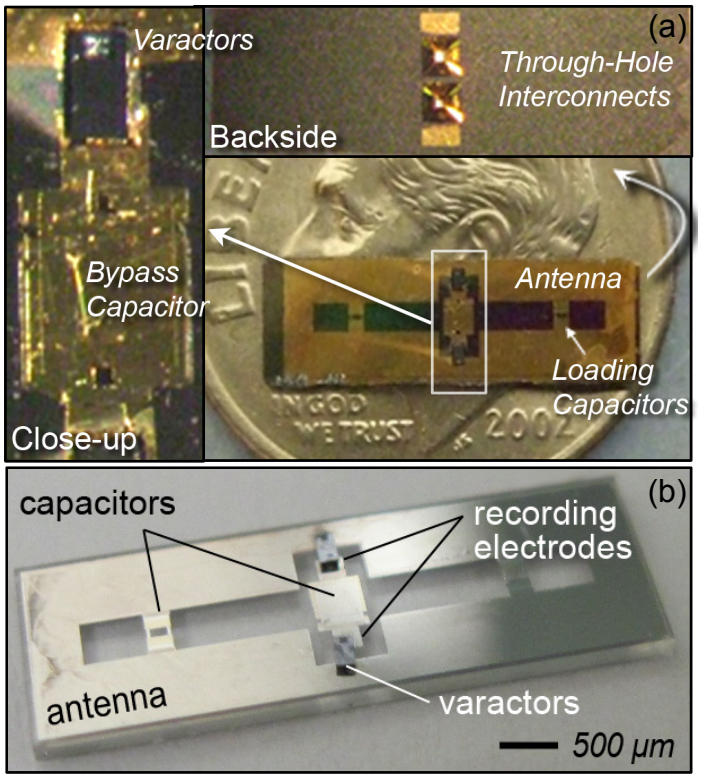

Figure 3.2. Photograph of fabricated devices. (a) A fully passive neurorecording microsystem on high resistivity silicon with through-hole recording electrodes above a US dime, for visual scaling. A close-up of the bypass MIM capacitor and varactor component mounted in the trench is shown on the left. The microsystem is flipped in the top figure to display backside through-hole interconnects where neuropotentials are acquired. (b) A neurorecording microsystem fabricated on a glass substrate for lower loss and without through-hole electrodes.

CHAPTER 4

TESTING OF A FULLY PASSIVE NEURORECORDER

Wireless testing of the fully passive neurorecording microsystem involved three different environments: using a function generator to supply emulated neuropotentials, using real frog sciatic nerves to supply compound action potentials (CAPs) to be wirelessly recorded, and implanting of the microsystem in a human head mimicking phantom to test wireless backscattering performance in a lossy physiologically relevant medium. The external interrogator was improvised as needed to provide a low noise carrier to activate recording and backscattering operations of the microsystem and detect backscattered nonlinear harmonics carrying targeted neuropotential signals in the form of a frequency spectrum and/or downconverted to baseband temporal form.

4.1. External Interrogator

The external interrogator incorporates a linearly tapered slot antenna (LTSA) as the wideband wireless link (Janaswamy, Schaubert, & Pozar, 1986) (Yngvesson, Schaubert, Korzeniowski, Kollberg, Thungren, & Johansson, 1985) having dual band radiation channels (where return loss > 7 dB) at 2.3 – 2.7 GHz (for transmission at LO (f_0)) and 4.25 to 5.5 GHz (for receiving at RF ($2f_0 \pm f_m$)). The antenna also combines a diplexer to isolate transmit and receive channels; essentially a low pass filter (LPF) at the incident frequency band (transmitter, f_0) and a high pass filter (HPF) at the backscatter frequency band (receiver, $2f_0 \pm f_m$). For monitoring backscattered RF spectra, a spectrum analyzer (Agilent E4448A) was directly connected to the RF output of the LTSA, having a noise floor of around -135 to -138 dBm for a 1 kHz bandwidth at the frequencies of

interest. To downconvert and demodulate RF signals, an RF synchronous demodulator was used, as shown in Figure 4.1. The demodulator was constructed to retrieve the original neuropotential signals at baseband. The incident LO exciter is produced using a signal generator (2002B Wavetek, Agilent E4432B, or HP 8341A) outputting a continuous wave (CW) signal in the frequency range of 2.3 to 2.7 GHz and power range of 0 to 16.7 dBm, respectively, and is amplified, as needed, through a broadband amplifier (ZHL-42 Mini-Circuits). To suppress higher harmonics exacerbated by the amplifier, one to two stages of band-pass filters (BPF) around f_0 is connected to the amplifier's output. The LO signal is then connected to the LO port of the LTSA. Through a splitter, the carrier signal is also fed to a frequency doubler (FDR-4-8 RF Bay) to produce a $2f_0$ reference used to downconvert the RF backscattered signals ($2f_0 \pm f_m$) to baseband (f_m). Direct downconversion is performed through a mixer (ZX05-153LH+ Mini-Circuits) where its LO port inputs the reference of $2f_0$ and its RF port inputs the backscattered signals ($2f_0 \pm f_m$) from the LTSA's RF output. Before the signals are fed to the mixer, both the reference ($2f_0$) and backscattered signals ($2f_0 \pm f_m$) pass through multiple stages of amplification through low noise amplifiers (LNA-6G RF Bay) and BPF's around $2f_0$. This preamplification and filtering helps improve the final signal to noise ratio (SNR) since noise contributions nearer to the antenna cascade and will affect the final SNR more than noise introduced further down the chain. Overall noise figure ($F_{1\text{-}n}$) of the cascaded components may be calculated by

$$F_{1-n} = F_1 + (F_2 - 1)/G_1 + (F_3 - 1)/G_1G_2 + \ldots + (F_{n-1})/G_1G_2 \ldots G_{n-1} \tag{4.1}$$

where F_n represents individual noise figures, G represents individual gain, and the subscripts ($1,2,\ldots n$) represent the order of the components starting from closest to the

antenna. Individual noise figures are deduced by the thermal noise characteristics of an individual component, $N=kT_o\Delta f$, where k represents Boltzmann's constant (1.381×10^{-23} J/K), T_0 represents temperature (K), and Δf represents bandwidth. The mixer multiplies the reference LO ($2f_0$) and the backscattered RF ($2f_0 \pm f_m$) inputs to produce the baseband output (f_m). This baseband output is fed into an amplifier and filter (SR560, Stanford Research Systems) with a variable gain of ~ 40 – 50 dB around the passband of ~ 0.5 Hz to 3 kHz. Specific demodulator component parameters are listed in Table 5.1. Overall wireless system performance is defined mostly by noise in the exciter (LO at f_0) and by the noise figures of components (amplifiers) near the antenna, as indicated in equation 5.1. Noise in the microsystem originates from only a relatively few sources mainly associated with thermal noise generated by the imperfect resistive components of the antenna and from the electrode-tissue interface. Input power of LO is limited to ~ 47 mW (16.7 dBm), which produces an approximate brain tissue absorbed power density of the radiated fields, or SAR, of less than 120 mW/kg, as computed in HFSS. This estimated SAR is in compliance with the exposure guideline set forth by U.S. FCC of 1.6 W/kg for personal wireless communication devices over a volume equivalent to 1 g in the head (Means & Chan, 2001).

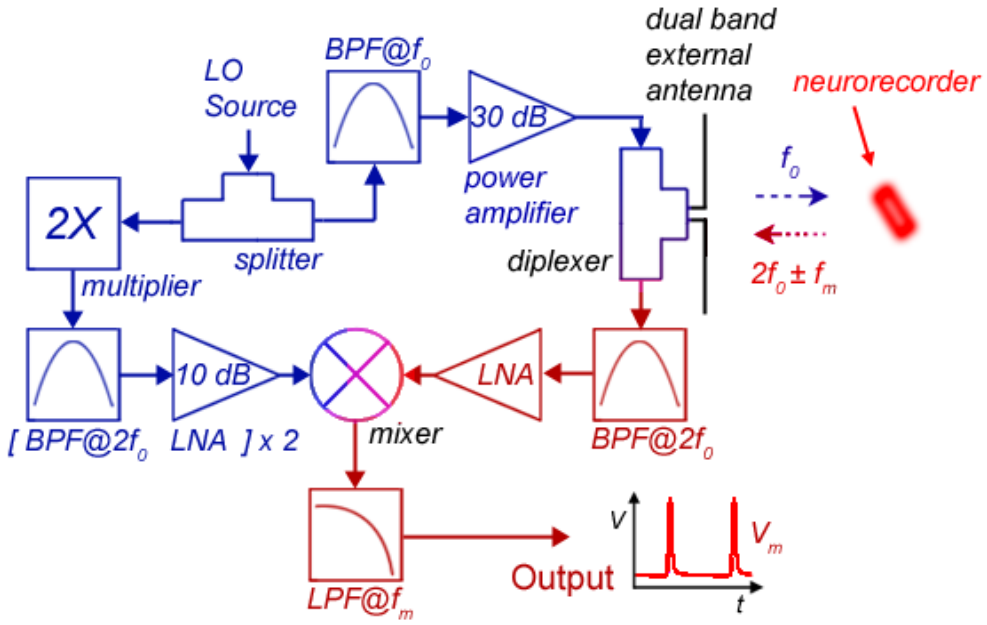

Figure 4.1. Block diagram of demodulator; blue colors represent transmitting and red, receiving. The backscattered third order harmonics ($2f_o \pm f_m$) are received by the antenna and demodulated to recover original neuropotentials (f_m).

Table 4.1. Demodulator component parameters.

LTSA LO (f_0) Input		
BPF @ f_0 (VHF-1910+)	2.2 – 4.4 GHz (passband)	Also after amplifier
Amplifier (ZHL-42)	30 dB (gain)	
Mixer LO ($2f_0$) Input		
Frequency Multiplier (x2)	14 dB (conversion loss)	
LNA (LNA-6G)	22 dB (gain)	Also after BPF
BPF @ $2f_0$ (VHF-3100+)	3.4 – 9.9 GHz (passband)	Also after 2nd LNA
LTSA RF ($2f_0 \pm f_m$) Output / Mixer RF Input		

LNA (LNA-6G)	20 dB (gain)	Also after BPF
BPF @ $2f_0$ (VHF-3800+)	4.25 – 10 GHz (passband)	Also after 2nd LNA
Mixer IF (f_m) Output		
LPF (SR560)	3 – 5 kHz (cut-off)	
HPF (SR560)	0.5 – 100 Hz (cut-off)	
Amplifier (SR560)	50 dB (gain)	

4.2. Testing with emulated neuropotentials

Emulated neuropotentials from a function generator (Agilent 33250A) were used to characterize the wireless backscattering response of the microsystem. These benchtop tests were performed in the facilities and with the equipment provided by ASU's Connection One wireless testing labs, Dr. Félix Miranda at NASA Glenn Research Center (Antenna and Optical Systems Branch), and/or by Prof. Bruce Towe at ASU's biomedical engineering department. Various waveforms (sinusoid, square, triangle), in the range of 1 to 50 mV_{pp} and 10 Hz to 5 kHz, were applied to the backside terminals of the microsystem. Incident power supplied from the signal generator ranged from 0 to 16.7 dBm (1 to 47 mW). The strength of the backscattered signals was quantified by the power of the modulating $\pm f_m$ components around the second harmonic ($2f_0 \pm f_m$) collected by the external interrogator. The minimum detectable signal (MDS) was set to -130 dBm, indicating that the modulating $\pm f_m$ components should be at least 5 dB greater than the noise. An example of the spectral response, a 3.4 mV_{pp} sinusoidal input at a distance of 2.5 mm, is shown in Figure 4.2(a) (Schwerdt, et al., A fully-passive wireless microsystem

for recording of neuropotentials using RF backscattering methods, 2011). The recovered waveforms at baseband are shown in Figure 4.2(b), for sinusoid, square, and triangle emulated neuropotentials of 3 mV_{pp} at 800 Hz. For a sinusoid 1 mV_{pp} input of 1 kHz, the demodulator yielded an SNR of around 1.5. The maximum wireless detection range was limited to 15 mm for neuropotentials below 50 mV_{pp}. For neuropotentials in the range of few *millivolts*, the microsystem needed to be placed within 2 mm from the external interrogator. Measured emulated signals of 50 mV_{pp} as a function of distance between the neurorecording microsystem and the external interrogator are plotted in Figure 4.2(b). The expected wireless attenuation trend of these signals in the far-field is also plotted as a solid gray line in Figure 4.3 for relative comparison.

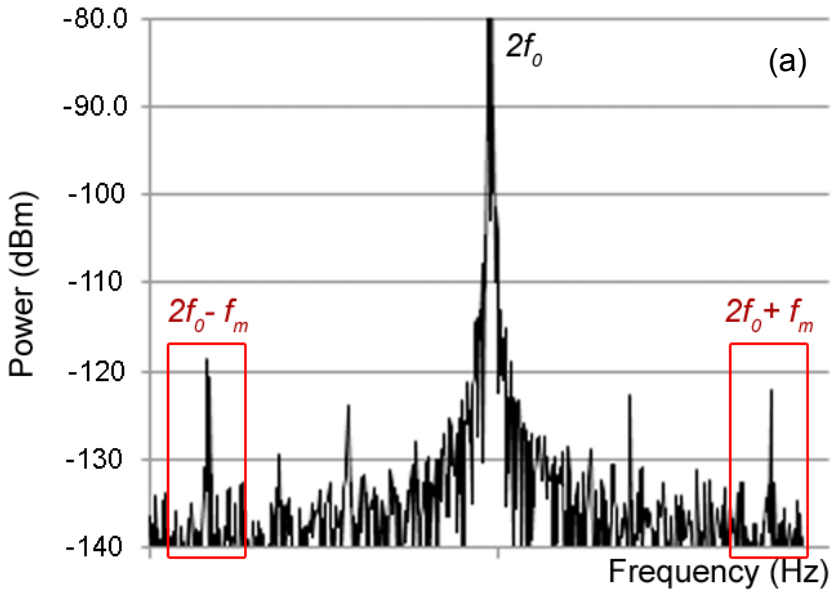

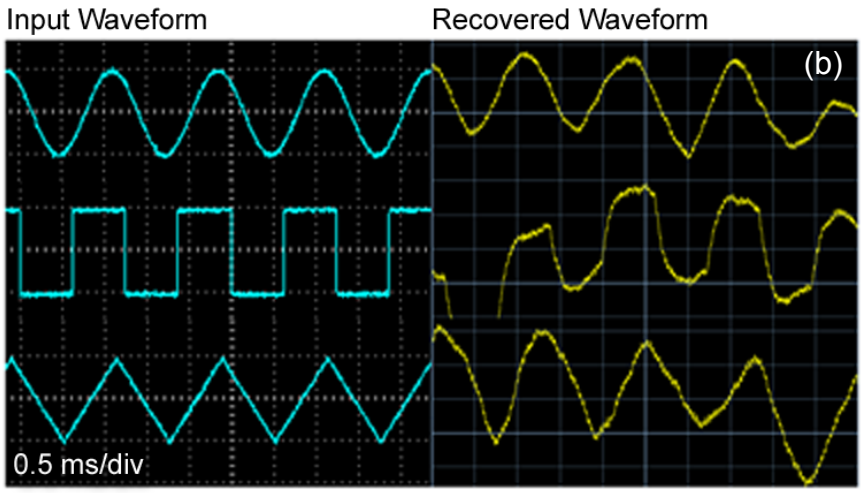

Figure 4.2. Measurement results of the fully passive wireless neurorecording microsystem. (a) Measured wireless spectral response for a wireless distance of 2.5 mm, V_m of 3.4 mV_{pp} at f_m of 400 Hz, P_0 of 14.8 dBm (33.1 mW) at f_0 of 2.2 GHz. The targeted modulating components associated with the neuropotentials ($2f_0 \pm f_m$) are highlighted in red. Low frequency harmonic noise components (120 and 240 Hz) are also seen modulating the $2f_0$ harmonic. (b) Demodulated emulated waveforms of sinusoid (top), square (middle), and triangle (bottom) forms. The input emulated waveforms into the neurorecording microsystem have a V_m of 3 mV_{pp} at f_m of 800 Hz and are shown on the left (cyan) and the wirelessly demodulated waveforms from the external interrogator are shown on the right (yellow). A low frequency noise (120 Hz) also exists here, as may be noticed by the slower oscillating component.

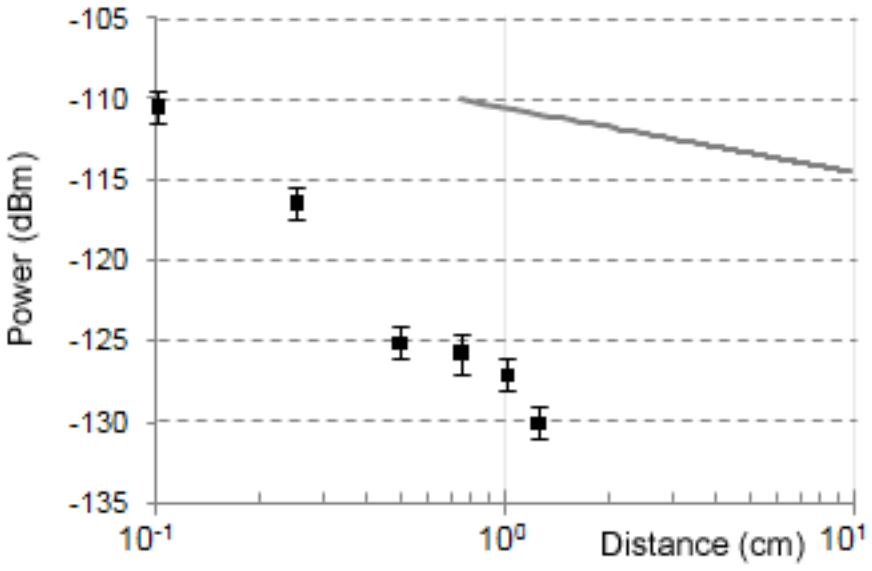

Figure 4.3. Backscattered power of targeted harmonics ($2f_0 \pm f_m$) received by the external interrogator as a function of its distance from the microsystem: in the far-field the free-space attenuation is proportional to $(4\pi R^2/\lambda)^2$, as seen by the solid gray line. An input V_m of 50 mV_{pp} at f_m of 400 Hz was used to acquire the signals. The discrepancy between the predicted power (solid gray line) and the measured power is likely due to the near-to-far-field transition.

4.3. Testing with real nerves

The microsystem was tested using neuropotentials in the form of compound action potentials (CAPs) from the frog sciatic nerve. These tests were carried out in the facilities of Prof. Bruce Towe. The frog was terminated immediately before conducting wireless experiments to ensure viability of its nervous system. All animal testing followed proper animal care guidelines of ASU's Institutional Animal Care and Use Committee (IACUC). The magnitude of an electrical stimulation pulse determines the number of neurons recruited for generating a CAP. The superimposing of concurrent

action potentials propagating through a bundle of nerves result in CAPs. A biphasic square waveform with a pulse-width of 0.2 ms (cathodic stimulation pulse followed by anodic-charge balancing pulse) was used as the current stimulus. Electrode wires were connected from the frog's sciatic nerve to the microsystem electrodes. Recording electrode were also connected directly to the oscilloscope to monitor original CAPs before wireless transmission. The microsystem was placed within 5 mm to the external interrogator. Stimulating electrodes were placed on the sciatic nerve approximately 10 mm above the terminals of the microsystem. CAPs were evoked at a rate of 2 to 140 Hz and were within the range of ~ 500 to 1000 μV_{pp}, as recorded by the microsystem. As these signals are near the overall system noise level and difficult to directly record, the potential to use such an approach with improvements in demodulation technique was investigated by using 128 epoch signal averaging of the repetitive CAP response to achieve an SNR improvement of 11.3. An example of the signals acquired from the frog's sciatic nerve is displayed in the bottom plot of Figure 4.4, where the CAPs measured to have a V_m ~ 500 μV_{pp} at f_m of 140 Hz. For verification purposes, the CAPs were also recorded directly with electrodes attached to the sciatic nerve and amplified are shown in the top plot. Spikes seen in between individual CAP cycles are stimulation artifacts from the current induced excitation of the sciatic nerve. The data are encouraging as it suggest that reducing noise in the receiver system in the future may remove the need for averaging to be able to detect less predictable non-periodic neuropotentials.

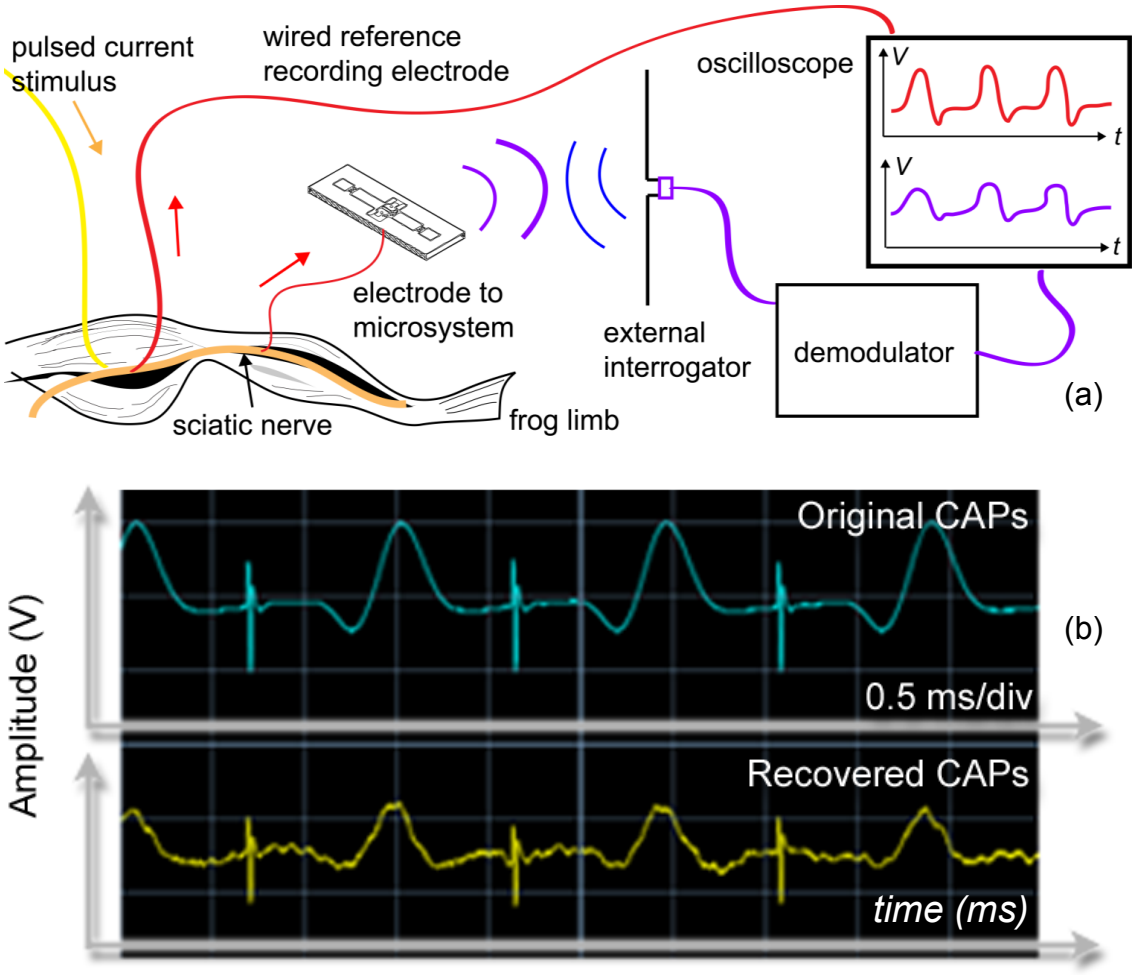

Figure 4.4. Measured and demodulated frog neuropotentials from a frog sciatic nerve. (a) Setup for wireless neurorecording of CAPs from frog sciatic nerve. (b) The original frog CAP waveforms, as measured directly from reference wired electrodes, are shown on the top (cyan). The CAPs have a measured V_m ~500 μV_{pp} at f_m of 140 Hz. Wirelessly recovered neuropotentials, as measured and wirelessly retrieved from the backscattering neurorecording microsystem, are shown on the bottom (yellow). The abrupt spikes interleaved between CAPs are stimulation artifacts from current induced excitation of the nerves. 128 epoch signal averaging of repetitive signals was used during demodulation for measuring the bottom recovered CAP waveforms.

4.4. Testing in emulated human head media

To demonstrate the efficacy of the microsystem within dispersive biological media, a semi-solid multilayer phantom emulating the lossy properties of the human head was constructed and used for testing the performance of the wireless backscattering microsystem as supplied with emulated neuropotentials (Schwerdt, Chae, & Miranda, Wireless performance of a fully passive neurorecording microsystem embedded in dispersive human head phantom, 2012, July) (Schwerdt, Miranda, & Chae, A fully passive wireless backscattering neuro-recording microsystem embedded in dispersive human head medium, 2012). The following tests were carried out in the facilities of NASA Glenn Research Center (Antenna and Optical Systems Branch) under the guidance of Dr. Félix Miranda. Individual phantom layers (skin, bone, dura, gray matter, white matter) were created by heating a mixture of distilled water, agar, NaCl, boric acid, TX-151, and polyethylene powder (Ito, Furuya, Okano, & Hamada, 2001). Open-ended coaxial probe measurements (85061E, Agilent) were performed on each layer to verify permittivity properties prior to merging all layers (Figure 4.5). Wireless testing was prepared by embedding the microsystem into the dura stratum of the phantom. A schematic of the test setup is shown in Figure 4.6. Three different microsystems were tested in this experiment, each harboring a different substrate (low resistivity silicon, high resistivity silicon, and glass) and each uniformly coated with parylene-C to prevent conductive shorting to the phantom medium. Testing with emulated neuropotentials was performed in the same manner as delineated in prior sections. The ratio of received backscattered power ($P_R = P_{IM3}$ or power of the third order harmonics at $2f_0 \pm f_m$) to

externally transmitted P_0 as a function of depth of the microsystem in phantom is plotted in Figure 4.7. The average observed SNR for the three different types of microsystems are tabulated in Table 4.2. The minimum detectable signal of the microsystem in the phantom was V_m = 6 mV_{pp}. The type of substrate harboring the microsystem did not noticeably alter performance, except for the low resistivity silicon (LR Si) that failed to demonstrate any effective operation. Based on reverse calculation of the experimental results, the antenna transmission gain may be crudely approximated. For a 50 mV V_m in phantom (equivalent to P_m ~ -13 dBm input power) undergoing ~15 dB mixer conversion loss (based on simulation) and then ~ 20dB path loss in tissue (based on measurements in phantom as shown in Figure 4.7) (-13-15dB-20dB), so the backscattered signal is produced from a combination of factors P_{IM3} (dBm) ~ P_m (dBm) + $G_{2\omega}$ (dB) + G_t (dB) + G_{path} (dB) + G_R (dB), where G_t is the microsystem transmit gain (unknown), G_{path} is the path loss in tissue (~ 20 dB), and G_R is the external antenna receive gain (~ 0 dB). For a P_{IM3} = -120 dBm that is typically detected in measurements, G_t ~ -72 dB, which is very poor, but then again this may be an inaccurate estimation because the varactor $G_{2\omega}$ is probably much lower in physical operation than simulated estimates. It may be more accurate to simply express that the collective losses of the varactor mixer ($G_{2\omega}$) and antenna backscatter gain (G_t) are collectively ~ -87 dB.

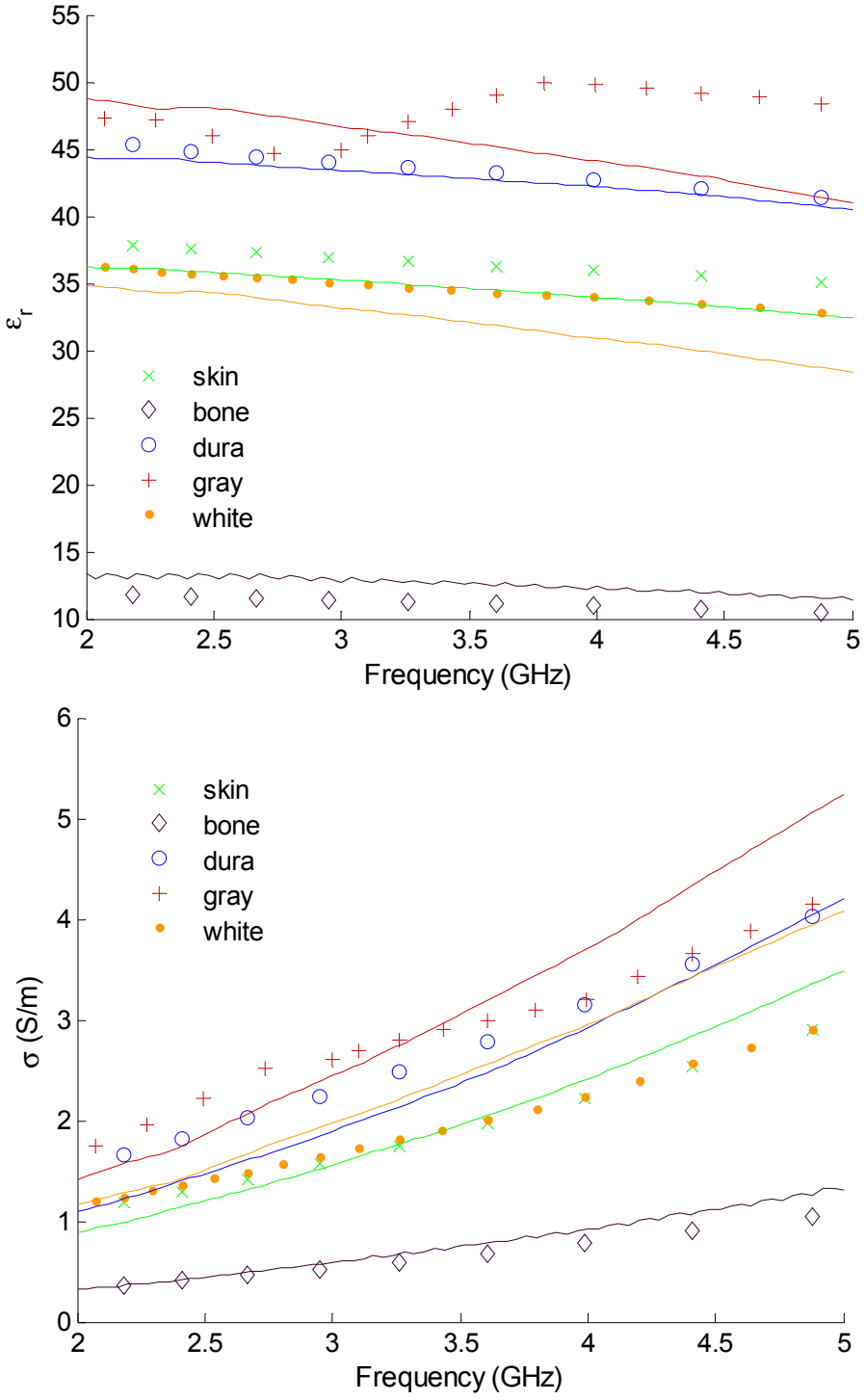

Figure 4.5. Plot of complex permittivity (ε_r, top, and σ, bottom) for real (symbol) and measured phantom (solid) human head tissue layers (Gabriel & Gabriel, 1996).

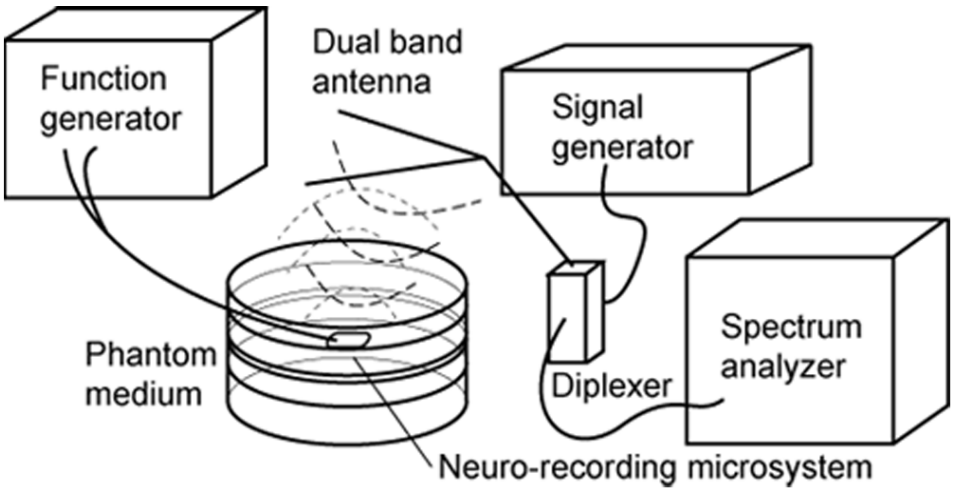

Figure 4.6. Wireless benchtop setup for phantom testing. The function generator (Agilent 33250A) supplies $V_m \sim 1 - 50$ mV_{pp} at $f_m = 10$ Hz – 5 kHz to the microsystem. The signal generator (Agilent E4432B or HP 83241A) supplies LO power, $P_0 = 0 - 16.7$ dBm, at $f_0 = 2.4 - 2.45$ GHz. The spectrum analyzer (Agilent E4448A) monitors the wirelessly backscattered RF signals containing targeted neuropotentials, at $2f_0 \pm f_m$. The diplexer is integrated directly onto the antenna and effectively isolates LO and RF signals transmitted and received by the external antenna, respectively.

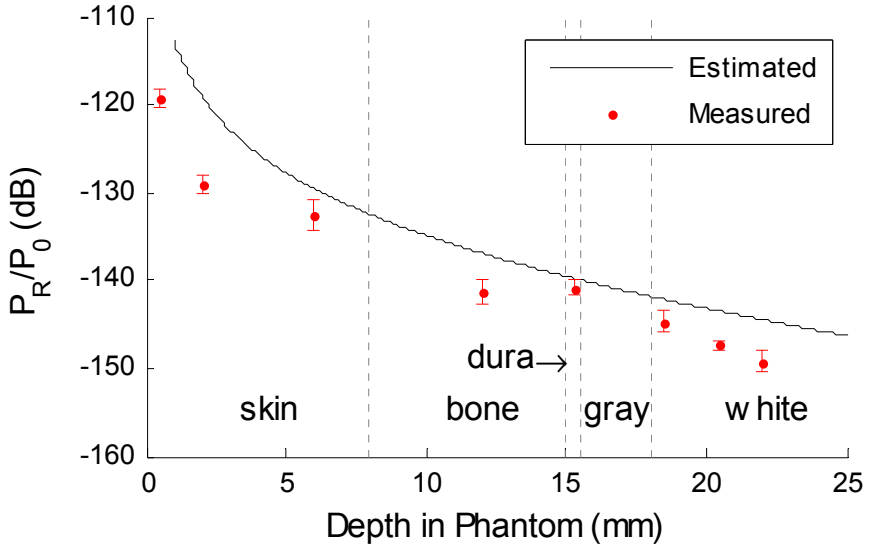

Figure 4.7. Plot of measured P_R/P_0 ratio (where $P_R=P_{IM3}$ or the power of the backscattered power at $2f_0 \pm f_m$ and P_0 is the power supplied to the external wireless interrogator) as a function of microsystem depth into the phantom media along with a theoretical estimated curve for comparison (Equations 2.8, 2.10). Error bars indicate the standard deviation range over multiple measurements.

Table 4.2. Comparison of SNR for three different substrates.

Microsystem Substrate	*Free Space*	*Phantom*
Low Resistivity Si (LR Si)	0 dB	0 dB
High Resistivity Si (HR Si)	38.9 dB	22.0 dB
Glass	36.6 dB	21.3 dB

Table 4.3. Summary of measured specifications of the fully passive neurorecorder

Footprint	Dimensions	$12\times4\times0.5\ mm^3$
Detected Input Signals	Bandwidth	*5 – 3000 Hz*
	Amplitude	$\geq 500\ \mu V_{pp}$
	Distance	$\leq 1.5\ cm$

RF Transmission	Radiated Power	*0 – 16.7 dBm*
	Frequency	*2.2 – 2.45 GHz*
RF Reception	Sideband Level	*≤ -105 dBm*
	Noise Floor*	*≈ -134 dBm*
	Frequency	*4.4 – 4.9 GHz*
Thermal	ΔT	*≤ 0.15 ± 0.1°C*
	SAR (estimated)	*≤ 0.112 W/kg*

*Noise floor imposed by external receiver instrumentation (ie. spectrum analyzer)

CHAPTER 5

IMPLANT SAFETY ANALYSIS

In order to assure minimal risk in operating wireless brain implantable devices, it is vital to assess the impact of heat emanated by integrated circuit as well as impinging EM waves in the human body. In this work, the analysis of safety is especially relevant as the fully passive scheme is set forth to rectify virtually all heat related trauma commonly introduced by implant electronics. The practical utility of implantable neurorecording systems in the clinical and scientific fields can only be realized by ascertaining their safety and long term reliability. In order to conform to the stringent safety requirements of chronic brain implantation, considerable research has been devoted to enhancing device aspects such as biocompatibility (Wise, Sodagar, Yao, Gulari, Perlin, & Najafi, 2008) (Marin & Fernandez, 2010) (Ward, Rajdev, Ellison, & Irazoqui, 2009), miniaturization (Kipke, et al., 2008), elastic material platforms (Blount, Cormier, Kim, Kankirawatana, Riley, & Knowlton, 2008), and power or heat management (Kim, Tathireddy, Normann, & Solzbacher, 2007) (Abbaspour-Tamijani, Farooqui, Towe, & Chae, 2008, August). These requirements have been expressed in chapter 1, and are reinstated here in greater detail as applicable to this analysis on implant safety. A biocompatible encapsulation of the implant is needed to avoid evoking immune reaction or harmful response from the human body (Marin & Fernandez, 2010) (Ward, Rajdev, Ellison, & Irazoqui, 2009). Miniaturization and/or translation to more compliant materials are also needed to minimize the implant's physical obtrusion and contortion of the brain (Kipke, et al., 2008) (Wise, Sodagar, Yao, Gulari, Perlin, & Najafi, 2008). On top of these chemically or mechanically instilled perturbations, an important safety

concern is associated with the actual operation of the implanted device as relates to the heat dissipated by the embedded electronics or by the permeating wireless EM fields into surrounding tissue (Vidal & Lopez, 2010). Temperature rises greater than 1 °C have been shown to induce irreversible damage on the brain (LaManna, McCracken, Patil, & Prohaska, 1989). Therefore, it is imperative to limit the heat generated by the cortically implanted device. Heat may be generated by the implant in two ways: by the heat dissipated by internal circuitry that is directly related to the power consumed by the circuits and power supply/regulatory elements and/or by the absorption by the dissipative tissue medium of induced wireless power in the form of propagating EM waves. As the fully passive neurorecording microsystem operates exclusively by means of wireless EM backscattering in the absence of onboard active electronics or internal powering elements, the present study focuses on characterizing induced EM fields associated with operation of the microsystem that may be correlated to potentially adverse thermal consequences. Thermal analyses for active wireless multichannel MEA implant circuits have been performed in the past using FEA and infrared (IR) thermography in brain phantom and *in vivo* (Kim, Tathireddy, Normann, & Solzbacher, 2007). This prior work estimated the heat dissipated by the microsystem IC (integrated circuit) by mounting Ti/Pt micro heating elements onboard the MEA to emulate IC power dissipation. The study demonstrated a temperature profile of 0.029 °C/mW due to power dissipated by the IC or an equivalent maximum temperature rise of 0.38 °C (at 13 mW). However, unlike prevalent low frequency inductive coupling systems, the fully passive microsystem operates by EM backscattering at microwave frequencies (~ 2.25 – 4.9 GHz) wherein most of the irradiated EM signals experience a large amount of scattering and absorption

in the brain tissue medium. Hence, it is pertinent to measure the specific absorption rate (SAR) or localized power density of the EM fields absorbed by the biological media. SAR limits are regulated by the U.S. FCC for commercial mobile devices (1 g average SAR $\leq$ 1.6 W/kg) (Means & Chan, 2001). In other parts of the world, SAR is usually regulated by criteria set forth by the International Radiation Protection Association (IRPA) and International Non-Ionizing Radiation Committee (INIRC) to a less stringent threshold of SAR averaged over a 10 g tissue sample (SAR_{10g}) of less than 2 W/kg (International Commission on Non-Ionizing Radiation Protection, 1998). SAR thresholds are designated to account for known thermal consequences as related to specific SAR doses (Hossmann & Hermann, 2003). SAR may be empirically measured by thermographic procedures, of which the operation and accuracy have been extensively explored (Guy, 2000) (Okano, Ito, Ida, & Takahashi, 2000). SAR is a measure of the rate at which energy is absorbed by biological tissue and is defined as the power absorbed per mass of tissue. SAR is generally defined in reference to the electric field by,

$$SAR = \frac{\sigma E_i^{\,2}}{\rho} \tag{5.1}$$

where ρ (kg/m^3) is sample density and E_i (V/m) is root mean squared (RMS) electrical field strength, respectively. U.S. FCC authorizes measurement of the SAR as averaged within 1 g of tissue (SAR_{1g}), usually enclosed in the brain itself (Means & Chan, 2001) (Hossmann & Hermann, 2003). Because of the strong heterogeneity of the EM fields in tissue, along with the close orientation between source external interrogator and implant, SAR analysis must consider the effects of localized pulse energy absorption in the head. Therefore, in the present study, the external antenna, implanted microsystem, and head-

mimicking phantom are situated in an arrangement that would produce the highest magnitude third order backscattering products (P_{IM3} at $f_{IM3} = 2f_0 \pm f_m$), as well as elicit maximal SAR, the worst-case scenario, in the brain tissue (Schwerdt, Miranda, & Chae, Analysis of electromagnetic fields induced in operation of a wireless fully passive backscattering neurorecording microsystem in emulated human head tissue, 2013). The work presented in this chapter was implemented at the facilities of NASA Glenn Research Center (Antenna and Optical Systems Branch).

5.1. Methods

Computational and empirical measurements of SAR are carried out by FEA analysis in HFSS and thermographic imaging methods, respectively. The computational analysis give a detailed and accurate insight onto SAR comportment in the brain tissues, while the real measurements serve to validate these theoretical figures. The arrangement of the wireless recording system is fixed throughout analyses. Human head mimicking phantom geometry and properties are identical to those reported in the previous chapter (chapter 4.4).

FEA is performed via HFSS to compute SAR generated during operation of the microsystem. The implant-phantom assembly is placed parallel to the plane of the LTSA substrate with an air gap of 0.5 mm (Figure 5.1). SAR computations are segregated into the two wireless transmit and receive channels of propagating EM waves; primary downlink for transmission from the external antenna at f_0 to the microsystem, and secondary uplink for backscattering from the microsystem to the external antenna at f_{IM3}. The signal loss (including mixer conversion loss, path loss, antenna gains, etc.) between

supplied transmit carrier (P_0) from external antenna and backscattered harmonics (P_{IM3}) is > 90 dB (chapter 4.3 – 4.5). This significant loss suggests that the SAR contributions of the uplink mode caused by backscattering of the microsystem are negligibly small relative to the primary downlink channel or, in other words, the externally supplied radiation is the primary determining factor of SAR for the fully passive system. The local maximum SAR is computed for both modes to measure their isolated effects. Spatial SAR distribution across the transverse plane of human head tissue layers aligned with the implanted microsystem is measured to visualize SAR along the main wireless propagation path. SAR_{1g} is obtained by averaging SAR within a 1 g cube underlying the microsystem and facing the LTSA and incorporating both dura/gray and white matter layers ($\rho \approx 1{,}030$ kg/m^3). SAR_{1g} on the surface of the irradiated head is obtained by averaging SAR within distal skin and bone strata ($\rho \approx 1{,}100$ kg/m^3 for skin and $\approx 1{,}800$ kg/m^3 for bone). Average 1 mg SAR (SAR_{1mg}) is also obtained for various depths in the phantom. All simulations were performed with a set source power of $P_0 = 50$ mW, representing the highest amount of power employed in practical operation of the microsystem.

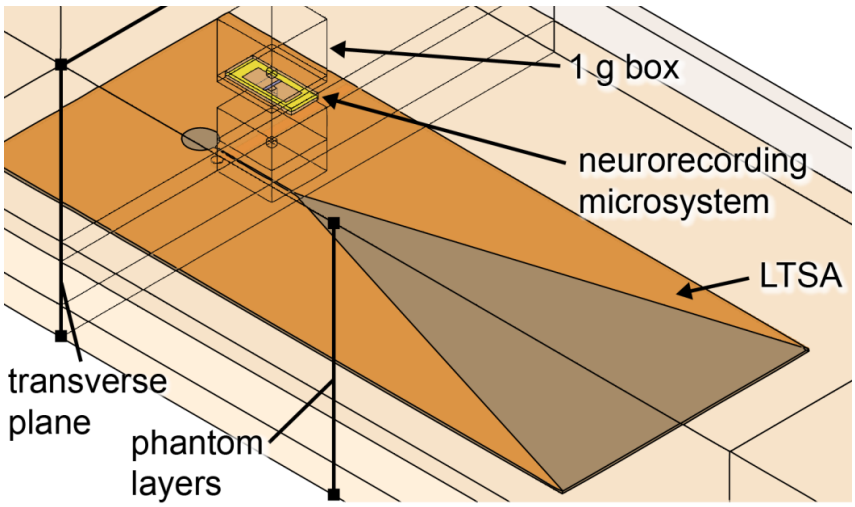

Figure 5.1. FEA simulation setup for computing SAR. Averaging 1 g and 1 mg boxes are seen along the orthogonal axis of the microsystem. The transverse cross section across which spatial SAR is computed is also indicated.

Thermographic measurements involve recording the temperature rise affiliated with the induced radiating wireless fields through the use of an IR camera (Guy, 2000) (Okano, Ito, Ida, & Takahashi, 2000) (Ito, Furuya, Okano, & Hamada, 2001), to empirically estimate SAR. The measured temperature rise may be directly related to SAR by,

$$SAR = C\frac{\partial T}{\partial t}\bigg|_{t\to 0} = C\frac{\Delta T}{\Delta t} \tag{5.2}$$

where C (J/(kg·K)) is specific heat of the sample and t (seconds) is duration of exposure to radiation. C is ~ 1,300 J/(kg·K) for bone and ~ 3,750 J/(kg·K) for brain phantoms (Okano, Ito, Ida, & Takahashi, 2000) (Ito, Furuya, Okano, & Hamada, 2001). Equation (5.2) is valid for small thermal diffusion and when ΔT is linearly proportional to Δt. Deviations caused by thermal diffusion may be minimized by increasing ΔT (increasing

P_0) and reducing lag time between procuring IR images and lowering of Δt. P_0 is fixed at 20 W throughout testing. ΔT was measured as a function of Δt to confirm near linear ΔT for $\Delta t \leq 60$ seconds, as shown in Figure 5.2. Throughout testing, neurorecording and backscattering functionality was confirmed at this higher operating power (note– maximum P_0 supplied by interrogator for normal operation is < 50 mW) by monitoring P_{IM3} signals on a spectrum analyzer. Unlike prior thermography-based SAR measurements (Okano, Ito, Ida, & Takahashi, 2000) that only used an external radiating device towards the human body, the present work incorporates a radiating implant. Phantom layers emulating the dielectric and thermal properties of individual human head tissue layers are constructed in the same manner as previously described (chapter 4.5). The dura mater and gray matter layers are merged for ease of experimental testing since the dura is very thin (< 0.5 mm) and should have little influence on radiating EM fields as may be corroborated by their similar dielectric properties (Gabriel & Gabriel, 1996). The phantom is sliced across the implant axis to image surface SAR distribution along the main radiating axis of the implant and across the various phantom layers, replicating computational FEA procedures. An IR camera (FLIR, SC620) possessing a resolution of 640 x 480, or equivalent ~0.09 x 0.12 mm^2 spatial resolution, is used for thermographic imaging. A thin layer of black paint is uniformly sprayed onto the phantom cross-sectional halves to normalize emissivity, ε_m, to ~ 0.95 across the various layers and reduce errors caused by apparent T_m ($T_m^4 = \varepsilon_m \cdot T_0^4 + (1-\varepsilon_m) \cdot T_{amb}^4$) measured by the IR camera. Plastic wrap is used to separate the phantom surface from the external antenna below and create an effective separation of ~ 0.3 – 0.5 mm that nearly replicates the air gap used in computational analysis. The procedure for measuring ΔT during wireless

operation involves: i) capturing an IR image of the surface of the microsystem enclosed phantom half to capture initial temperature, T_i, distribution, ii) merging the two phantom halves, turning on the function generator to supply V_m (50 mV_{pp}) to the implanted microsystem, and turning on the signal generator and microwave amplifier to supply P_0 (20 W) to the external antenna (LTSA), iii) maintaining wireless backscattering operation and confirming backscattering operation by concurrent monitoring of wirelessly retrieved P_{IM3} in spectrum analyzer, and iv) after selected Δt (45 to 60 seconds), detaching secondary phantom half and capturing an IR image of the radiation exposed primary phantom half surface to measure final temperature T_f and obtain targeted temperature rise ($\Delta T = T_f - T_i$). Convective cooling caused by phantom splitting in step (iv) is expected to be minimal (i.e., of the order of 0.1 ^oC) and within the IR camera's resolving range. The setup is shown in Figure 5.3. Thermal data from the IR camera are exported to MATLAB where measured ΔT over specified Δt are converted to correlated SAR based on Equation (5.2). The evaluated SAR data are re-normalized to a source power of P_0 = 50 mW, the maximum operating power used by the external interrogator to activate microsystem.

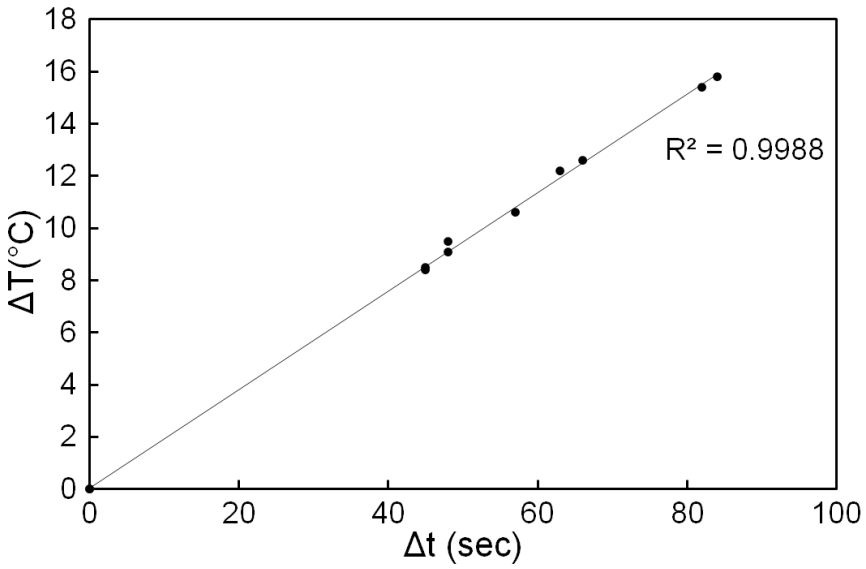

Figure 5.2. Temperature rise measured in phantom as a function of radiation exposure duration (at P_0 = 20 W) plotted with trend-line having coefficient of determination (R^2) of 0.9988, indicating a nearly linear relationship between ΔT and Δt, and validating SAR derivations based on Equation (5.2).

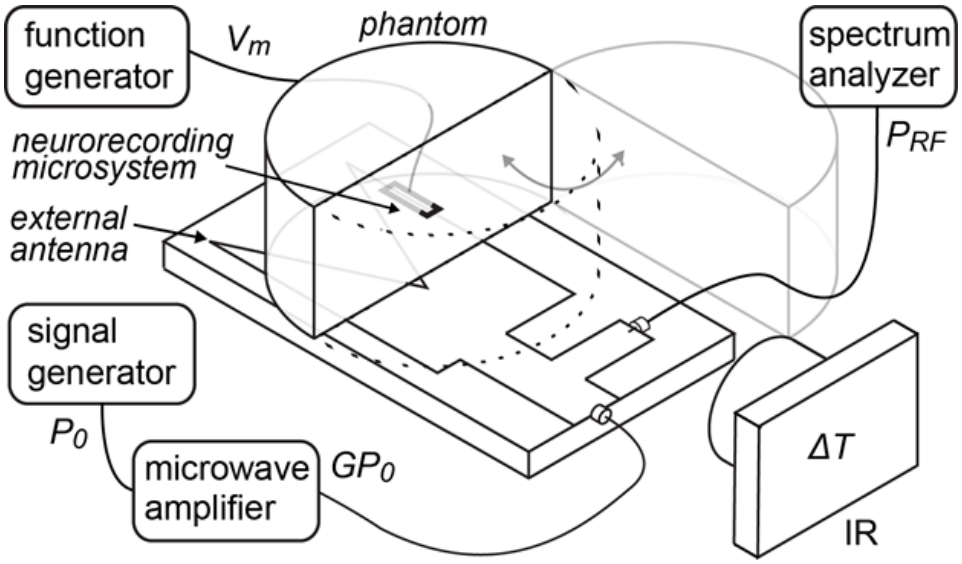

Figure 5.3. Setup for IR-based empirical measurement of SAR generated during operation of implanted microsystem inside human-head mimicking phantom. The

microsystem is embedded in the gray/dura striatum towards the exposed cross-sectional surface. The phantom cross-section is spray painted black to normalize apparent emissivity for IR measurements. The external LTSA antenna is separated from the phantom by thin plastic wrap (≤ 0.5 mm). The IR camera (lower right) records thermographic images for subsequent determination of SAR.

5.2. Results and discussion

SAR data were obtained for isolated primary downlink and secondary uplink modes of the wireless backscattering neurorecording operation. The simulation of the uplink backscattering channel is made by setting the conversion gain of the onboard nonlinear mixer to an idealized value of $G_{2\omega}$ = -5 dB, signifying the loss introduced by translation of incident f_0 carrier to third order harmonic output products at f_{IM3}. Concomitantly, for a computed optimal downlink wireless path loss of ~ 20 dB at f_0 factored in with the aforementioned $G_{2\omega}$, the power backscattered by the implanted microsystem antenna at f_{IM3} is set as 0.158 mW. The peak local SAR computed in the surrounding dura/gray mass of the microsystem is 4.648 W/kg (SAR_{1g} = 0.216 W/kg) for the primary downlink mode at f_0 = 2.45 GHz and 0.6 W/kg (SAR_{1g} = 0.0318 W/kg) for the downlink mode at f_{IM3} = 4.9 GHz. Spatial SAR distributions for the fundamental transmit mode and for secondary backscatter mode are shown in Figure 5.4(a), and (b), respectively.

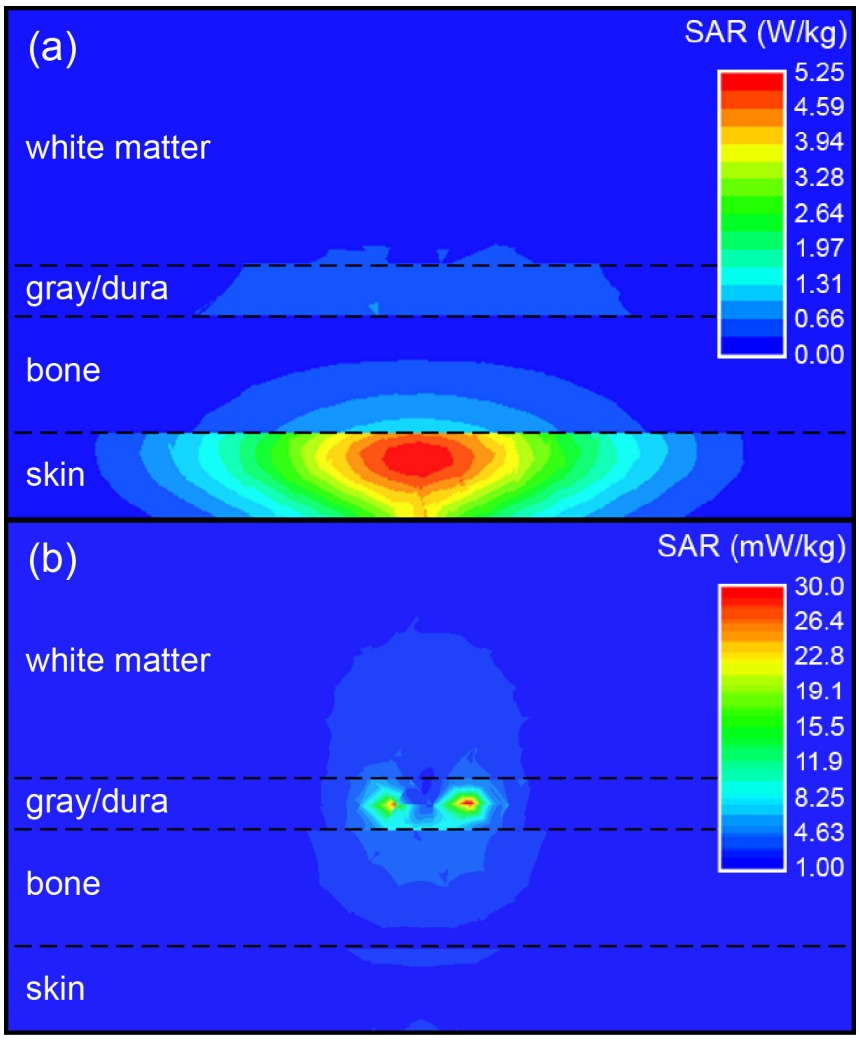

Figure 5.4. (a) Computed SAR distribution across cross section of phantom (50 mm x 40 mm) for primary transmit (uplink) mode at f_0 = 2.45 GHz for P_0 = 50 mW and (b) for secondary backscattering (downlink) mode at f_{IM3} = 4.9 GHz for a set backscatter power of 0.158 mW irradiated from the microsystem as derived by factoring computed (idealized) wireless propagation and mixer conversion loss (~25 dB).

The plotted local SAR distribution for operation of the microsystem in the constructed phantom is shown in Figure 5.5. In order to estimate average volumetric SAR values corresponding to the computed average SAR_{1g} and SAR_{1mg}, the measured surface

SAR distribution is approximated to have an equal distribution along its orthogonal plane. This coarse interpretation is expected to indicate the maximum possible average SAR as the assimilated SAR fields rapidly decay away from the axis of the microsystem, where thermal measurements are taken. As follows, the areal SAR distribution (1 mm^2 and 1 cm^2) is evaluated along with average volumetric SAR (~ 1 mm^3 and 1 cm^3). Based on these reconstructions, the maximum SAR_{1g} is ~ 0.45 ± 0.11 W/kg, which is higher than the computed value (0.216 W/kg and 0.102 W/kg for primary and secondary modes, respectively). The results are higher than the computed values since the evaluation of volumetric SAR based on areal SAR, represents the state where the entire volume possesses the same SAR everywhere inside that is equal to that displayed at the planar cross-section, which is not likely the actual situation. In actuality, SAR varies in the volume and, based on the computational model, decays away from the microsystem. Here, areal SAR is measured at the cross-section intersecting the microsystem, where SAR is most likely maximum. Hence, the evaluated volumetric SAR measurement is higher than the computed value, and, most likely, higher than the actual volumetric SAR. SAR_{1mg} is plotted relative to depth into the tissue mass alongside theory, as shown in Figure 5.6. SAR_{1mg} computed for two different vertical axes along the microsystem are included in the plot to account for SAR variability. The computed and experimental SAR data are tabulated in Table 5.1.

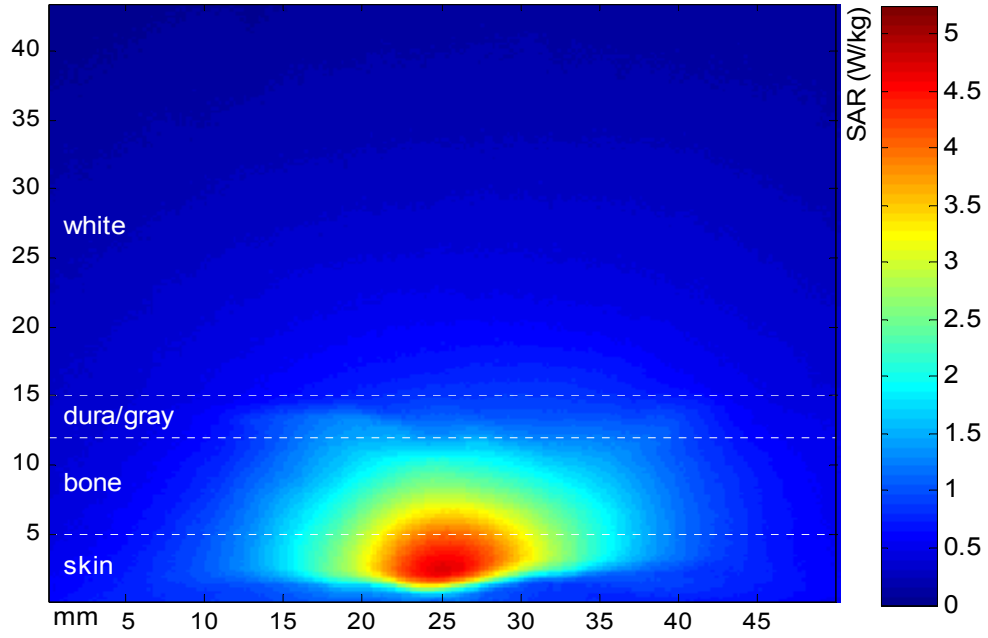

Figure 5.5. Measured spatial SAR distribution. Implanted microsystem (not visible) is embedded in dura/gray layer. SAR distribution is seen to concentrate towards the external skin layers of the phantom and decay rapidly towards more critical brain tissue mass, as expected.

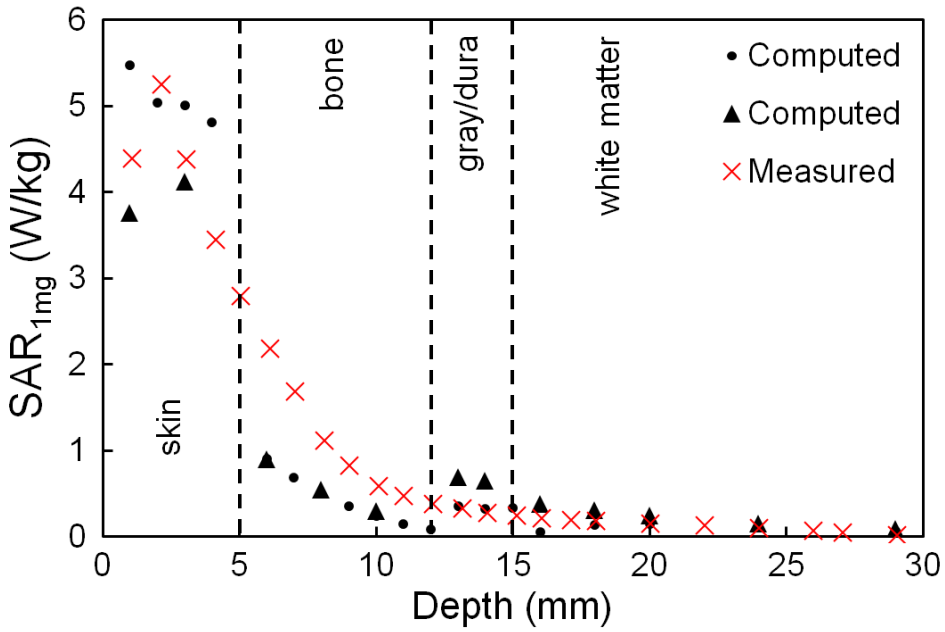

Figure 5.6. Computed and measured maximum average SAR_{1mg} versus penetration depth of tissue volume. Computed SAR_{1mg} for two different vertical axes aligned with implanted microsystem are incorporated.

Table 5.1. Summary of SAR measurements.

		Computed		**Measured**
		Primary (W/kg)	*Secondary (mW/kg)*	*(W/kg)*
Max Avg. SAR				
brain	*1 g*	0.216	31.8	0.45 ± 0.11
	1 mg	0.714	154	0.69 ± 0.17
dura/gray	*1 mg*	0.302	469	1.16 ± 0.23
bone	*1 mg*	1.109	81.7	1.93 ± 0.53
skin	*1 g*	2.432	3.97	2.40 ± 0.81
	1 mg	7.364	4.39	4.43 ± 1.09
Max Local SAR				
white matter		0.620	204	0.68 ± 0.32

dura/gray	4.648	600	1.67 ± 0.69
bone	1.277	114	4.85 ± 1.30
skin	10.06	5.49	8.49 ± 2.23

The computed and measured SAR_{1g} associated with operation of the fully passive wireless neurorecording microsystem (0.216 W/kg computed and 0.45 ± 0.11 W/kg measured at P_0 = 50 mW) in the human head equivalent phantom complies with formal U.S. FCC standards and informal clinical guidelines (Means & Chan, 2001) (Hossmann & Hermann, 2003) and is also much lower in comparison to available applicable studies of SAR for implantable systems operating at or near microwave frequencies (Merli, Bolomey, Zurcher, Corradini, Meurville, & Skriveryik, 2011) (Huang, Lee, Chang, Chen, Yo, & Luo, 2011). Unlike EM propagating wireless systems, inductive coupling schemes that are more commonly adopted by implant systems, primarily generate magnetic flux, whereby induced and absorbed wireless power is negligibly small. As such, it is inconsequential to compare SAR measurements of the current work to those of inductive coupling. On the other hand, existing work employing EM transmission systems, suggest significantly higher SAR_{1g} of 14.5 and 19.1 W/kg (289 and 382 W/kg at P_0 = 1 W) at lower microwave frequencies (0.9 – 2.45 GHz) when their reported values are adjusted for an equivalent power of P_0 = 50 mW (Huang, Lee, Chang, Chen, Yo, & Luo, 2011) (Merli, Bolomey, Zurcher, Corradini, Meurville, & Skriveryik, 2011). However, the higher SAR_{1g} is largely owing to the fact that these studies reference to power supplied by the implant itself, while the fully passive microsystem is exclusively activated by the external interrogator. In order to conform to FCC regulated $SAR_{1g} \leq 1.6$ W/kg, the existing studies limit input implant power to ≤ 1 – 4.2 mW. Regardless of these

restrictions, the potentially higher SAR associated with the induced EM fields generated by an external interrogator to activate implant functionality remains nonetheless unaccounted for.

The higher SAR measured within the bone layer (Table 5.1) may be caused by a combination of thermal diffusion, moisture loss across the phantom surface throughout the course of testing, diffusion of moisture from neighboring skin and dura/gray layers increasing thermal conductivity at the interface, and unadjusted specific heat capacity, C, for the bone mass. C is fixed at 3,750 J/(kg·K) for all experimental SAR estimations (as taken from reported thermal properties of skin, gray matter, and white matter phantoms) despite the considerably different $C \approx 1{,}300$ J/(kg·K) for bone medium (Guy, 2000) (Gabriel & Gabriel, 1996). Due to this combination of uncertainties, the apparent discontinuity observed in computed SAR (Figure 5.4) between skin and bone strata does not manifest itself in the measured SAR distribution (Figure 5.5). Moreover, the higher empirical SAR_{1mg} and peak local SAR values observed at deeper strata of the phantom are not seen in measurement by the thermographic imager and is likely caused by finite thermal diffusion of the higher SAR established in the skin layer. Such discrepancies may be subdued by using a higher output power and lower Δt.

As the microsystem may involve operation in the reactive near field regime, variations in individual phantom layer thicknesses would alter SAR considerably (Vidal & Lopez, 2010). As the propagation distance reaches the order of the wavelength, interference phenomena of the impinging EM fields become increasingly prominent. Nevertheless, this safety analysis targets a worst-case interpretation of SAR distribution in the ultimately intended subcranial implant setting and does not account for the highly

variable thicknesses that may be more influential for application in other parts of the human body

Results for the highest possible SAR generated in operation of the fully passive wireless neurorecording microsystem demonstrate compliance with current safety thresholds (Hossmann & Hermann, 2003) (Means & Chan, 2001) and significantly reduced SAR in the vicinity of more important underlying brain tissue layers in comparison to existing SAR studies (Huang, Lee, Chang, Chen, Yo, & Luo, 2011) (Merli, Bolomey, Zurcher, Corradini, Meurville, & Skriveryik, 2011). Furthermore, as may be visualized in Figures 5.4 – 5.6, SAR is primarily dominated by the radiating source (external interrogator) rather than the implanted backscattering microsystem. In consequence, induced EM fields are concentrated towards the skin surface, and rapidly decay towards more critical brain tissue mass. This externalization of SAR may contrast with inductively coupled or other wireless schemes containing active on-chip electronics, where emanated heat may be localized towards the implant surrounding due to internal powering elements (Kim, Tathireddy, Normann, & Solzbacher, 2007).

CHAPTER 6

MULTICHANNEL CONFIGURATION

One major practical obstacle of the current fully passive system is its limitation to a single channel; the current microsystem, as implanted, would only be able to record potentials from a single cerebral site. A single channel implant is envisioned to find use in few applications: localized seizure detection when non-invasive EEG is inadequate and/or arrayed implementation as a grid of subdural electrodes in the form of wireless ECoG. Nevertheless, the addition of multiple channels capable of recording from a spatially diverse population of neurons would significantly enhance the fully passive system's practicality and clinical and scientific viability. Multichannel platforms provide the ability to acquire detailed information of increasingly complex neural mechanisms for greater accuracy in the large-scale interpretation. As stated in Chapter 1, MEAs are the mechanical brain wiring module that are usually connected to the subcutaneous electronic recording platform through intracranial wires. MEAs are capable of probing small clusters of neurons spanning intervals of 10s to 100s of microns in the cortex. The monolithic incorporation of the fully passive recording microsystem with an MEA would provide the high resolution and density seen in current state of art neural recorders while maintaining the desirable safety benefits of minimal heat dissipation, simplicity (i.e. elimination of complex active circuitry), and single microsized recording implant (separate electronics and electrode modules connected by tethering through the skull are not needed). Manifestation of this added multichannel feature onto the fully passive device would espouse its inception towards real medical and scientific applications.

6.1. Methods and operation

Multichannel functionality is appended onto the existing passive recording operations of the single channel neurorecorder by introducing light-activated switch elements onto implant circuit. In doing so, the physical size of the implant, as determined by the integrated antenna, is maintained. Furthermore, recording and wireless backscattering operations by means of the same nonlinear mixing operations are also sustained. As a result, because the introduced switching operations (activated also by external interrogation) are passive, the desired passive qualities of the implant circuit are maintained. In order to activate recording from multiple channels through on-chip light-dependent switches, the external interrogator will carry the additional task of radiating light waves in addition to the original RF carrier or LO signal to activate main implant mixing and recording operations. This multimodal (EM light waves at near infrared, IR, wavelengths and EM waves at RF frequencies) approach to provide multichannel functionality is depicted in Figure 6.1.

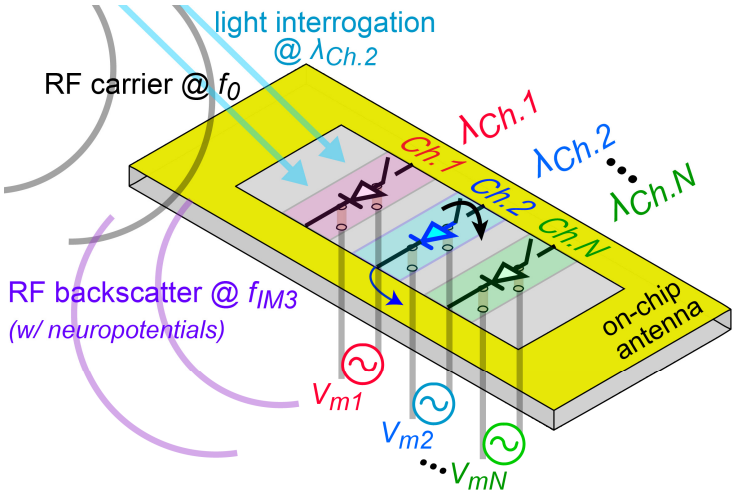

Figure 6.1. Conceptual illustration of light-activated multichannel recording; externally interrogated at specific wavelength of light (e.g., $\lambda_{Ch.2}$) activates corresponding light-sensitive switch (i.e., switch of channel 2) while other switches remain off. The non-linear element (diode varistor) mixes a neuropotential signal associated with the channel (V_{m2}) and the on-chip antenna backscatters f_{IM3} to the external interrogator. As we sweep the wavelength of the interrogated light, multichannel acquisition of neuropotentials at multisites can be obtained. This light-activated scheme allows the use of single antenna to maintain the overall footprint of neural implant as well as maintaining wireless and passive operation of the recorder.

The multichannel recorder is composed of a single wireless link (antenna) that backscatters targeted neuropotentials, and N recording channels, each possessing an optical wavelength selective switch (WSS), a mixer diode that "records" neuropotentials, and electrodes that interface the neuropotential inputs. Since the ability of the diode to mix and generate IM3 products, in essence, defines the "recording" operation of the fully passive circuit, "mixing" and "recording" terminology have the same connotation for the

remainder of this chapter. The antenna element may be maintained on the implant along with its wireless dual band functionality in receiving the LO signal (P_0) from the external interrogator and allowing the "on" recording channel to provide its mixed output harmonics ($2f_0 \pm f_m$) to backscatter these IM3 products to the external interrogator, in the same manner as the fully passive circuit. The N recording channels are connected to the antenna through an isolation capacitor (C_S) that provides DC and V_{mn} isolation between channels, while conducting the RF signals to the antenna. Each recording channel comprises a WSS in the form of a photoconductive diode switch with a unique responsive band for each channel so that it only responds and turns on by external irradiation of a specific wavelength of light. Each channel upholds the same mixer diode, uniform for all channels, and functions in virtually the same manner as the single channel version. The operational difference lies in its activation recording operations by the switch. As light is used to switch on selected channels and thereby allow multichannel functionality, the light-activated WSS thereby determines the on/off behavior of the diode mixing and recording operation. Unlike the single channel diode mixer that employed (in intended design) varactor or capacitive mixing to generate IM3 harmonics, the recording operation here adopts varistor or resistive mixing operations to output IM3 signals. The varistor scheme is employed as its IM3 product generation can be directly manipulated by the switch; photocurrent generated by the WSS is supplied to the recording varistor diode and directly controls the magnitude of output IM3 harmonics for a given channel. The amount of photobias across the mixer diode will in turn determine the "on"/"off" ratio or its behavior as an ideal switch. A simple circuit schematic of the multichannel recording

system, less the antenna, is shown in Figure 6.2 and the individual light-activated WSS and diode recording elements are discussed in further detail below.

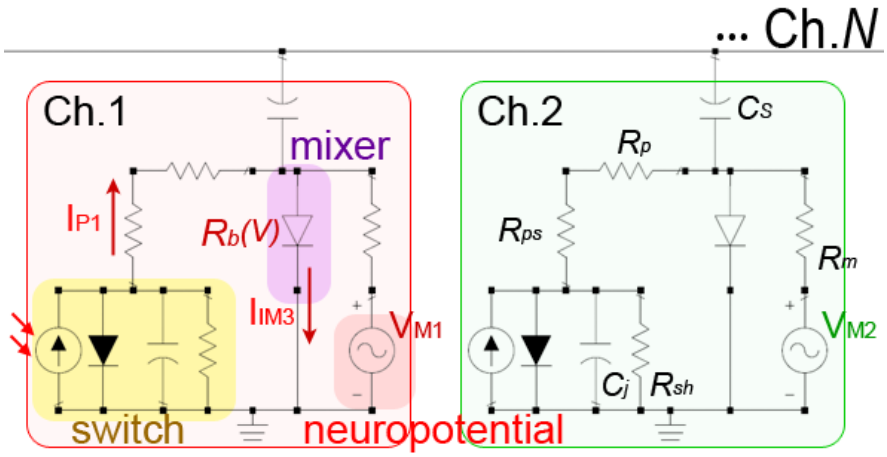

Figure 6.2. Simplified equivalent circuit model of multichannel recorder, including internal parasitics and isolation resistors/capacitors. Two units are shown and may be arrayed for N channels. Each channel is discriminated from each other depending on its responsive wavelength of light. The photodiode is represented as a current source (I_p) in parallel with a diode, junction capacitance (C_j) and shunt resistance (R_{sh}). Upon illumination, the activated switch provides photocurrent to the mixer diode of the same channel to shift the operating point of $R_b(V)$, the nonlinear barrier resistance of the mixer diode, which mixes supplied carrier (P_0) with neuropotential signals (V_{m1}, V_{m2},...V_{mN}).

6.1.1. Optical wavelength selective switch (WSS)

The WSS adopted here is a switch that is normally open (off) and turns on in response to a specific wavelength of light. In essence, the WSS is a photodiode, and its behavior as a switch connotes to its generation of a high or open circuit impedance when

"off" or "open" and its generation of photocurrent in proportion to the amount of incident light for a selected wavelength when "on" or "closed". A photodiode is simply a P-N or P-I-N junction semiconductor diode that generates electron-hole pairs in its in P and N layers, creating carriers and as a result, current flow, in proportion to the amount of light or photons. The photodiode's responsivity (A/W) or amount of current it generates in response to optical irradiance is determined by the thicknesses of substrate or doping layer, doping concentration, and/or material. The ability for the photodiode to perform switching function and turn "on" or "off" in response to light is determined by its responsivity and ability to generate photocurrent, which will be used to activate channel recording functions, as will be discussed in the next section. On the other hand, the ability for the photodiode switch to selectively respond to a specific center wavelength with a sufficiently narrow bandwidth and out of band rejection will determine channel to channel isolation and maximum number of channels. For system-on-chip forms, channel selectivity or wavelength selectivity is addressed either through the fabrication process of the photodiodes themselves and/or incorporation of optical filters. Arrays of photodiodes with linearly varying wavelength response and bandwidths near 4 nm have been fabricated by varying the thickness of the anodic oxide layer onto the photodiodes (Hu, Ko, & Coldren, 1997). These arrays had a 14.5 dB rejection ratio (amount of out of band reflection) 4 nm from specific resonant peaks. Other integrated channel selective photodiodes have been attempted for miniature spectrometry applications by depositing $Al/SiO_2/Ag$ layers that act as Fabry-Perot optical filters onto the p-n junction photodiodes (Correia, Bartek, & Wolffenbuttel, 2000). Channel filtering here is provided by

absorptive color filters rather than monolithically photodiode integrated filters for ease of initial conception.

The light-induced DC photocurrent generated by the WSS enables the recording operation of the same channel's diode recorder, and resulting functionality as a switch. The current through the photodiode may be simply expressed as, $I_o = I_P - I_D = I_P - I_S(e^{\alpha V} - 1)$, where I_P (photocurrent) is proportional to the supplied optical power irradiated and is produced in the reverse direction of the diode current (I_D). The equivalent circuit representation of the photodiode is seen in Figure 6.2. When the photodiode is open-circuited (I_o = 0), open-circuit voltage of the photodiode is expressed as,

$$V_{op} = \frac{1}{\alpha}\ln\left(\frac{I_p - I'}{I_D} + 1\right) \tag{6.1}$$

where $\alpha = qV/(nkT)$ (V is voltage applied, q is the magnitude of charge of an electron ≈ $1.602\,176\,565\times10^{-19}$ C, k is the Boltzmann constant ≈ 1.3806488×10^{-23} J/K, T is the absolute temperature (K)), and I' is the current through its shunt resistance (R_{sh}). When short-circuited (V_o = 0), its current is expressed as:

$$I_{sh} = I_p - I_D\left(e^{\alpha I_{sh}R_s} - 1\right) - \frac{I_{sh}R_s}{R_{sh}} \tag{6.2}$$

where R_S is the series resistance. The desired mode of operation for the photodiode for the multichannel neurorecorder application is in the "photoconductive" regime, near zero or small negative voltage bias. The photoconductive mode provides maximum reverse photocurrent to the load (mixer recording diode). Increasing I_P will generate a voltage across its internal diode, effectively reducing its internal resistance, and as a result

reducing the DC bias (V_B) to be supplied to the mixer diode. Resistors are added in series to maximize V_B across the recording diode. Conversely, these resistors also dissipate current supplied to the recording diode. The amount of resistance must be carefully chosen and also depends on the barrier potential of the photodiode and mixer diode; the former should be greater than that of the mixer diode to ensure that most of the I_P is supplied to the mixer diode. Furthermore, an RF choke inductor is added in series to minimize RF current into the photodiode from the antenna. As seen in Figure 6.3., commercially available photodiodes are capable of generating microampere levels of photocurrent in response to 1 – 100 mW/cm^2 of light irradiation; the responsivity curves suggest that the photodiodes will be suitable for activating channel recording operations given a reasonable amount of light (natural sunlight at earth's horizon can range to ~ 100 mW/cm^2) .

6.1.2. Channel mixer and recording

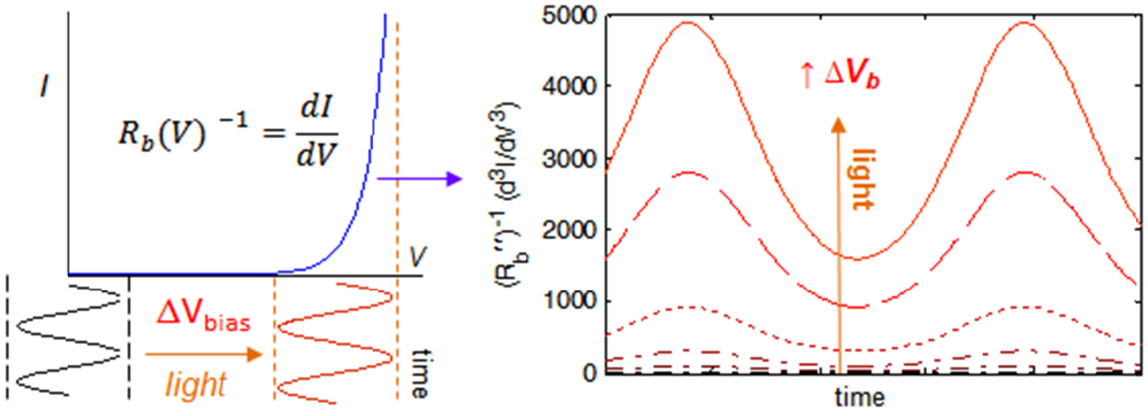

Figure 6.3. Illustration of photo-bias enabled resistive varistor mixing scheme. The left plot shows the typical I-V characteristics of a diode and how a shift in DC bias towards V_t allows low level time varying waveform inputs to encounter a nonlinear resistance near V_t whose differential varies depending on bias level. The right plots show the plotted variation of $R_b(V)^{-1}$ (d^3I/dV^3) as a function of time for the sine wave input for increasing bias level, V_b ($V_b \propto light$) (model uses V_{in} = 10 mV_{pp} and $0 \leq V_b \leq 27$ mV). The intention is that for harmonic mixing and therefore neurorecording operations to transpire, a switch must be activated to provide a photo-bias that shifts the DC operating point. Mixing is only enabled when P_0 or corresponding V_0 varying across the diode is sufficiently low to not rectify or exceed diode V_t in the absence of DC bias.

In contrast to the single channel implementation that utilizes a diode in its varactor mode of operation to mix V_m and externally supplied P_0 via mixing through its voltage-variable nonlinear capacitance ($C_j(V)$), the mixer for multichannel implementation utilizes the varistor mode of operation for the same diode to generate

mixing products through its voltage-variable nonlinear forward conductance or, inversely, barrier resistance ($R_b(V)$). The varistor mode of mixing is preferred to integrate switching by means of the light-activated photodiode switches. In the "off" state, when the photoconductive switches do not supply any DC photocurrent bias, the IM3 output of the mixing varistor diode of supplied carrier (P_0) and input neuropotentials (V_m) is low. In the "on" state, when the photoconductive switches supply a DC bias, the IM3 output is high. As nearly any diode is capable of mixing with or without formally supplied DC bias or with the bias provided by input RF signals, not much can be done to explicitly deactivate its mixing operation and only "low" and "high" magnitude IM3 products can be targeted. The general expression for diode current is as follows,

$$I = I_R + I_C = I_s\left(e^{\alpha V} - 1\right) + \frac{dC_j(V)V}{dt} \tag{6.3}$$

where I_R represents the diode current through its variable resistance (forward conductance), and I_C represents the current through its junction capacitance ($C_j(V)$), and each term is expanded on the right side. I_R is ideally zero when the voltage is less than the contact or barrier potential (V_t) and exhibits an exponential rise when $V > V_t$. I_C does not contribute in the forward operating mode, but dominates for reverse bias ($V < V_t$) and generates nonlinear output harmonics through its voltage variable $C_j(V)$ (varactor mode). The single channel recorder was intended to employ this latter varactor mixing scheme provided that the local oscillator (LO) drive for the carrier (f_0) is not strong enough to drive the diode beyond V_t, towards forward conduction and resistive mixing (in reality, both varactor and varistor modes were probably engaged in generating IM3 products). Therefore, in the varactor mixing scheme, a diode (usually presented as a hyperabrupt

varactor diode) with a high $0.9 < \gamma < 1.1$ to enhance nonlinear operations and a fairly high $V_t \sim 1.3$ V to suppress resistive components, was selected. Conversely, for the multichannel implementation here, a diode (usually presented as a barrier or junction diode) possessing $\gamma \leq 0.33$ (to suppress inherent varactor nonlinearity) and a sufficiently low V_t (to operate at low LO drives) is used to repress nonlinear mixing in the absence of a DC bias (off state) while producing higher IM3 mixing products in the presence of a small DC bias (on state) through its nonlinear barrier resistance ($R_B(V)$). This incremental DC bias is provided by the photocurrent generated by the photodiode in response to external illumination of light. By shifting the DC operating point of the varistor diode towards where d^2I_R/dV^2 or d^3I_R/dV^3 becomes maximal, the time varying input waveforms ($V = V_0\cos(\omega_0 t) + V_m\cos(\omega_m t)$) will encounter a higher variability of the voltage-dependent resistance to produce larger nonlinear mixing products with a magnitude proportional to the d^2I_R/dV^2 (ie. $R_b'(V_b)^{-1}$) (for IM2 products—2nd order harmonics) or d^3I_R/dV^3 (ie. $R_b''(V_b)^{-1}$) (for IM3 products) slope at this operating point. This may be visualized by expanding on the term I_R in the equation above using a Taylor Series expansion around an operating point of $V = V_b$, the supplied photocurrent generated DC bias, such that,

$$I = I(V_b) + \frac{I'(V_b)}{1!}(V - V_b) + \frac{I''(V_b)}{2!}(V - V_b)^2 + \frac{I'''(V_b)}{3!}(V - V_b)^3 + \ldots$$

$$I = a_0 + a_1 v + a_2 v^2 + a_3 v^3 + \ldots \tag{6.4}$$

The a_n terms represent the magnitude of the n-th harmonics and may be expressed as, $a_2 = \frac{I_s \alpha^2 e^{\alpha V_b}}{2}$, and $a_3 = \frac{I_s \alpha^3 e^{\alpha V_b}}{6}$, showing that the applied V_b DC bias will

exponentially increase the a_n coefficients and the correlated IM2 (a_2) and IM3 (a_3) harmonic products. V^2 may be expanded and the $f_0 \pm f_m$ (IM2) V^2 and a_2 terms substituted into I (above), to find the following expression, $I_{IM2}\big|_{\omega_0 t \pm \omega_m t} = \frac{I_s \alpha^2 e^{\alpha V_b}}{2} V_0 V_m \cos(\omega_0 t \pm \omega_m t)$. Similarly, the V^3 term may be expanded and the targeted $2f_0 \pm f_m$ (IM3) products substituted to find,

$$I_{IM3}\big|_{2\omega_0 t \pm \omega_m t} = \frac{I_s \alpha^3 e^{\alpha V_b}}{8} V_0{}^2 V_m \cos(2\omega_0 t \pm \omega_m t) \tag{6.5}$$

The equations indicate that the magnitude of P_{IM3} is determined by the diode's forward conductance nonlinearity (ie. $P_{IM3} \propto (a_3)^2 \propto (d^3 I_R/dV^3)^2$) as well as the product of the input signals (ie. $P_{IM3} \propto (V_0{}^2 V_m)^2$). The equations may incorrectly suggest that increase in V_b will indefinitely increase the output harmonics. However, P_{IM3} output depends on a large number of variables related to the frequency and voltage dependent circuit parasitics, and embedding impedances. For the diode alone, the power of the output harmonics depends on the operating load of the R_b (the barrier resistance saturates or becomes short circuited at some point) of the diode as well as its internal barrier capacitance (C_b) and spreading resistance (R_s). Operation will require tuning diode bias (via externally supplied photo-bias and/or P_0) for maximum P_{IM3} generation; C_b will suppress P_{IM3} at lower bias when the barrier capacitance dominates and R_s and R_b will limit P_{IM3} at higher bias as the fixed spreading resistance reduces the influence of the variable $R_B(V)$ and the nonlinear barrier resistance saturates. Optimal R_b may be found by first determining the broadband conversion loss (L_c) due to power dissipation in the diode. This is found by taking the ratio of power available at the diode ($P_a \propto P_0$ supplied) to the power supplied to the barrier resistance of the diode (P_b):

$$L_c = \frac{P_a}{P_b} = 1 + \omega^2 C_b{}^2 R_b R_s + R_s / R_b \tag{6.6}$$

By taking $dL_c/dR_b = 0$, it is found that the optimal barrier resistance is,

$$R_b = 1/\omega C_b \tag{6.7}$$

to minimize loss and increase the power of the output harmonics. Therefore, optimal mixing performance and highest IM3 products are generated when the light supplied (V_b) and externally radiated P_0 align R_b accordingly. Along with externally supplied P_0 to adjust the operating level of the diode, mixing performance also depends on diode specifications such as its V_t and C_b. V_t should be chosen to be as small as possible to reduce required illumination and resulting photocurrent needed to deliver optimal V_b. Similarly, C_b should be as small as possible as it will introduce loss at higher frequencies as may be seen in the equation above. As indicated in Equation (6.6) and suggested earlier, the diode also exhibits a series spreading resistance, R_s, that limits the nonlinear R_b above V_t and reduce harmonic outputs. L_c is plotted in Figure 6.4 as a function of R_b to visualize and determine optimal diode specifications. Based on the requirements for low V_t, C_b, γ, and R_s, initial diodes selected included MA/COM DMK2790 (γ = 0.26, V_t = 0.82 V, C_b = 0.05 pF, R_s = 4 Ω), MA/COM CDB7620 (γ = 0.32, V_t = 0.5 V, C_b = 0.15 pF, R_s = 4 Ω), and SMS7621 (Skyworks), but a variety of diodes were simulated to optimize diode selection. However, these simple circuit models do not take into account the embedding impedances (antenna, isolation capacitor, photodiode switch circuit, and electrode impedances) that will affect the maximum magnitude of desired IM3 harmonics that will be backscattered through the antenna. The majority of design falls on harmonic balance

circuit simulation to optimize mixing performance and multichannel functionality, as will be discussed in the subsequent section.

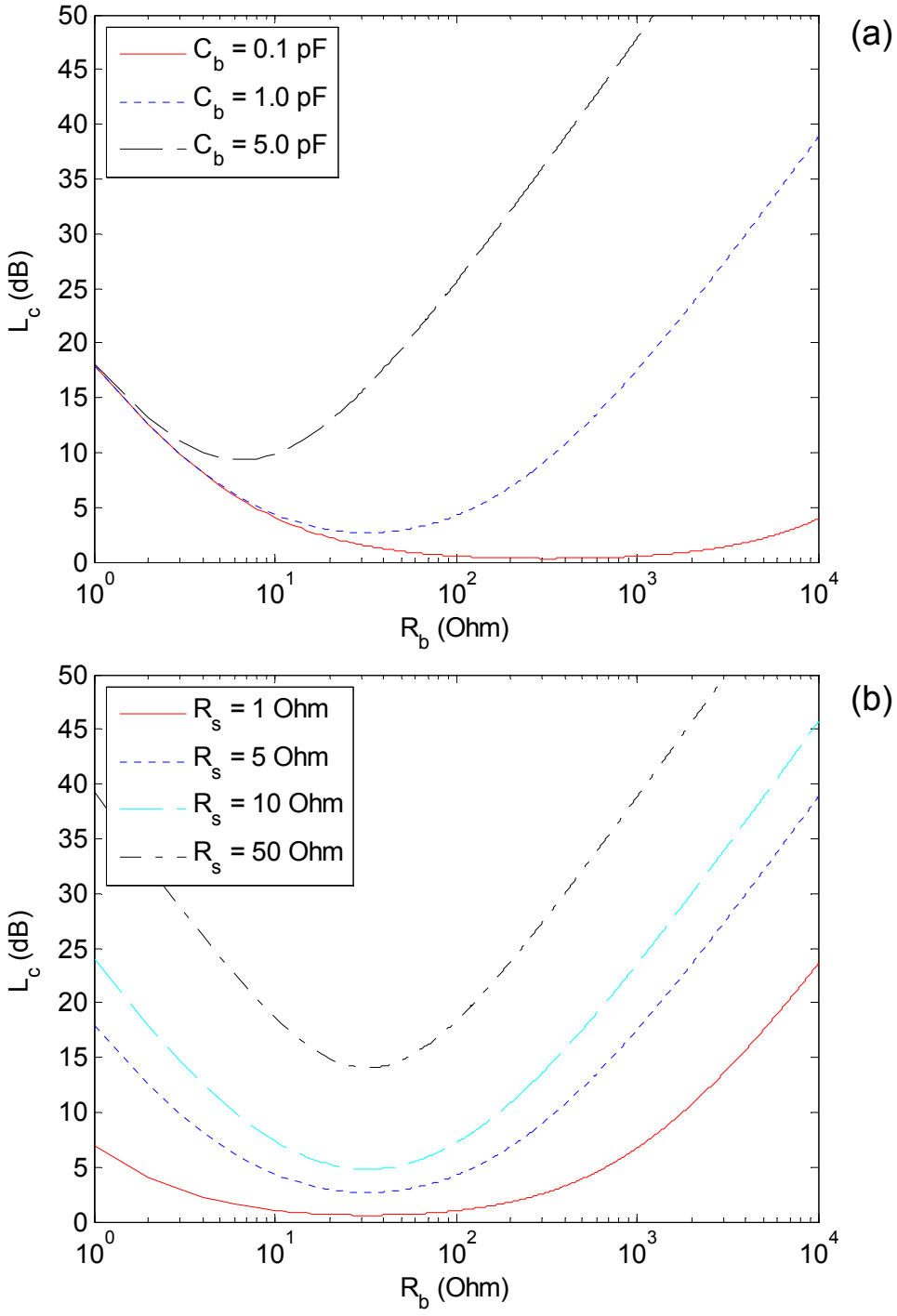

Figure 6.4. (a) Broadband conversion loss, L_c, of varistor diode mixer for three different barrier capacitance values of C_b = 0.1 pF, 1 pF, and 5 pF (a typical range of capacitance values for RF mixer diodes), as a function of barrier resistance, $R_b \propto$ externally supplied P_0 or photocurrent supplied by irradiation of light upon photodiode switch. R_s is set to 5 Ohm and frequency to 4.9 GHz. (b) L_c for four different spreading resistance values of R_s = 1 Ohm, 5 Ohm, 10 Ohm, and 50 Ohm (common range for low loss diodes), as a function of R_b. C_b is set to 5 Ohm and frequency to 4.9 GHz.

6.2. Wired proof of concept

To test feasibility of the multichannel switching operations (ie. test the ability of the wireless light modality to enable multiple channel recording operation), a proof of concept was coarsely assembled using commercial off the shelf (COTS) components. The aim was to test switching capabilities of the wireless light modality independent of wireless RF backscattering operations. Therefore the exciter LO and backscattering RF link was wired. The number of recording channels was limited to three for reasons of financial practicality (customized narrowband optical filters needed for increasing channel count are expensive).

6.2.1. Design

The proof of concept was constructed on printed circuit board (PCB) to verify the ability to record from multiple channels using light to turn on individual channels with distinctive responsive wavelengths. Channels 1, 2, and 3 were chosen to respond to dominant wavelengths of 650, 530, and 430 nm, respectively, corresponding to the

visible spectrum of light or red, green, and blue, respectively. The circuit used readily available surface mount broadband silicon photodiodes (PD93-21C for channels 1 and 2, and PD15-22C—blue enhanced photodiodes for channel 3) that served as the light activated optical switch elements. The photodiodes were arrayed (~10 per channel) to provide ~ I_p of 10s μA per channel when activated, as projected per specification sheet guidelines, in order to boost the responsivity (A/W) of each channel, thereby increasing the magnitude of photocurrent generated in response to irradiated light (mW), and finally the bias-enabled switching of the diode mixer for the same channel. For channel to channel isolation—isolating the optical bandwidth of each photodiode from each other to serve as functionally different channels—absorptive color filters (Kodak Wratten) 29 (red), 58 (green), and 47B (blue) were mounted on the photodiodes of channels 1, 2, and 3, respectively. The optical transmission spectra for the photodiodes and mounted channel filters are shown in Figure 6.5. The overlapping spectra of the nonideal filters will degrade channel to channel isolation, as will be seen in the results. Standard surface mount Schottky diodes (MMBD354LT1, ON Semiconductor) were used as the mixer diode with a V_t = 0.5 – 0.6 V, C_b = 1 pF, and γ = 1.0. No wireless link or antenna was integrated since the performance of external light activation on multichannel functionality was the targeted test parameter. Thus, the only external wireless interrogation performed was through the 3 high power LED light sources (XLamp XP-E and XT-E, Cree) with radiant flux of 100 – 200 mW each and with corresponding red, green, and blue optical bands to remotely activate mixing operation of individual channels. The constructed wired PCB recording circuit with wirelessly enabled optical switches and multichannel functionality is shown in Figure 6.6.

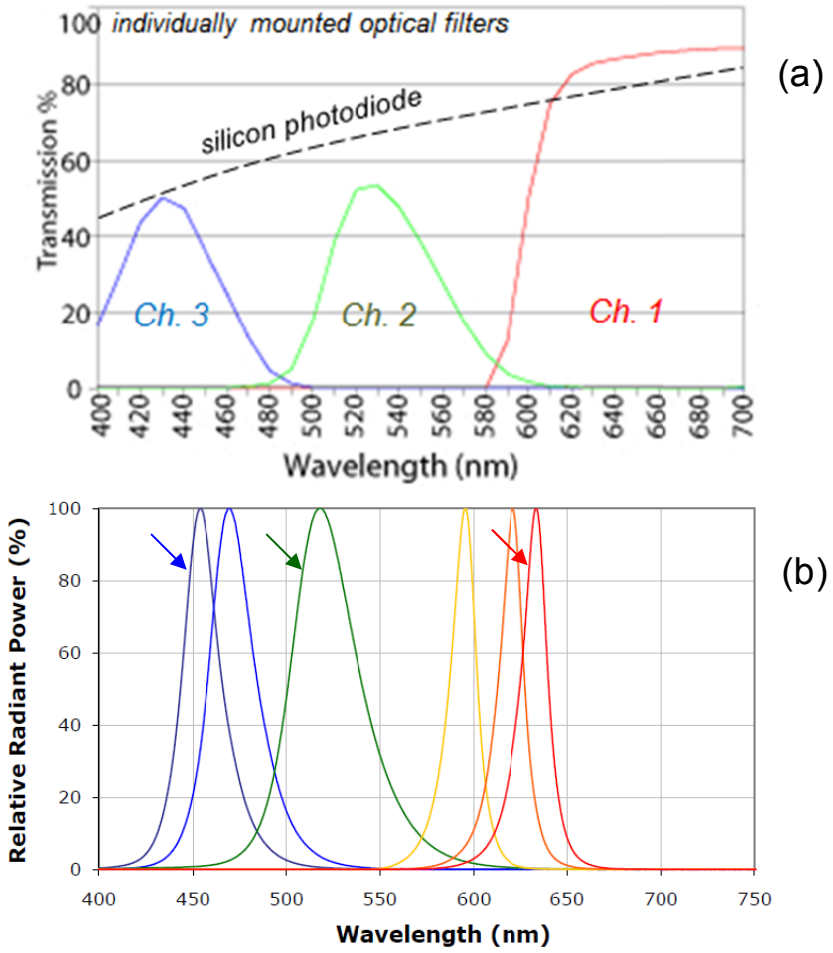

Figure 6.5. (a) Optical transmission spectra of the silicon photodiode (PD93-21C) (dashed curve) and individually mounted optical absorptive color filters for corresponding channels (Kodak Wratten 25, 58, and 47B). (Note-29 is not shown, but instead 25 is shown possessing similar spectrum except for a slightly higher lower cut off of 600 nm). (b) Optical transmission spectra of external LEDs (Cree XLamp XP-E or XT-E) for providing irradiative sources for the three individual channel bands to activate on-chip optical switches (bands of implemented LEDs indicated by arrow).

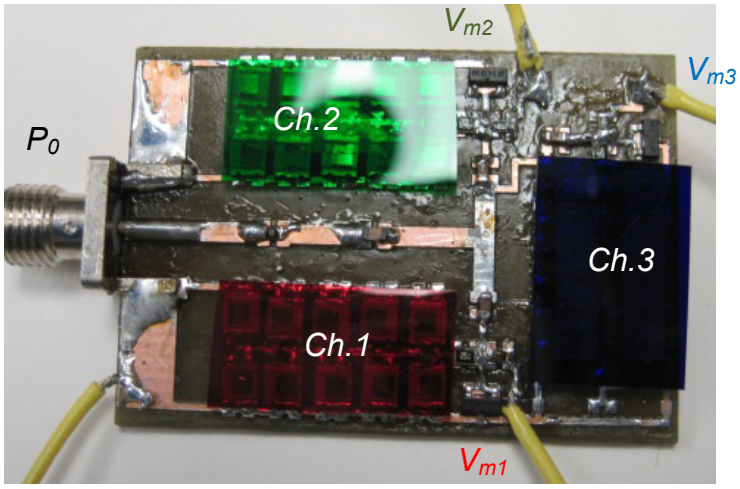

Figure 6.6. Proof of concept PCB prototype of 3 channel light activated neural recorder. Optical filters may be clearly seen and are placed above the photodiode array for each channel. External wires interface emulated neuropotentials (V_{m1}, V_{m2}, V_{m3}) and P_0 carrier is supplied through the SMA connector on the left.

6.2.2. Results

Testing was performed using a carrier f_0 = 10 MHz (a lower frequency was used to offset effects of parasitics and matching as well as nonideal γ and C_b of the current mixer diodes). P_0 of -7.4 dBm was found to be the optimal LO power to produce maximal channel to channel and on/off isolation as well as sufficient sensitivity (power of the output IM3 products). Increasing P_0 degraded isolation while decreasing P_0 degraded sensitivity, as expected. Each recording site or channel was made distinguishable by providing unique emulated neuropotentials (V_{m1}, V_{m2}, and V_{m3}) to each. The frequency of the neuropotential was varied for each channel (f_{m1} = 100 Hz, f_{m2} = 200 Hz, f_{m3} = 300 Hz). The magnitude of the emulated neuropotentials was maintainted across

all channels at V_m = 50 mV_{pp}. The signal to noise ratio (SNR) of the IM3 ($2f_0 \pm f_m$) output was measured through a spectrum analyzer with a 1 kHz span and resolution bandwidth of 1 Hz to produce an average noise floor of around -137 dBm. The measured results using optical activation of individual red, green, and blue channels are shown in Figure 6.7. It can be seen that the maximum SNR for each channel correlates to the matching wavelength of the supplied LED light source wavelength. Ideally, illumination of a single band of light should activate only a single channel. However, interference occurs and other channels may also be slightly activated due to out of band transmission of the color filters as well as out of band transmission of the LED light sources. However, enhanced optical band pass filters (ie. thin film interference filters) may be used in future implementations to achieve extensively higher out of band rejection (>50 dB) with narrower transmission bands. Lower V_m were tested, but the significant degradation of SNR for decreasing V_m (17 dB for V_m = 10 mV_{pp}, 5 dB at V_m = 1 mV_{pp}) was fairly impractical for testing channel to channel isolation and overall multichannel performance. However, SNR may be substantially improved by optimizing diode selection to possess lower V_t, C_b, and γ.

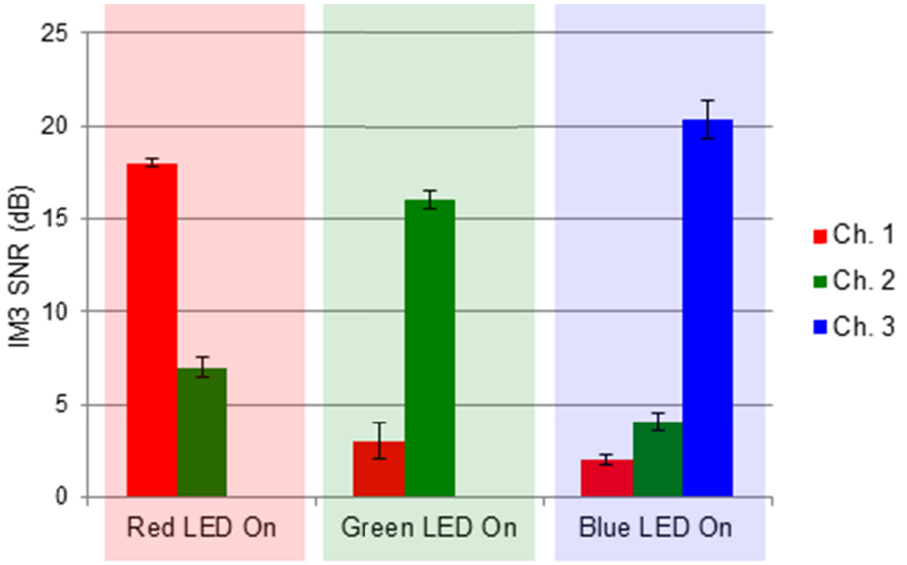

Figure 6.7. Measured performance of proof of concept multichannel neural recorder using light activated wavelength selective switches of 650 (red), 530 (green), and 430 (blue) nm (for red and green activation, channel 3 did not produce any observable signal above the noise floor).

The results demonstrate the ability for multichannel functionality through the passive varistor based harmonic mixing and wireless light activation of onboard photodiode switches. These results provided the assurance to forward development of an implantable wireless multimodal multichannel neurorecorder.

6.3. Wireless design and prototype

The immediate next step of the multichannel study was to integrate a wireless RF link (for transmitting neuropotential data wirelessly) along with the established wireless optical link (for switching/multichannel operation). The main goal of this study is to develop a 3–channel prototype operating wirelessly in air (preliminary attempt).

Demonstration of the wireless multichannel recorder in a biological tissue mimicking phantom of the implant medium will largely complicate the optical interrogation link where a large amount of scattering and absorption at the visible wavelengths (500–800 nm) is known to occur and ultimately degrade performance. As the purpose of this prototype is to confirm optically triggered multichannel recording operations in an entirely wireless fashion, wireless performance through human implant considerations is largely disregarded as this stage. Future work (chapter 7) will delineate requirements for wireless operation as a brain implant via use of near-infrared (NIR) optical interrogation bands. As NIR optics—photodiodes, filters, and sources (lasers or laser-diodes)—are considerably more expensive than those optical components operating at the visible wavelengths, the visible band is chosen for optical interrogation in this preliminary prototype in the same manner as the wired proof of concept (chapter 6.2). Successful demonstration of this prototype will confirm the ability to functionally turn on and off a mixer varistor diode using light and to wirelessly backscatter nonlinear mixing products containing neuropotential (V_m) signals for multiple channels. The mixer varistor diode for this application requires careful modeling in this unique application, as in the single channel circuit, and multichannel operation necessitates computational modeling using harmonic balance simulation in ADS and FEA of RF circuit signaling and wireless transmission in HFSS.

6.3.1. Simulation

Circuit simulation was performed in ADS to model multichannel mixer performance and in HFSS to model “implant” internal antenna, external antenna, internal

on-chip RF passives, and wireless backscattering. Despite the simplicity of the circuit structure (one mixer diode and optical switch per channel), the diode's generation of harmonic outputs as a function of input neuropotentials and externally supplied LO (P_0) and photo-bias current heavily depends on the varying impedances of the two basic circuit elements (diode and photodiode switch), passive interconnects to separate the DC, low frequency (IF or V_m) , and high frequency (LO or P_0 and RF or P_{IM3}) components, the wireless link (antenna), as well as all of the parasitics associated the integrated circuit and interconnect structures. The multichannel system consists of the backscatter unit ("implant" circuit) and an external interrogator unit that wirelessly supplies two modes of EM waveforms: P_0 at f_0 = 2.45 GHz (to activate recording or mixing operations of the backscatter unit) and light at 3 optical bands (650, 530, and 430 nm) (to activate switching or multichannel functionality of 3 channels).

Harmonic balance models in ADS were used to prepare a simple circuit to computationally measure harmonic mixing performance and ability to wirelessly record neuropotentials in multichannel form. A simplified snapshot of the ADS circuit model displaying all main circuit components and wireless link is shown in Figure 6.8. In addition to the essential basic circuit elements, the ADS circuit also incorporates circuit models for the parasitics of off-chip mounted components (diodes and photodiode switches) and on-chip interconnects (traces, wirebonds, inductors, etc.), biological recording interface, and the wireless link. Initial design formation and optimization of diode selection involved measuring the maximum magnitude of targeted IM3 harmonics output for various mixer diodes as a function of V_m, The DMK2790 diode was selected as the mixer diode due to its ability to generate high IM3 products. I_p (photo-bias current

from the photodiode switch), and for the given frequency range (f_0 = 2.45 GHz and f_{IM3} ~ 4.9 GHz), for optimally matched embedding impedances. An array of 20 photodiode elements (same surface mount components as in the proof of concept) is used as the optical switch to maximize photo-bias current in view of their less than optimal responsivity properties. Wireless optical activation of individual channel switches is simulated by manipulating the amount of photocurrent (I_p) generated by the photodiode, which correlates directly to the amount of external light irradiated for that channel. The maximum amount of total photocurrent output is set to ~ 100 μA (i.e. 20 × 5 μA per photodiode) as would be generated by externally irradiating ~ 10 – 15 mW/cm^2 intensity of light. The DC feed network between mixer diode and the photodiode array (PD array) is designed to maximize voltage bias across the mixer diode for a given amount of I_p and P_0, while blocking RF signals from the antenna and diode's harmonic output. The neuropotential input is modeled as a time-varying voltage source in parallel with a tissue impedance and bypass capacitor, and in series with electrode and DC blocking impedances. The neuropotential input is also fed through the same inductor DC feed as the PD array switch to connect and supply the mixer diode with V_m. Channels are separated from each other by a DC block capacitor (C_m). The backscatter antenna, wireless transmission in air (~ 18 mm), and external dual-band antenna for supplying P_0 and receiving backscattered P_{IM3} are modeled as an S-parameters import element (SNP1) that imports parameters simulated in HFSS. On-chip passives and interconnects (LP1 and other simple nodal wiring connections) were later replaced with more accurate S-parameter models based on HFSS layout and simulations of these components.

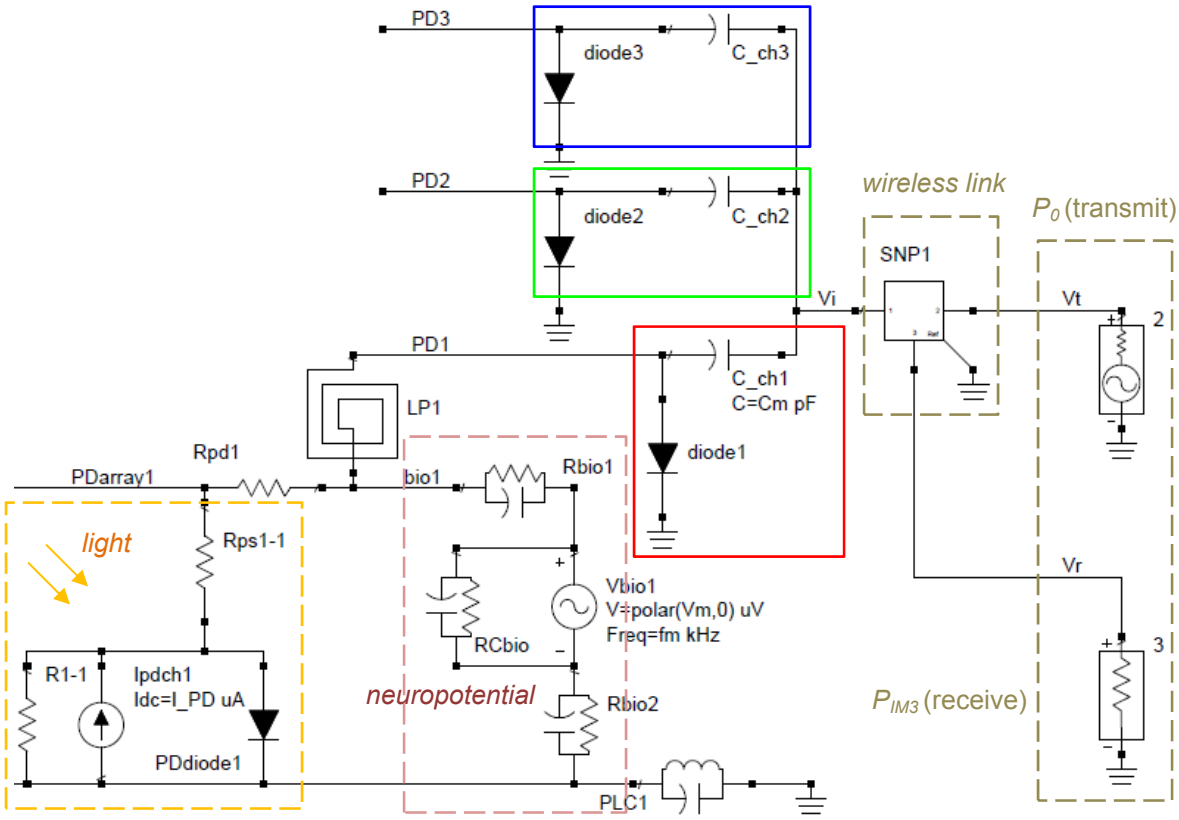

Figure 6.8. Snapshot of condensed ADS harmonic balance circuit schematic. Each recording channel is outlined in its color band of operation (channel 1 – red, channel 2 – green, channel 3 – blue) and in essence comprises a single diode for generating IM3 harmonics and a DC block capacitor for segregating photo-bias and neuropotential input for the individual channel. The mixer/recording diode of each channel is connected to both the photodiode switch (outlined in orange) and neuropotential input (outlined in brown) via an RF block (LP1) (the switch and neuropotential input is explicitly shown only for channel 1 in this condensed schematic). The photodiode switch that provides the photo-bias current (I_p) to activate diode mixing for the same channel transports DC current through a resistor and RF block to shift the DC operating point of the mixer diode and activate its ability to generate IM3 harmonics that contain the targeted

neuropotentials. The neuropotential input incorporates the tissue interface impedance as well as electrode impedances. The wireless transmission path is represented by the S-parameter data box (SNP1) imported from HFSS. The terminals on the right represent the externally supplied LO (top right) and the external RF receive port (bottom right), where P_{IM3} signals are measured.

FEA models in HFSS were used to construct the backscatter unit antenna, on-chip passives (RF block inductors) and interconnects, and external interrogator dual-band antenna, as well as to simulate the wireless radiation phenomena between backscatter unit and external interrogator in air. The HFSS layout for the entire wireless multichannel system is shown in Figure 6.9. The backscatter unit was designed on a standard 0.5 mm thick Pyrex substrate and patterned with conductive 0.5 μm thick gold. A single dual band dipole antenna, resonating near f_0 = 2.45 GHz and f_{IM3} = 4.9 GHz, was used as the backscatter unit wireless link for simplicity and ease of impedance tuneability. Antenna port impedances for the backscatter unit were set to the impedances measured for the backscatter circuit (as measured in ADS) at f_0 and f_{IM3}, to simulate and measure return loss characteristics and antenna efficiency. The wireless characteristics of the backscatter unit antenna are shown in Figure 6.10, displaying return loss ~ 3 – 4 dB at f_0 and > 20 dB at f_{IM3}. The less than optimal return loss at the LO band was not further optimized since it has marginal impact on wireless backscattering performance relative to the performance required at the RF backscatter band. Two dipole antennas, each resonating at the operational frequencies of interest (f_0 and f_{IM3}) were employed in the external interrogator, with set port impedances of 50 Ohm, equating with load terminations of

subsequent measurement apparatus (spectrum analyzer and signal generator). Return loss of > 10 dB was verified for both antennas at the targeted frequencies. On-chip passives (inductors along with wirebond and trace interconnects) were also designed and simulated to collectively present high impedances at f_0 and f_{IM3}, to effectively block RF.

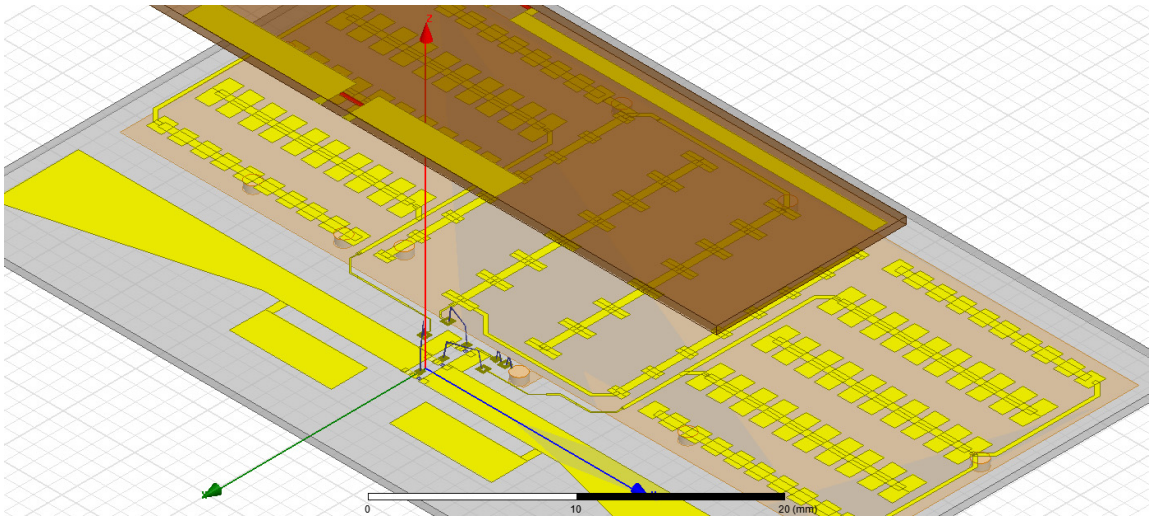

Figure 6.9. Layout of multichannel system in HFSS including both the external interrogator antennas (two dipole antennas for LO transmission of P_0 and RF reception of the targeted backscattered P_{IM3} signals) and the internal "implant" circuit. The internal system includes a dual-band phase reversed dipole antenna, an array of pads for off-chip mounting of photodiodes, and interconnects. Total dimensions are ~ 28 mm x 50 mm. The "implant" antenna is optimized for in – air operation and is 5 – 7 × larger than the equivalent tissue-implantable antenna.

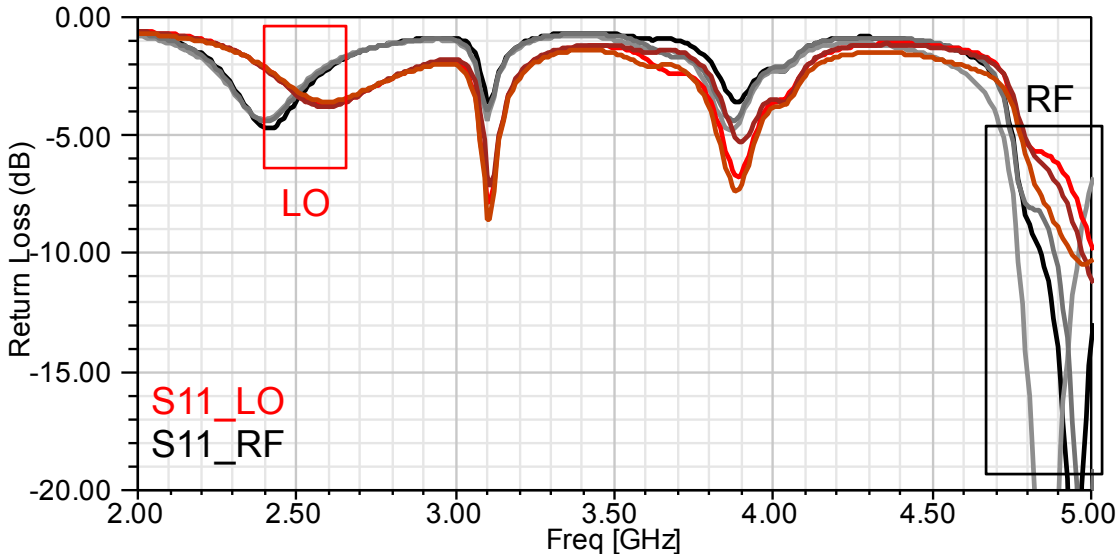

Figure 6.10. Backscatter unit antenna simulation results in HFSS. The black and gray curves represent RF return loss (*S11_RF = mag[(Z(1,1) – (72+120j)) / (Z(1,1)+(72-120j))]*) when channel ports are set to their respective input impedances as measured in ADS at f_{IM3} for optimal biasing and single channel activation ($Z_{in,RF}$ = 72 – j120 Ohm). The red curves represent LO return loss (*S11_LO = mag[(Z(1,1) – (160 + 135j)) / (Z(1,1) + (160-135j))]*) when channel ports are set to their impedance values as determined in ADS at f_0 ($Z_{in,LO}$ = 160 – j135 Ohm). The three curves displayed per LO / RF operation band represent the return loss as measured per channel (since the position of each channel's port within antenna terminals is slightly different).

Results from HFSS FEA simulations were exported back to ADS to optimize harmonic balance circuit models and measure the final performance of the multichannel circuit. Simulation results for channel to channel isolation as a function of externally radiated P_0 are shown in Figure 6.11. Here, only 2 channels are shown with one channel activated by photo-bias and the other off (zero photo-bias current supplied). However, the

results are essentially with an additional 3rd channel that is turned off; the off 3rd channel P_{IM3} trails the off 2nd channel P_{IM3} curve. The results show > 40 – 50 dB channel to channel isolation ($P_{IM3,on}$ / $P_{IM3,off}$) for V_m of 50 – 500 μV and external $P_0 \leq 5$ dBm, indicating very little channel to channel interference when only a single channel's recording operation is activated by light. In essence, the off channel is at noise floor level, and would be marginally if not at all detected by the external interrogator. Furthermore, for the on channel, SNR is ~ 45 dB and ~ 25 dB for V_m = 500 μV and 50 μV, respectively, which is sufficiently resolvable by the external interrogator to wirelessly recover targeted neuropotential signals. On the other hand, P_0 must be well controlled since as P_0 increases above 5 dBm, channel to channel isolation degrades as the intended off channel starts to generate increasing $P_{IM3,off}$ due to the DC self-biasing effects of the induced P_0 carrier signal and the $P_{IM3,on}$ levels off due to the overshadowing effects of the spreading resistance of the mixer diode that occurs during higher levels of forward conductance operation. Channel to channel isolation results at a fixed P_0 = 5 dBm as a function of the supplied neuropotential signal magnitude ($V_m = V_{m1} = V_{m2}$) are shown in Figure 6.12, revealing that P_{IM3} reaches noise floor level near $V_m \sim 2$ μV and a resolvable SNR ~ 10 dB near V_m ~ 8 μV, which may delineate the minimum detectable neuropotential.

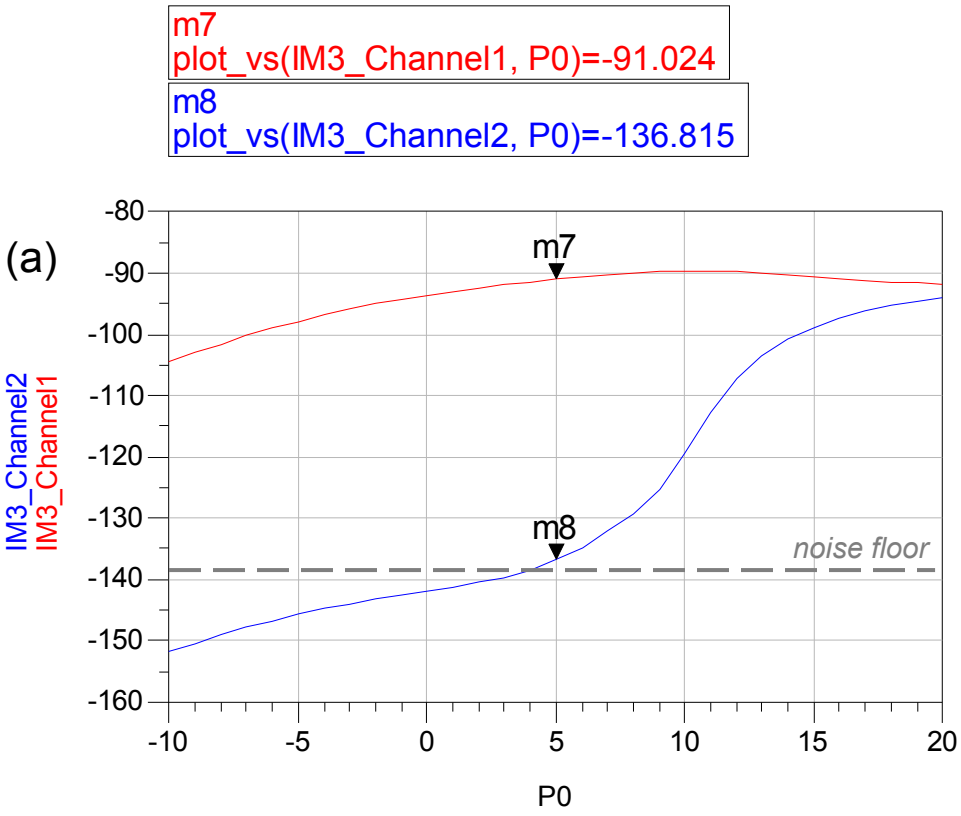
m7
plot_vs(IM3_Channel1, P0)=-91.024
m8
plot_vs(IM3_Channel2, P0)=-136.815
(a)
m7
m8
noise floor
IM3_Channel2
IM3_Channel1
-80
-90
-100
-110
-120
-130
-140
-150
-160
-10
-5
0
5
10
15
20
P0

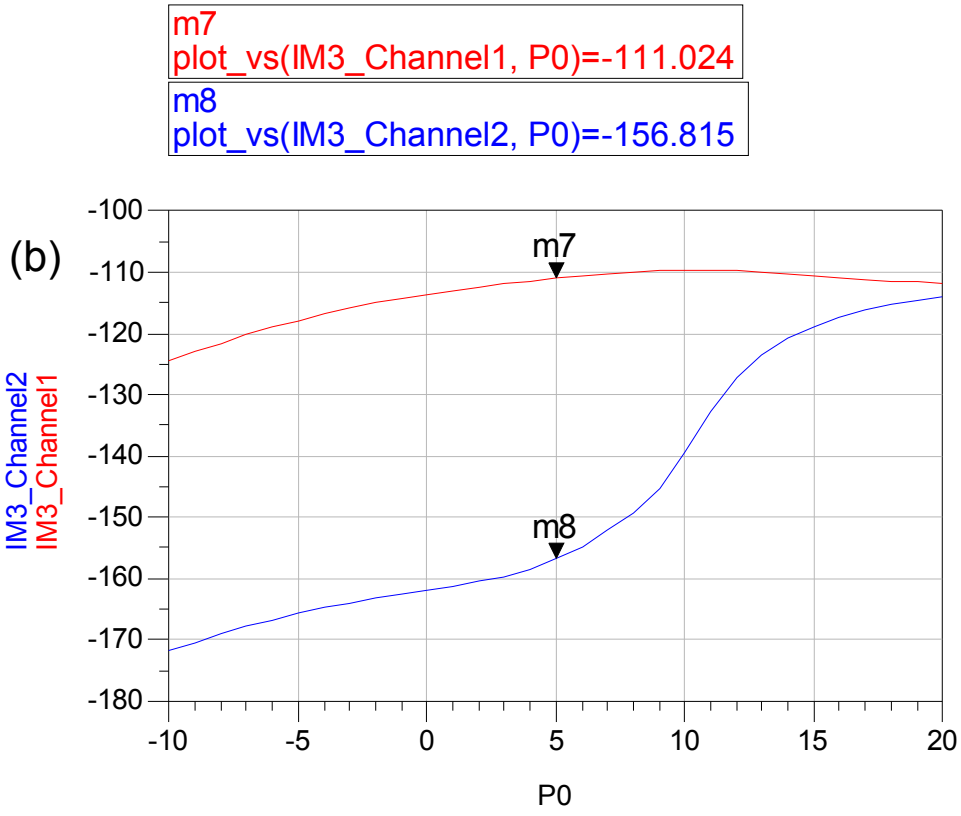
m7
plot_vs(IM3_Channel1, P0)=-111.024
m8
plot_vs(IM3_Channel2, P0)=-156.815
(b)
m7
m8
IM3_Channel2
IM3_Channel1
-100
-110
-120
-130
-140
-150
-160
-170
-180
-10
-5
0
5
10
15
20
P0

Figure 6.11. Harmonic balance simulations of channel to channel isolation as a function of LO power. Data is plotted as power of the $2f_0 \pm f_m$ harmonics (P_{IM3} in dBm) wirelessly backscattered and received by the external interrogator versus the externally wirelessly supplied LO power (P_0 in dBm). Data for 2 channels are shown: the red curve represents the "on" channel activated by setting $I_p = 5 \times 20$ µA (relates to amount of irradiated light on array of photodiodes) and the blue curve represents the "off" channel where $I_p = 0$ µA. (a) Wirelessly backscattered P_{IM3} for an input neuropotential $V_m = 500$ µV. Noise floor (~ - 137 dBm according to currently equipped spectrum analyzer at a bandwidth of 1 kHz) is depicted as a dashed line. (b) P_{IM3} for an input neuropotential $V_m = 50$ µV.

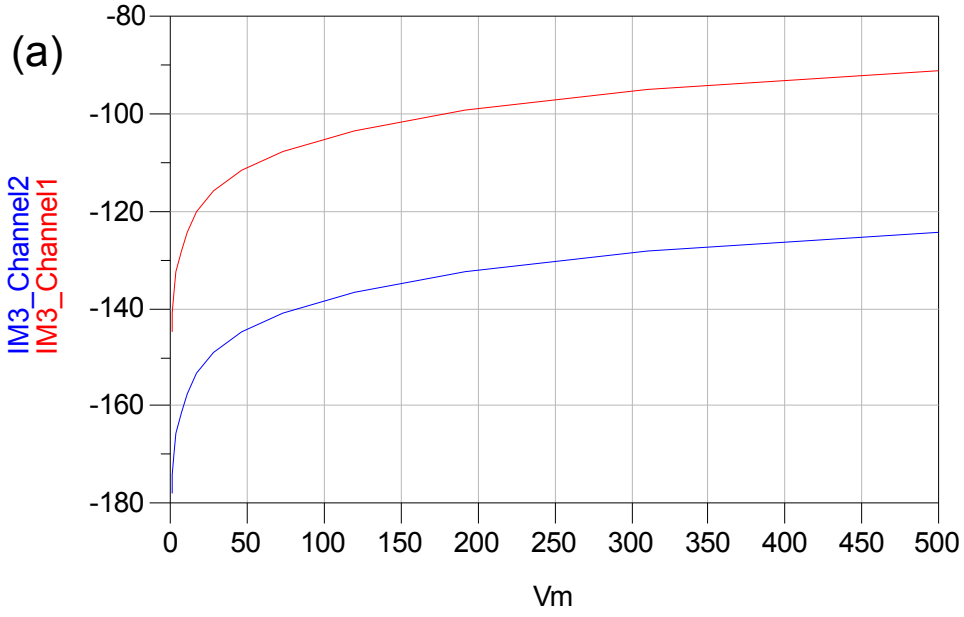

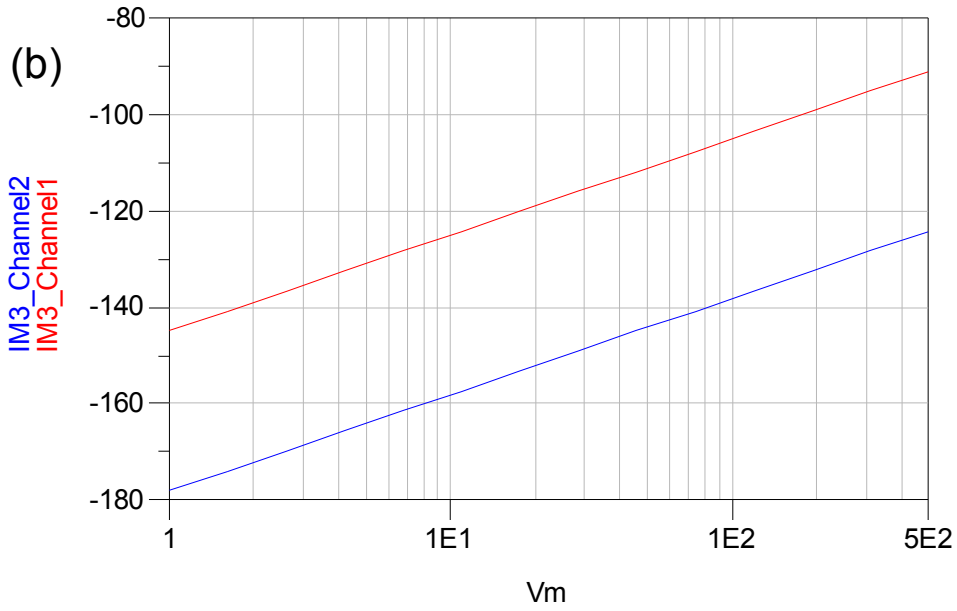

Figure 6.12. Harmonic balance simulations of channel to channel isolation as a function of input magnitude of neuropotentials, V_m. Data is plotted as power of the $2f_0 \pm f_m$ harmonics (P_{IM3} in dBm) wirelessly backscattered and received by the external interrogator versus the input V_m (in μV). Data for 2 channels are shown: the red curve represents the "on" channel activated by setting I_p = 5 × 20 μA and the blue curve represents the "off" channel where I_p = 0. (a) Wirelessly backscattered P_{IM3} for an input neuropotential P_0 = 0 dBm. (b) The same on a log x-axis scale.

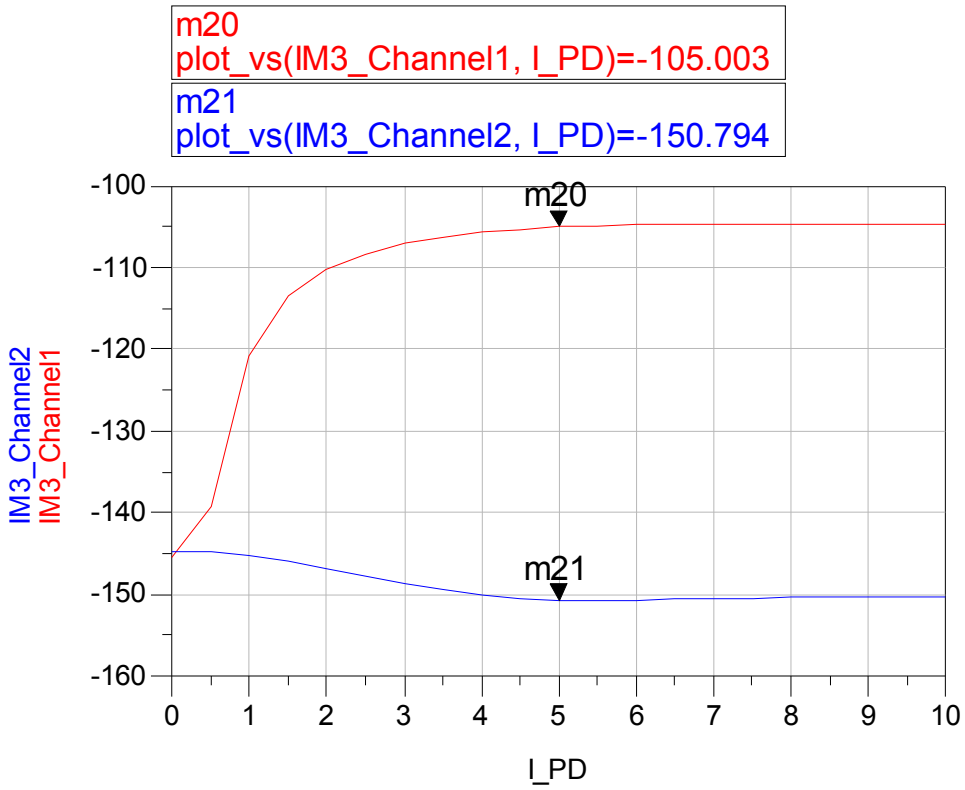

Figure 6.13. Harmonic balance simulations of channel to channel isolation as a function of photo-bias current (I_p) generated in proportion to the externally irradiated light. I_p is supplied only to the on channel 1 (red) and is set to zero for the off channel 2 (blue). Data is plotted as power of the $2f_0 \pm f_m$ harmonics (P_{IM3} in dBm) wirelessly backscattered versus the input I_p (in μA). The x-axis should be scaled by 20 as it corresponds to only the photocurrent generated by a single photodiode and not the array of 20 photodiodes. P_0 = 5 dBm and V_m = 100 μV.

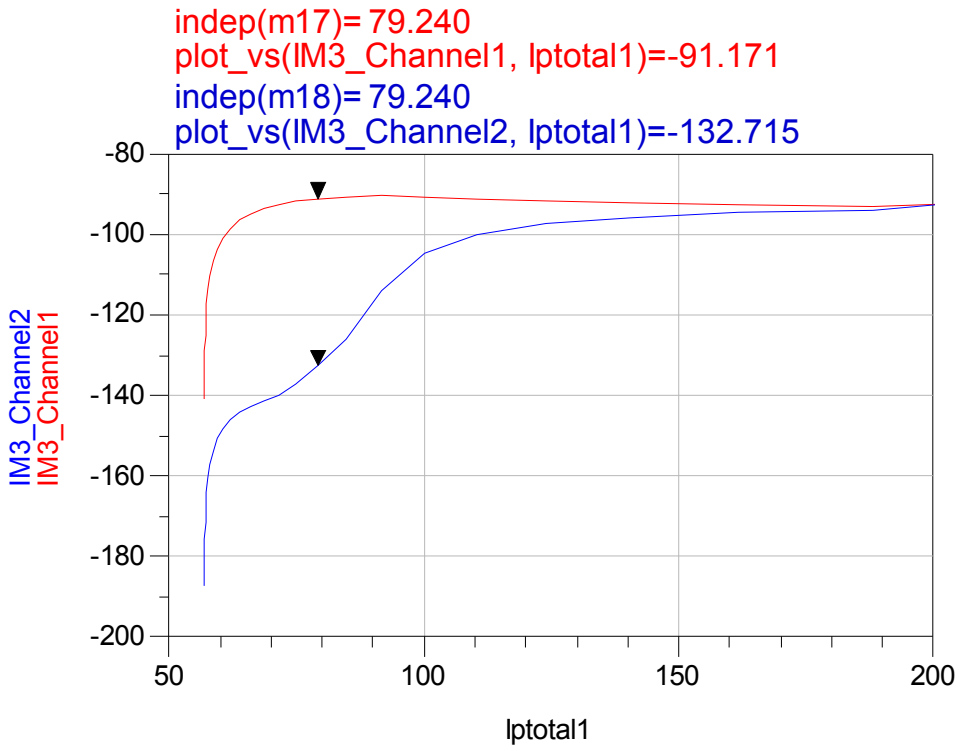

Figure 6.14. P_{IM3} (dBm) vs. total DC current through channel 1 mixer diode (μA) as generated by both $I_p \times 20$ (arrayed photo-bias current from photodiode switches) plus the rectified mixer diode current from externally radiated P_0. I_p is supplied only to the on channel 1 (red) and is set to zero for the off channel 2 (blue). P_0 swept from - 20 – +30 dBm, V_m = 500 μV, and I_p = 5 μA × 20 = 100 μA (channel 1 only). The plot shows that with increasing P_0 and resulting increased total DC current through mixer diode (I_{ptotal}), IM3 products saturate and multichannel operations become nullified as $P_{IM3,ch2}$ increases towards $P_{IM3,ch1}$ level and decreases channel to channel isolation ($P_{IM3,ch1}/P_{IM3,ch2} \rightarrow 1$). Despite I_p set to 100 μA, the steady-state DC current observed through the mixer diode is 56 μA (when $P_{IM3} \rightarrow 0$ or $-\infty$ dBm or curve drops towards left indicating current generated from photodiodes only). The reason why not all of the photodiode generated current is not equal to that seen across the mixer diode is because the photodiode

dissipates its own current through its own forward conducting variable resistance (refer to equivalent photodiode circuit) with increasing illumination.

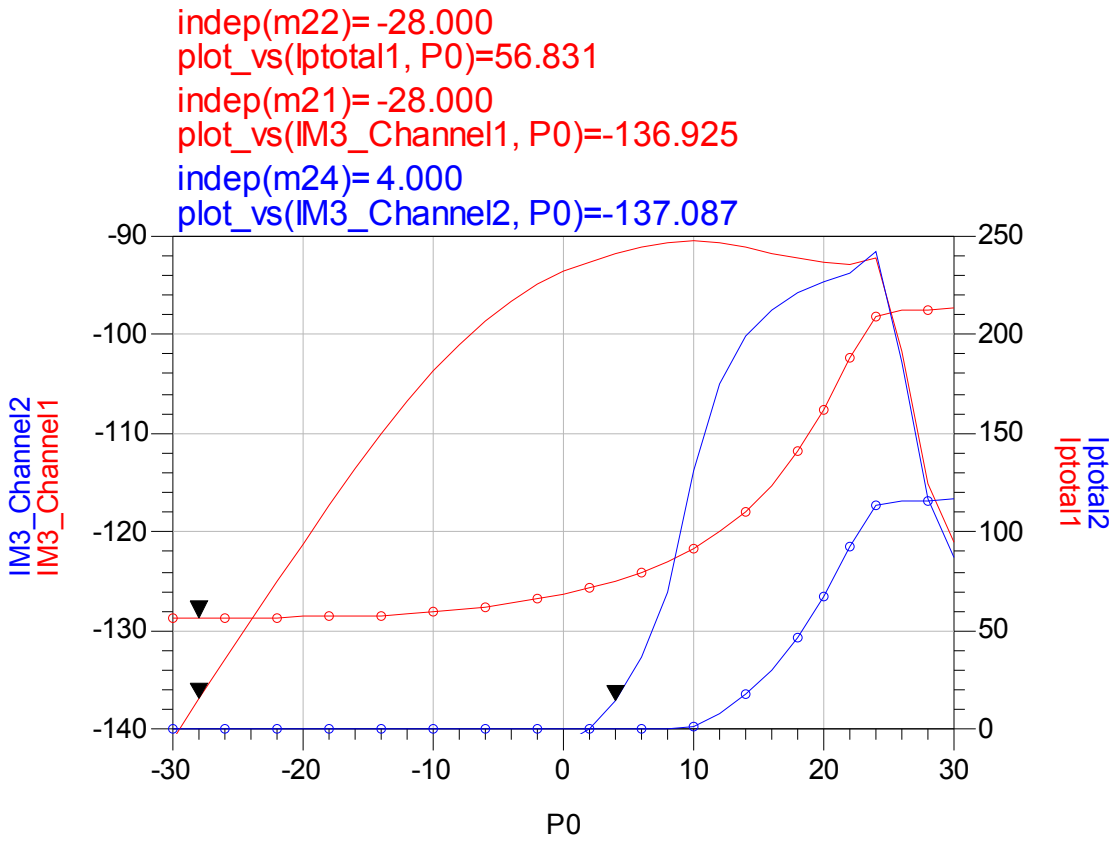

Figure 6.15. P_{IM3} (dBm) (left y-axis) and total DC current, I_{ptotal}, for respective channel mixer diodes (μA) (right y-axis) vs. P_0 (dBm). I_p is supplied only to the on channel 1 (red) and is set to zero for the off channel 2 (blue). The plot shows that even with negligible supply of P_0 (< -20 dBm), the photo-bias allows generation of P_{IM3} for channel 1 (on channel, photo-bias from photodiodes, $I_{p,ch1}$ = 5 × 20 μA) recording. In contrast, generation of P_{IM3} for channel 2 (off channel, no photo-bias from photodiodes, $I_{p,ch2}$ = 0) above the noise floor level requires at least P_0 > 5 dBm. Markers indicate "threshold" or

noise floor level. P_0 swept from - 30 – +30 dBm, V_m = 500 µV, and $I_{p,ch1}$ = 5 × 20 µA (actual I_p through diode ~ 57 µA as indicated by top marker caption).

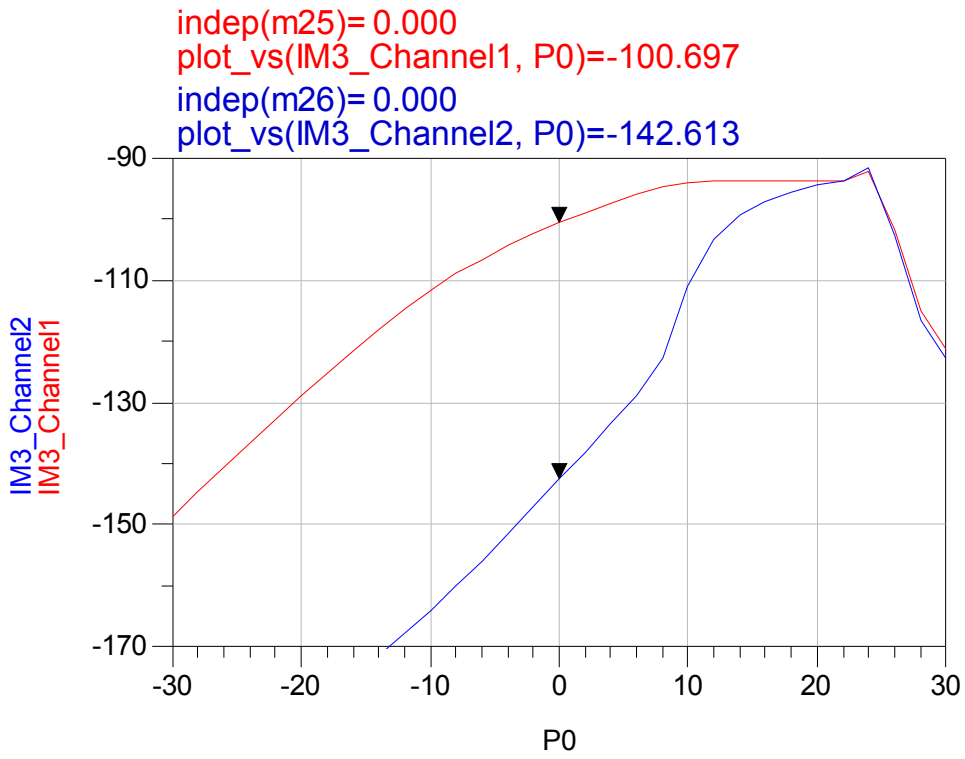

Figure 6.16. P_{IM3} (dBm) vs. P_0 (dBm) for lower photo-bias or light irradiation of on-channel switch and with V_m = 500 µV. Channel 1 supplied I_p = 2 µA × 20 = 40 µA. I_p is set to zero for the off channel 2 (blue).

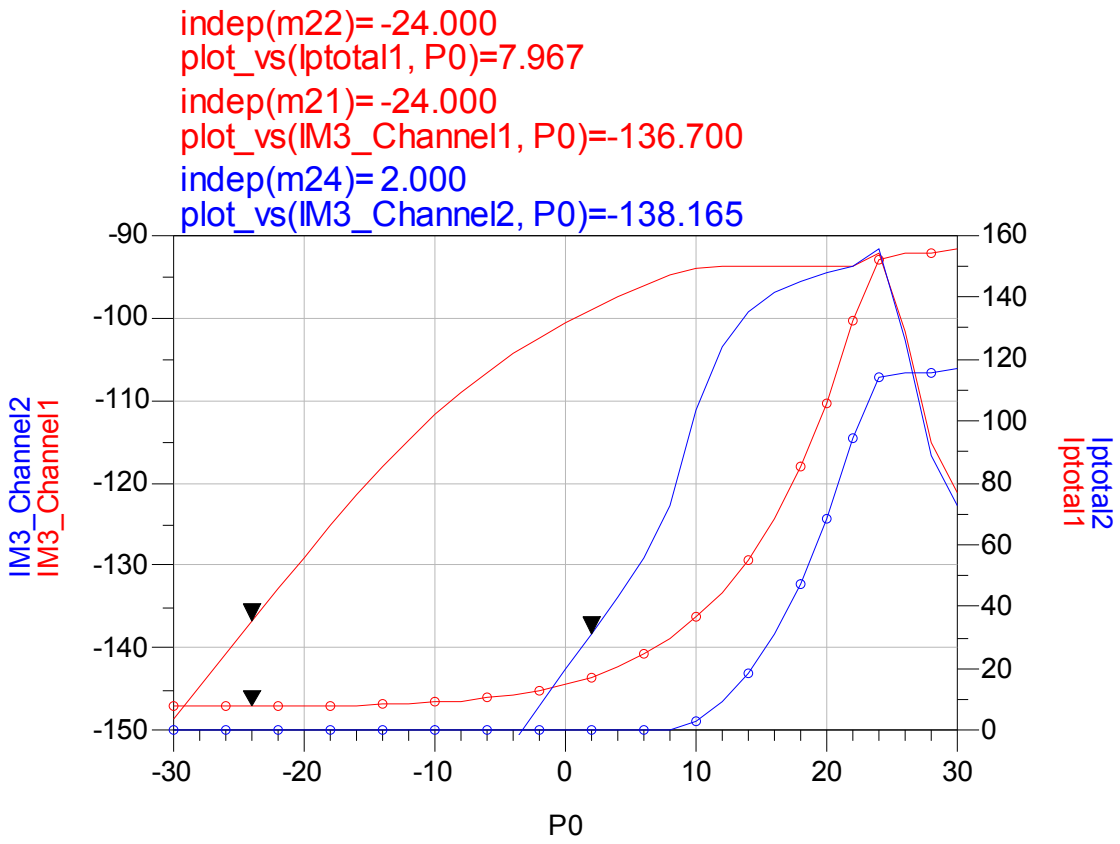

Figure 6.17. P_{IM3} (dBm) (left y-axis) and total DC current, I_{ptotal}, for respective channel mixer diodes (μA) (right y-axis) vs. P_0 (dBm) for lower photo-bias or channel 1 supplied I_p = 2 μA × 20 = 40 μA (actual I_p through diode ~ 8 μA as indicated by top marker caption) and V_m = 500 μV.

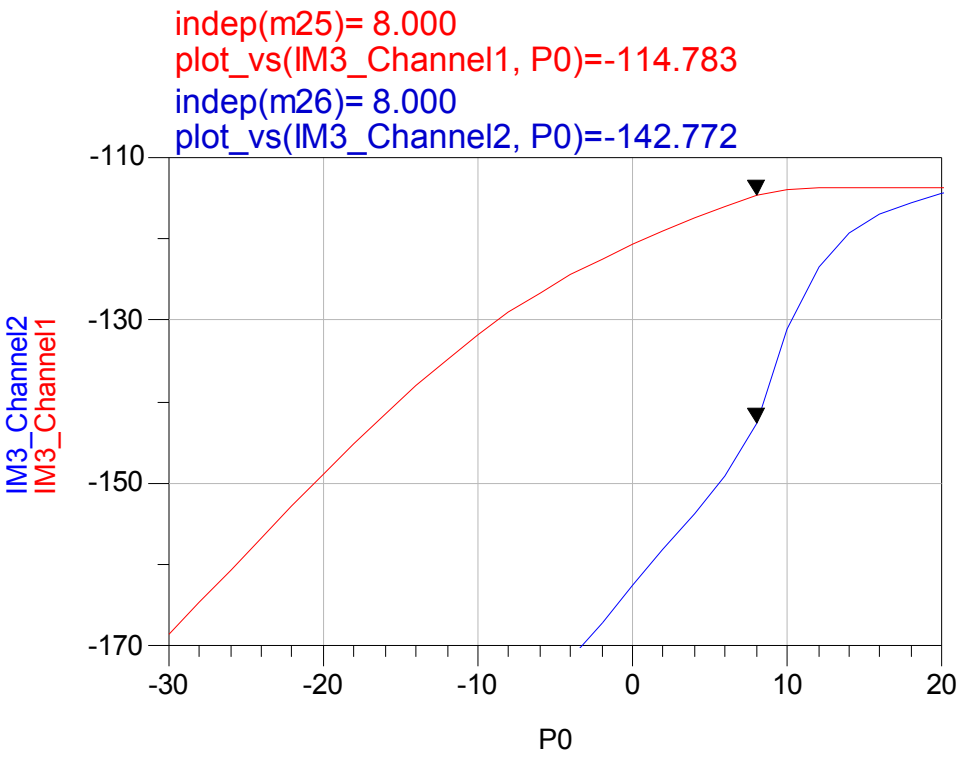

Figure 6.18. P_{IM3} (dBm) vs. P_0 (dBm) for lower photo-bias of on-channel (I_p = 40 μA) and with lower neuropotential input of V_m = 50 μV. Actual I_p through diode ~ 8 μA.

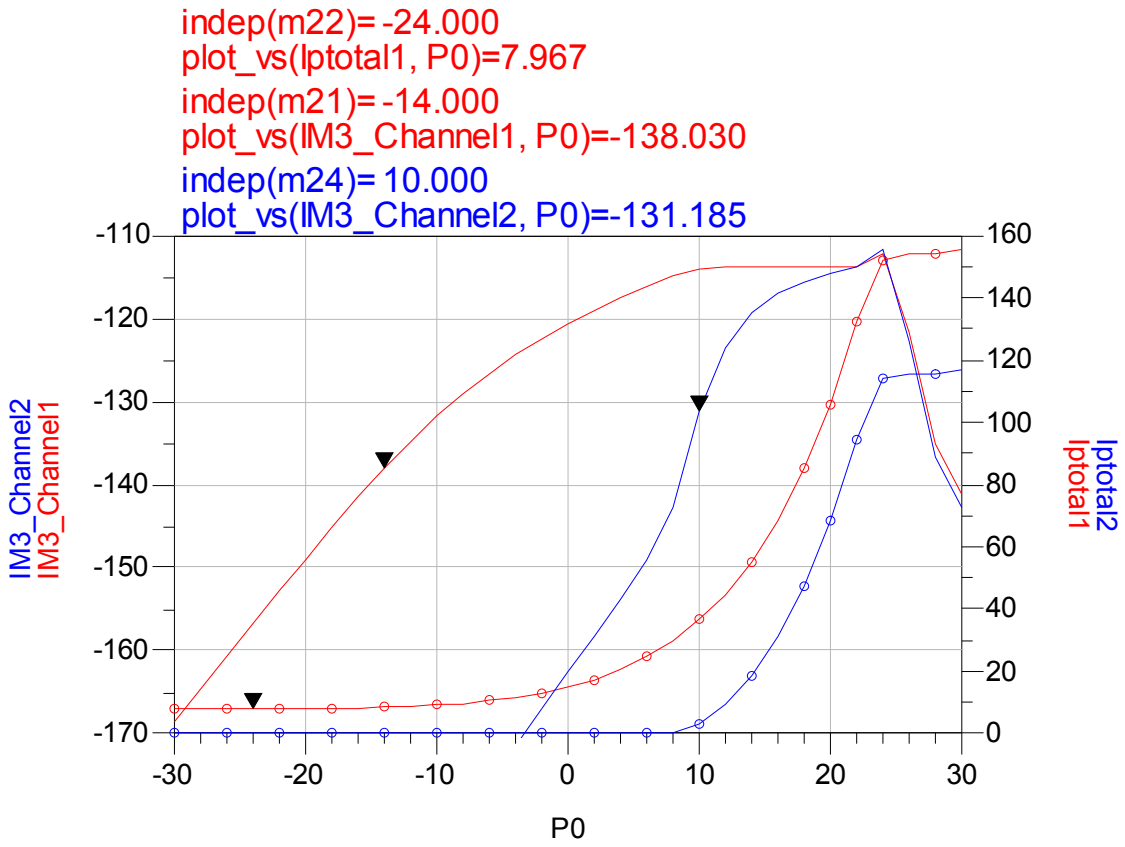

Figure 6.19. P_{IM3} (dBm) (left y-axis) and total DC current, I_{ptotal}, for respective channel mixer diodes (μA) (right y-axis) vs. P_0 (dBm) for I_p = 40 μA (actual I_p through diode ~ 8 μA as indicated by top marker caption) and V_m = 50 μV.

Table 6.1. Design specifications for wireless multichannel neurorecording.

	Specifications		**Use**
Off-Chip Mounted Components			
Photodiodes for PD switch	*I_p per mW/cm^2 light*	*Bandwidth*	
PD93-21C (Everlight)	1.2 uA	400 – 1150 nm	x 20 – 28 in PD array (blue channel)
PD15-22C (Everlight)	5 – 6.5 uA	500 – 1050 nm	x 20 in PD array (red/green channels)
Mixer diode (GaAs flip-chip)	*Key parameters*		

DMK2790 (Skyworks)	C_{j0} = 0.05 pF V_j = 0.82 V	γ = 0.26 *Rs* = 4 Ohm	essential mixing & recording functions
DC block capacitor	*Capacitance*	*RF performance*	
06031U510FAT2A (AVX)	51 pF	Low ESR / SRF	separates channels
On-Chip Elements			
	Impedance at f_0 (2.45 GHz)	*Impedance at f_{RF} (4.9 GHz)*	
Z_{in} backscatter circuit (ideal on-chip elements)	160 - j135 Ohm	72 - j120 Ohm	for optimal photo-bias / single channel
Z_{in} backscatter circuit (FEA on-chip elements)	~ same as above	66.7 - j130 Ohm	same as above
PD DC feed	990 Ohm (magnitude)	600 - 1500 Ohm (magnitude)	blocks RF to PD switch
Z_{in} integrated antenna	27 + j184 Ohm	63 + j65 Ohm	wireless link

6.3.2. Fabrication

Fabrication of the backscatter unit and external interrogator antennas involved standard photolithography processes on Pyrex wafers. Because of the small features of on-chip passive inductors (20 μm pitch, 10 μm trace width, and 400 – 500 μm diameter), high resolution masks were used for patterning conductive traces. The fabrication process involved in brief: i) cleaning wafers in methanol in ultrasonic bath for 5 minutes to remove dust particles, ii) topside sputtering Cr/Au ~ 100 nm / 400 nm thick, iii) spinning 4 μm thick photoresist (2000 rpm, AZ4330), with 60 s softbake, iv) using a soft-contact aligner to transfer mask patterns (~200 mJ/cm^2), followed by developing in MIF300 with mild agitation, v) patterning Au by wet etching using GE-4148 (<10 seconds at room temperature) with mild agitation and patterning of Cr by wet etching (~30 seconds) with

mild agitation, and vi) masking backside areas with low-adhesive tape and sputtering Cr/Au ~ 100 nm / 400 nm thick on backside. Individual backscatter unit circuits and external antennas were diced using a dicing machine with topside wafer protection using photoresist. Ultrasonic based wirebonding of inductor pads was performed using a wirebond tool with aluminum wirebonds having a diameter of 25 μm. Off-chip components were mounted onto the backscatter unit circuit using silver epoxy and cured at 120 ºC for ~ 30 minutes. Color absorptive filters for individual channels (channel 1, red = 650 nm, channel 2, green = 530 nm, and channel 3, blue = 430 nm) were mounted onto respective photodiode arrays using double-sided tape. Photographs of fabricated multichannel circuits are shown in Figure 6.20.

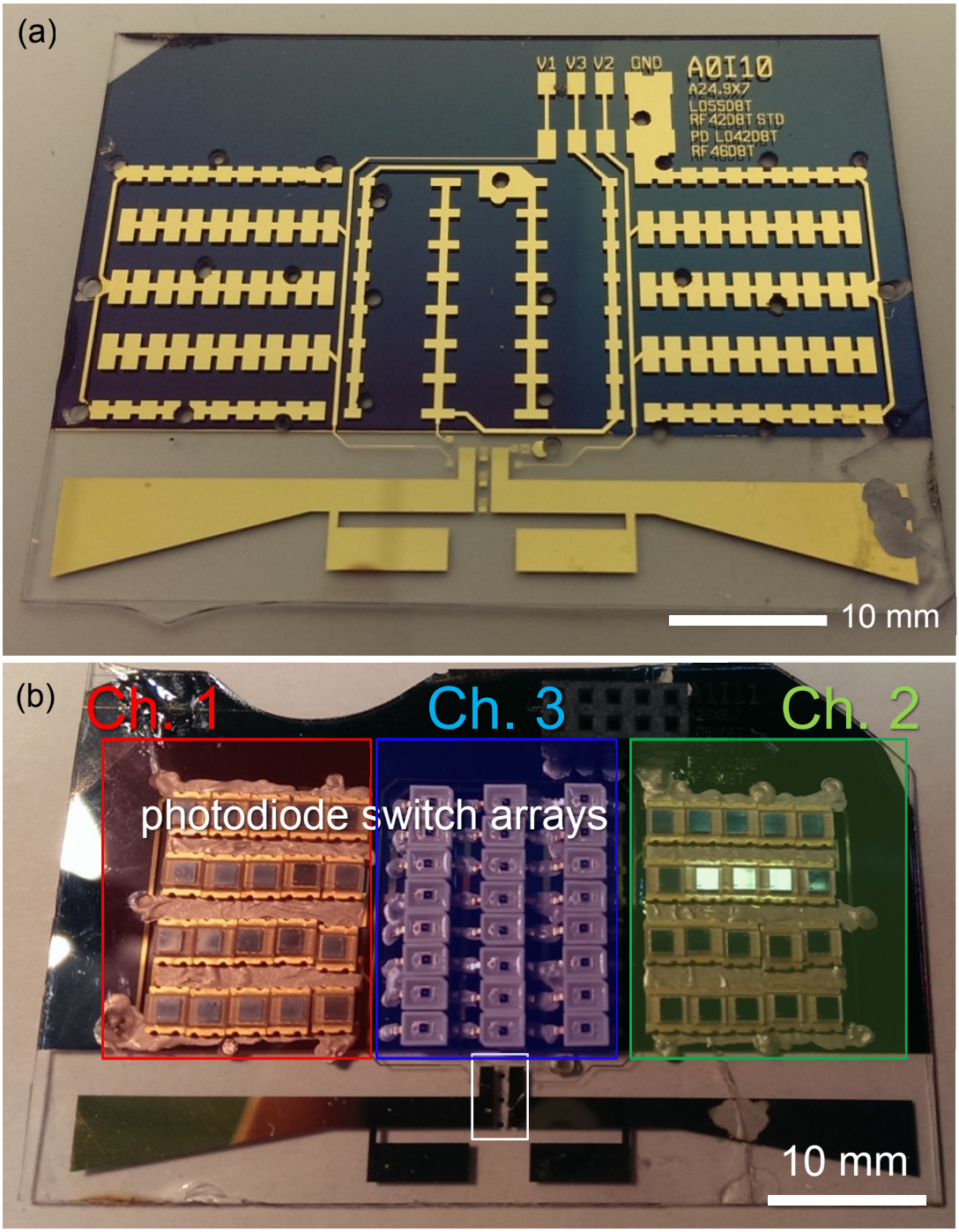
(a)
V1 V3 V2 GND
A0I10
A24.9X7
LD55D8T
RF42D8T STD
PD LD42D8T
RF46D8T
10 mm
(b)
Ch. 1
Ch. 3
Ch. 2
photodiode switch arrays
10 mm

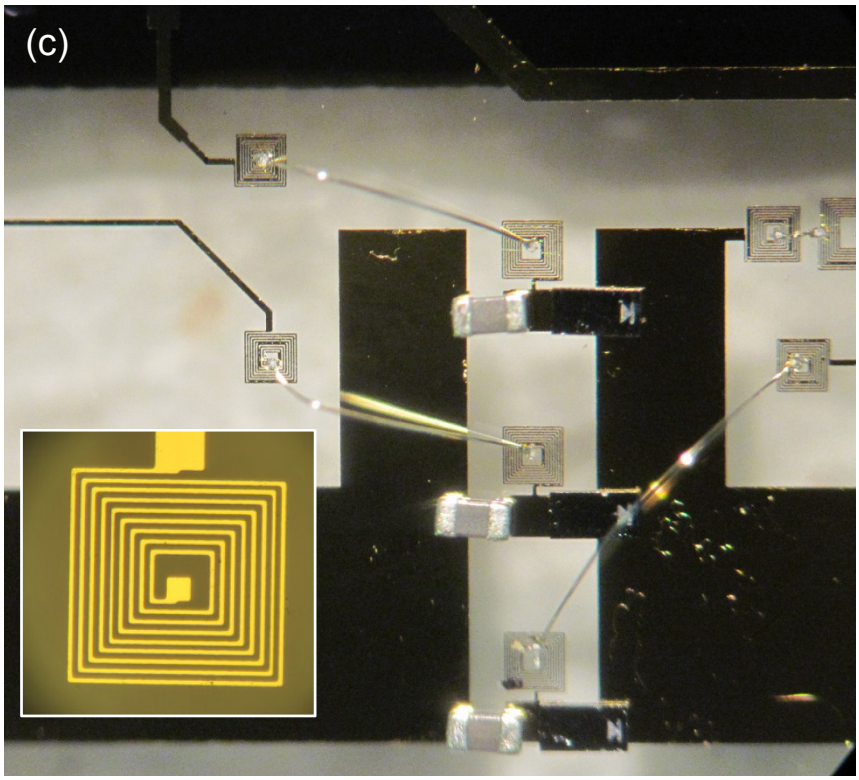

Figure 6.20. Photograph of fabricated multichannel neurorecording circuit (backscatter unit) before (a) and after assembly with off-chip diodes, capacitors, and photodiode switches (b). (c) Close-up of multichannel mixing circuit involving the 3 channel mixer diodes and channel isolation capacitors placed between antenna terminals as outlined in white in (b). Inset on bottom left shows close-up of a fabricated RF block inductors residing between antenna terminals.

6.3.3. Results

Wireless benchtop testing of the multichannel neurorecording system was performed in the same manner as proof of concept testing (chapter 6.2.1), except that here the data link for backscattering neuropotentials is provided wirelessly through use of an integrated antenna on the backscatter unit ("implant" circuit) along with wireless

activation of optical switches for multichannel functionality. Two resonant dipole antennas constructed on PCB were used as the wireless external transmit/receive antennas (both on same substrate) for supplying P_0 (f_0 = 2.45 GHz) and receiving backscattered P_{RF} signals, including targeted P_{IM3} harmonics at $2f_0 \pm f_m$, respectively. P_0 was generated by a signal generator and output power was varied between 0 – 12 dBm. Identical LED light sources (Cree, Inc.) were used to supply light irradiation to wirelessly activate the optical switches for multichannel functionality at dominant wavelengths of, λ = 650 (red), 530 (green), and 430 (blue) nm, for channels 1, 2, and 3, respectively. 6 LEDs were used as each channel's light source to ensure sufficient light irradiation and resulting channel activation. Each neuropotential recording channel was made unique by setting each neuropotential with a different frequency for each channel, f_{m1} = 350 Hz, f_{m2} = 400 Hz, f_{m3} = 450 Hz, while fixing the amplitude of each so that $V_m = V_{m1} = V_{m2} = V_{m3}$. The magnitude of the emulated neuropotentials, maintained across all channels, was varied between $0.7 \leq V_m \leq 10$ mV_{pp}. The external interrogator antenna was fixed at a certain separation distance to the backscatter unit ranging from ~ 3 mm to 38 mm. The external light sources were oriented towards the onboard optical switches of the backscatter unit and at a distance of ~ 30 – 50 mm from the backscatter unit. The entire wireless system was enclosed in a light absorptive box to block out diffuse ambient light that would inevitably turn on unsolicited channels and disturb channel to channel and on/off isolation. Backscattered P_{RF} signals containing targeted P_{IM3} ($2f_0 \pm f_m$) signals were measured through a spectrum analyzer with a 1 kHz span and resolution bandwidth of 1 Hz (noise floor ~ -136 – -138 dBm).

Recorded P_{RF} spectra for individual optical activation of the three channels for a V_m = 7 mV_{pp}, P_0 = 0 dBm, and separation between backscatter unit and external interrogator antennas of 3 – 4 mm, are shown in Figure 6.21, 6.22, 6.23, for activation of channel 1, channel 2, and channel 3, respectively. The magnitude of the targeted harmonics containing neuropotentials, $P_{IM3,}$ for the on channel that is activated by its corresponding wavelength of light is considerably higher (~ 14 – 20 dB) than the P_{IM3} for the off channels (possessing optical switches that reject most of the bands of light irradiated for the channel of interest). The ability of light to substantially increase the P_{IM3} for a specified individual channel over other channels makes conceivable the functionality of multichannel recording: by serially sweeping the wavelength of the illuminating external light source to sequentially read corresponding successive channels and discriminate the multiple sites of neuropotentials inputted to the individual channels of the backscatter "implant" unit. Figure 6.24 illustrates the performance of individual channel activation operations as a function of wirelessly supplied P_0 and signify the performance of optical modalities. In theory, given perfectly pure spectral light sources and their corresponding filter embedded photodiode optical switches, the ch – ch selectivity (ratio of P_{IM3} of the on channel to the P_{IM3} of the off channels) should equal on – off isolation (ratio of P_{IM3} of the channel turned on to the P_{IM3} of the same channel turned off). However, in practice, due to the imperfect out of band rejection of light sources and corresponding switch filters, light supplied for a specified channel will inevitably diffuse through other channel switches and turn on, to a finite extent, these peripheral channels. On the other hand, on – off isolation represents the amount of increase in P_{IM3} with optical switch activation through light excitation versus the P_{IM3}

with no light and no photo-bias to activate the optical switches (I_p = 0). The degradation of ch – ch selectivity is most notable in Figure 6.24 (c) where the channel 3 (blue) light source (λ_{ch3} = 430 nm) raises the P_{IM3} levels of channels 1 and 2 above the P_{IM3} originally measured in complete darkness without any light irradiation. This interference is indicated by the upwards shift in the dashed P_{IM3} curves (no light) of channels 1 and 2 to their corresponding solid curves with light activated at the extraneous λ_{ch3}. Nevertheless, ch – ch selectivity may be increased to correspond with on – off isolation through the use of narrower and more selective light sources and optical filters. Figure 6.25 displays the on – off isolation measurements made for a single channel by turning on and off external light and measuring the wirelessly backscattered P_{IM3} at both light and dark states for optimal P_0. The measurements of on – off isolation are made as a function of input neuropotential amplitudes (V_m = 0.7 – 10 mV_{pp}). The lowest detectable neuropotential signal of V_m = 0.7 mV_{pp} is specified by its ability to produce an SNR of ≥ 10 dB (for a noise floor of ~ -137 dBm) and is capable of generating an on – off isolation of ~ 10 – 16 dB. Most of these preceding measurements were executed under optimal separation spacing between the backscatter unit and the wireless external interrogator to maximize the power of the targeted backscattered harmonics, P_{IM3}. The maximum wireless read distance measured was ~ 38 mm that produced an SNR of ≥ 10 dB for the on channel and on – off isolation of ≥ 6 – 8 dB for a V_m = 10 mV_{pp}.

The ability to wirelessly record neuropotentials from multiple channels and with amplitudes as low as 700 μV_{pp} in a fully passive manner (without any on-chip control circuitry and/or power supply components) promotes future expansion of this work towards an implantable form. The sensitivity may be further improved to detect lower

level neuropotentials in the range of tens of *microvolts* by optimizing on-chip passives and circuit fabrication to reduce RF losses associated with parasitics to augment P_{IM3} (as demonstrated in simulation in section 6.3.1, as shown, for example, in Figure 6.11). Ch – ch selectivity may be improved through the use of enhanced optical light sources and integrated optical switch filters. Miniaturization of the circuit for brain implant feasibility is certainly feasible by monolithic fabrication of all mixer diode components along with optical light-activated switches (ie. photodiodes) and the air-operating antenna may be readily reduced by a factor of 7 – 10 × in length corresponding to the lower phase velocity of impinging high frequency EM waves in the intended higher dielectric biological tissue.

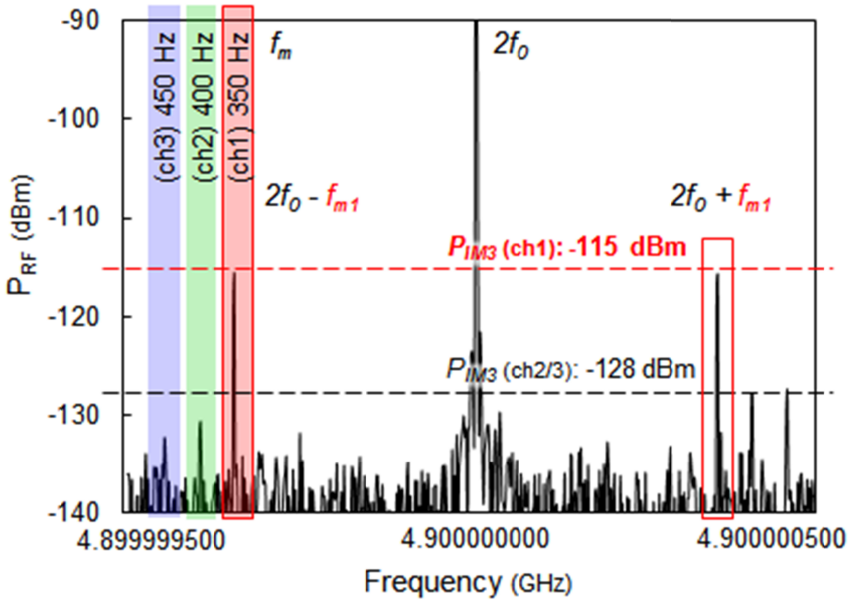

Figure 6.21. Wirelessly measured P_{RF} spectrum for P_0 = 0 dBm at f_0 = 2.45 GHz, V_m = 7 mV_{pp}, and external light supplied at λ ~ 650 nm targeting activation of channel 1 (red) optical switches onboard the backscatter unit and to wirelessly record channel 1

neuropotentials (f_{m1} = 350 Hz). The P_{IM3} of the on channel 1 are outlined in red and are ~ -115 dBm. The P_{IM3} of intended off channels are also observed closer to noise floor level and are ~ -128 dBm. The ratio between P_{IM3} of the on channel 1 and P_{IM3} of the off channels (channel 2/3) is denoted as the channel-to-channel isolation and for this measurement is $P_{IM3,ch1} / P_{IM3,ch2/3}$ ~ 13 dB.

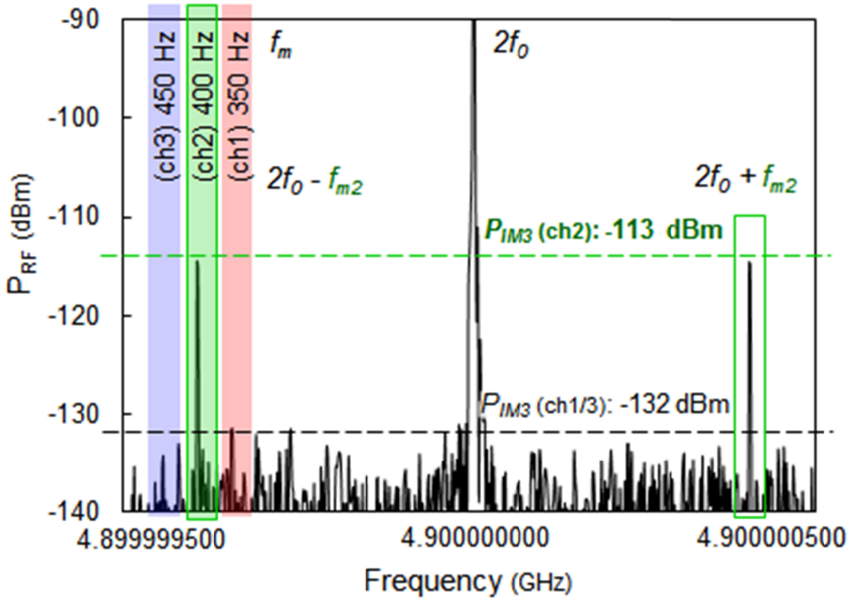

Figure 6.22. Wirelessly measured P_{RF} spectrum for P_0 = 0 dBm at f_0 = 2.45 GHz, V_m = 7 mV_{pp}, and external light supplied at λ ~ 530 nm targeting activation of channel 2 (green) optical switches onboard the backscatter unit and to wirelessly record channel 1 neuropotentials (f_{m2} = 400 Hz). The P_{IM3} of the on channel 2 are outlined in green and are ~ -113 dBm. The P_{IM3} of intended off channels are ~ -132 dBm, resulting in a channel-to-channel isolation of $P_{IM3,ch2} / P_{IM3,ch1/3}$ ~ 19 dB.

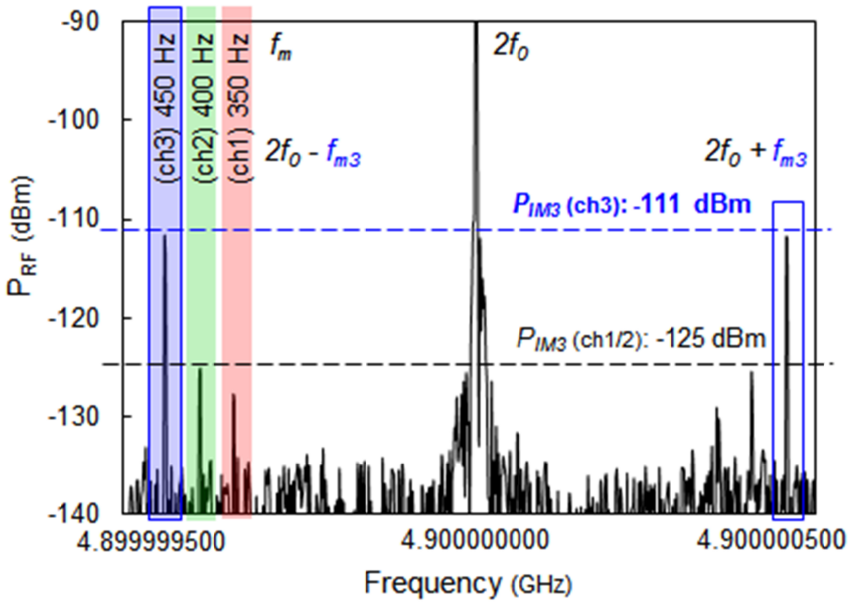

Figure 6.23. Wirelessly measured P_{RF} spectrum for P_0 = 0 dBm at f_0 = 2.45 GHz, V_m = 7 mV_{pp}, and external light supplied at λ ~ 430 nm targeting activation of channel 3 (blue) optical switches onboard the backscatter unit and to wirelessly record channel 1 neuropotentials (f_{m3} = 450 Hz). The P_{IM3} of the on channel 3 are outlined in blue and are ~ -111 dBm. The P_{IM3} of intended off channels are ~ -125 dBm, resulting in a channel-to-channel isolation of $P_{IM3,ch3} / P_{IM3,ch1/2}$ ~ 14 dB.

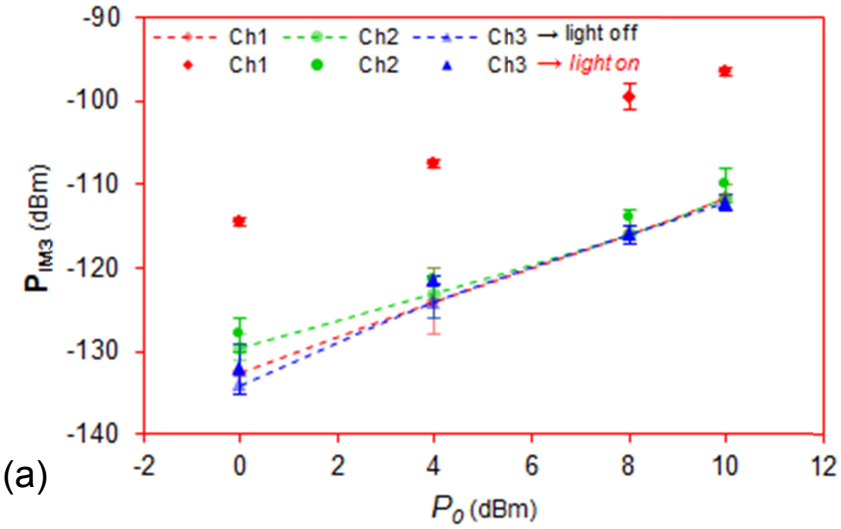
Ch1 Ch2 Ch3 → light off
Ch1 Ch2 Ch3 → light on
P_{IM3} (dBm)
P_0 (dBm)

(a)

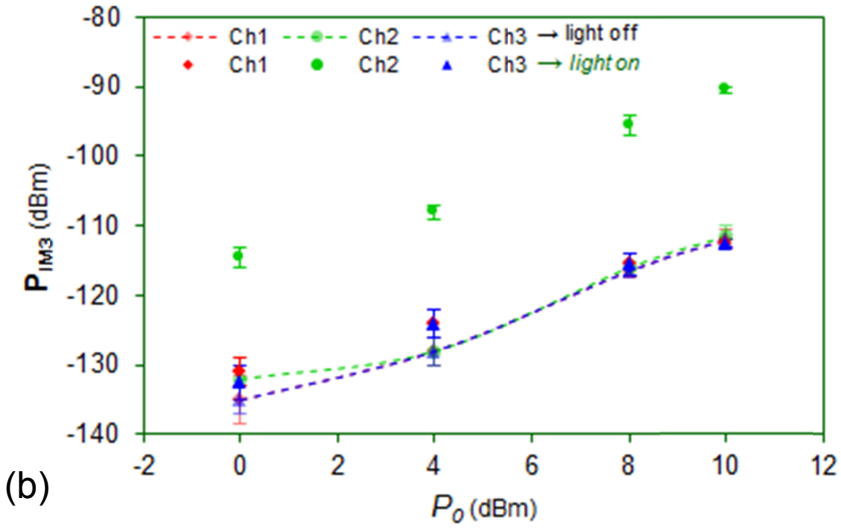
Ch1 Ch2 Ch3 → light off
Ch1 Ch2 Ch3 → light on
P_{IM3} (dBm)
P_0 (dBm)

(b)

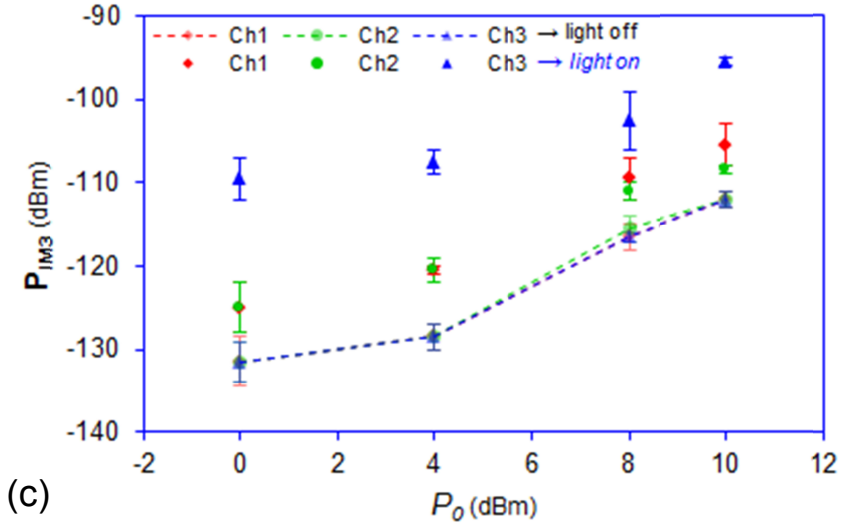
Ch1 Ch2 Ch3 → light off
Ch1 Ch2 Ch3 → light on
P_{IM3} (dBm)
P_0 (dBm)

(c)

Figure 6.24. Wirelessly measured P_{IM3} for the three channels versus P_0 for V_m = 7 mV_{pp}, when external light is supplied at (a) λ_{ch1} ~ 650 nm to target activation of channel 1 (red), (b) λ_{ch2} ~ 530 nm to target activation of channel 2 (green), and (c) λ_{ch3} ~ 430 nm to target activation of channel 3 (blue). Dashed curves represent P_{IM3} measured without any light turned on. Solid curves indicate P_{IM3} with a single band of light (eg. in (a), λ_{ch1} ~ 650 nm) turned on. The plots reveal that ch-ch isolation is not equal to on-off isolation (e.g. in (a), solid curve, representing light at λ_{ch1}, of off channels 2 and 3 are higher than dashed curve, representing no light, for same) as the spectral purity of the light source and filter embedded optical switches are imperfect and inevitably causes activation of unpaired channels intended for operation at alternate wavelengths. By removing the interference between optical bands, ch-ch isolation will increase and ideally equal on-off isolation.

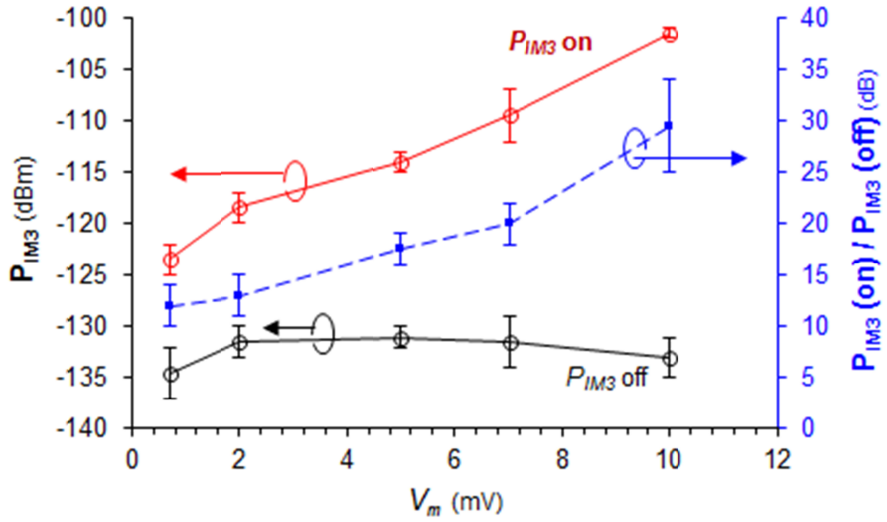

Figure 6.25. Wirelessly measured P_{IM3} (left y-axis) and on-off isolation (right y-axis) versus V_m for optimal P_0 and wireless separation. On and off P_{IM3} for a single channel for a given input V_m was measured with and without light. The plot reveals maximum

channel to channel isolation that can be expected if the spectral bandwidths of optical channels are purified (ie. infinite out of band rejection of filter embedded optical switches along with corresponding external light sources). On-off isolation is seen to decrease for lower V_m, and this is most likely due to the P_{IM3} falling to noise floor level, which limits the resolving of lower P_{IM3}.

Table 6.2. Measured specifications for wireless multichannel neurorecording

Footprint	Overall dimensions	*50×28 mm²*
	Antenna	*50×5 mm²*
	Photodiodes	*50×23 mm²*
Detected neuropotentials (V_m)	Bandwidth (f_m)	*5 – 1000 Hz*
	Amplitude (V_m)	*≥ 700 μV_{pp}*
	Distance	*≤ 38 mm*
Wireless RF		
LO transmission	Radiated power (P_0)	*0 – 12 dBm*
	Frequency (f_0)	*2.45 GHz*
RF reception	Backscattered harmonic (P_{IM3})	*-127 – -91 dBm*
	Min. detectable signal (SNR ≥ 10 dB)	*≥ -127 dBm*
	Noise floor	*~ -137 dBm*
	Frequency (f_{RF})	*~ 4.9 GHz*
	Read distance	*38 mm*
Wireless optical		
Light supplied	Illuminance (LED array output per specs)	*100 – 800 lm*
	Dominant wavelengths (λ_{ch1}, λ_{ch2}, λ_{ch3})	*650, 530, 430 nm*
Incident light	Irradiance (incident upon PD array)	*Not measured*
Multichannel functionality	On – off isolation	*10 – 35 dB*
	Ch – ch selectivity	*6 – 25 dB*

CHAPTER 7

CHALLENGES, LIMITATIONS, AND MITIGATIONS

7.1. Single channel neurorecording

At present, the neurorecording microsystem possesses an inadequately low sensitivity as the minimum level neuropotential that can be wirelessly resolved is limited to ~ 500 μV_{pp}, while cortically derived potentials and the targeted sensitivity, range V_m ~ 10 – 1000 μV_{pp}. There are several possible directions to approach in augmenting the sensitivity of the backscattering system so that the fully passive microsystem is practically employable in brain recording. Evidently, the task of improving overall SNR may be tackled by improvements either at the implant and/or the external interrogator. As the implant is fully passive, on-chip amplification and processing circuit functionality conventionally implemented to increase SNR are intentionally excluded. As will be seen, efforts must be shifted to suppress noise, mainly residing at the external interrogator.

Enhancements at the implant microsystem stage mainly rely on the mixing performance of the integrated varactors to produce strong intermodulation products ($2f_0 \pm f_m$), the antenna efficiency to increase SNR, and/or the noise associated with the implant circuit. The latter instance may readily be disregarded as the circuit targets primarily reactive circuit functions and the resistive elements are limited to the antenna, possessing few Ohms of resistance, and the biological tissue and electrode interface, for which lie beyond practical control or maneuverability. For the former case, it is expected, based on theory (equation 3.3), that varactors operating at lower threshold voltages (lower V_j), lower C_j, and/or higher γ would augment the magnitude of third order harmonics for a given input V_m. For a junction based diode, V_j is identified with the built-

in potential, and is inherently defined by the concentration of donors and acceptors in the semiconductor material (V_j (Si) ~ 0.7 V, V_j (Ge) ~ 0.3 V, V_j (GaAs) ~ 1.3 V). For a Schottky diode, the barrier height (V_j) is controlled by the doping characteristics of the interface between the metal contact and semiconductor substrate. C_j is circumscribed by the dimensions of the diode's depletion region ($C = \varepsilon A/d$, where d is gap between positive and negative terminals) that forms a capacitive dielectric under reverse bias. C_j is often difficult to lower in practice because of emerging parallel fringe capacitances that tend to eclipse C_j. γ is controlled by the vertical grading characteristics of the doping structure introduced into the substrate that will form the depletion region. As will be explained further, γ is difficult to model in the application of the fully passive harmonic mixing system. The MA46H120 varactor diodes used in the current circuit possessed the optimal specifications of, C_j = 1.1 pF and $0.9 < \gamma < 1.1$, for a flip-chip package, at the time. At present, only a few new varactor diodes have been made commercially available that seem to possess potentially higher γ and lower C_j and V_j (eg. DMK2790 and SMS7621 by Skyworks and MA46H500 series by MA/COM). However, the parameters advertised by the manufacturers may be deceiving since C_j, γ, and all of the diode's parasitics that will significantly impact its operation in the fully passive circuit, vary as a function of frequency and bias. Furthermore, γ fluctuates considerably at lower bias levels and is not accurately represented in its form as a constant value in describing the voltage variable capacitance (equation 3.1) that ultimately accounts for all the nonlinear output products targeted in the fully passive circuit (equations 3.2 – 3.3). Commercially specified parameters are usually listed for more traditional applications and each diode is generally manufactured for application specific parameters. Advertised component

specification data and available spice models do not accurately depict the multi-faceted and variable characteristics of the diodes to the extent required for simulating its use in the fully passive circuit. For example, for tuning and VCO applications, varactor γ is displayed for large voltage ranges beginning at discrete levels impractical for the fully passive application where operation bias is near zero volts. Spice models provided by the manufacturers are produced by fitting a model to their measurements that fail to include the variations at the low voltage levels employed in the fully passive circuit. Nevertheless, by customizing selection of optimal varactor parameters through in-house characterization and generation of more accurate models for targeted harmonic mixing operations, improvements may be made to overall sensitivity in the fully passive circuit. Alternatively, thin-film ferroelectric varactors (eg. BST (Barium Strontium Titanite) may also be explored in substitution of conventional semiconductor varactor diodes. Ferroelectrics display higher nonlinearity near the zero voltage bias with decreasing film thickness (Yngvesson, Schaubert, Korzeniowski, Kollberg, Thungren, & Johansson, 1985) (Vorobiev, Rundqvist, Khamchane, & Gevorgian, 2003), and can moreover, be monolithically integrated with the current neurorecording microsystem, eliminating the need for all off-chip components. In summary, implant based enhancements do not require any changes of the extremely simple circuit, but require optimization of the intrinsic semiconductor properties of mounted or monolithically integrated nonlinear elements that form the basis of fully passive harmonic recording mixing operations. Due to the projected enormity of investment required for both routes (fabrication and semiconductor characterization studies of custom made varactors), sensitivity augmentation via the implant circuit was not pursued in this study. The antenna may be

modified to display a greater real part of impedance to increase radiation efficiency as well as a positive imaginary part (inductive) of impedance to conjugate match to the capacitive varactor mixer and reduce mismatch losses. Reconfigured planar slot antennas have been shown to produce these preferred characteristics by varying the shape and size of the aperture slots in the metal plane (Marrocco, 2007) and could be readily implemented to increase the microsystem antenna backscatter gain and overall SNR. Another area that may be explored is parametric amplification inherent to varactor mixers, which ideally can produce a positive conversion gain for inputted fundamental signals if pumped with a high enough magnitude carrier power (Lee & Afshari, 2011).

On the other hand, the external interrogator possesses greater flexibility for optimization in contrast to the limited degrees of freedom for the implant circuit, burdened by its intended fully passive quality. One of the major drawbacks of the current interrogator is its inherent noise and coupling of noise that collectively veil and screen out the targeted low level backscattered signals carrying neuropotential data. The major contributors to overall noise are: i) noise originating from interrogator components, ii) phase noise of the supplied carrier (LO@f_0), and iii) externally coupled noise, as illustrated in Figure 7.1. Interrogator components and the external environment impact the integrity of the wirelessly transmitted signals and determine the maximum achievable SNR.

Front-end interrogator components include low noise amplifiers (LNA's), filters, etc., that manifest a cascade of noise properties impacting overall SNR. Overall noise figure ($F_{1\text{-}n}$) of the cascaded components may be calculated by Equation 4.1 (chapter 4.1). Individual noise figures are deduced by the thermal noise characteristics of an individual

component, $N=kT_o\Delta f$ (chapter 4.1). Based on theoretical models the minimum necessary signal power of the backscattered signal received by the antenna may be estimated given the input referred noise power spectral density ($N_i=FkT_0$). The current interrogator (F_1=2.4 dB) possesses an estimated N_i = 0.623 nV/√Hz, or equivalently, -141 dBm noise floor for a bandwidth of 1 kHz. Substituting enhanced front-end LNA ($F_1 \leq$0.4dB) may further reduce N_i to 0.478 nV/√Hz, or equivalently, -144 dBm. This ~ 3 dB improvement is only moderate and therefore other noise sources must be tackled.

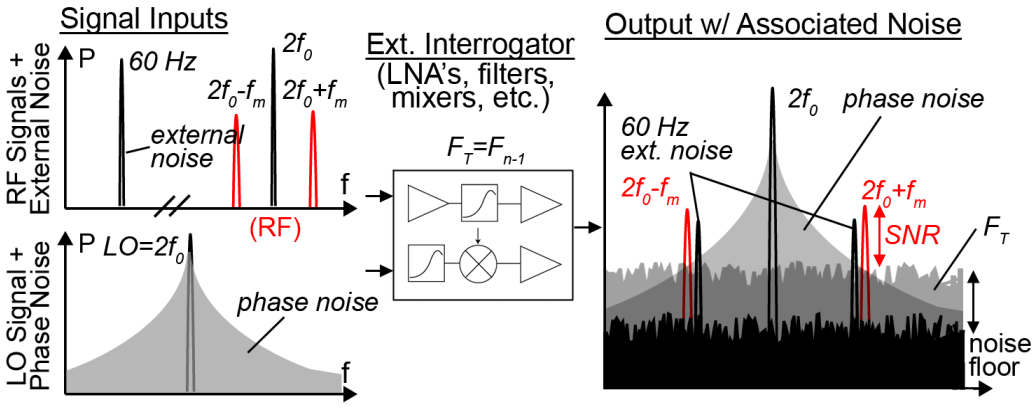

Figure 7.1. Illustration of various noise sources (60 Hz noise, phase noise, noise associated with interrogator components) and their impact on the overall SNR. All these noise sources coupled together to lower SNR; yet the phase noise is likely a dominant noise source as the target neuropotential signal (f_m) is at low frequency (up to 10 kHz) compared to the high frequency carrier (f_o) (2.45 GHz). By reducing phase noise, SNR may be improved.

Phase noise originating from the signal generator is the primary limiting factor on maximum achievable SNR. As depicted in Figure 7.1, phase noise trailing the desired LO

is reciprocally mixed and inconveniently expressed at the neural implant and external interrogator, raising overall noise. The present interrogator uses a signal generator with a phase noise of -75 dBc/Hz (at a 1 kHz offset). The phase noise is further exacerbated during amplification and/or frequency doubling for supplying the reference for downconversion. Instead, oscillators with -100 to -130 dBc/Hz (at 1 kHz) noise, available commercially, may be utilized to drastically reduce LO noise impact. An equivalent noise figure (F_{eq}) due to phase noise may be estimated based on preliminary data (section 3.4). The power of the suppressed $2f_0$ LO at the downconverting mixer is a minimum of -75 dBm, that along with its phase noise, results in an equivalent apparent noise figure of F_{eq} = 24 dB, illustrating ~ 21 dB increase in noise compared to noise solely from interrogator components or an equivalent N_i of 7.071 nV/√Hz. Reverse calculations show that phase noise ≤ -99 dBc/Hz is required to suppress noise contributions of the LO below overall $F_{1\text{-}n}$ of the interrogator components. Removing phase noise components effectively translates to about 125x reduction in background noise, depicting the dominating impact of phase noise especially given the narrow bandwidths of neuropotentials (Δf < 1 kHz). Although one may optimistically scale the current threshold voltage of 500 μV_{pp} to 4 μV_{pp} given this reduction of noise, unfortunately the power of the internal neuropotentials does not directly scale with the LO power received by the external interrogator. Wireless path loss ($e^{-\alpha R}$) in the tissue medium, implant antenna gains (G_t and G_r), and varactor mixer conversion loss ($G_{2\omega}$) must be taken into account. Data from benchtop wireless measurements using mV-level neuropotentials (V_m) were used to empirically estimate the combined $G_tG_re^{-\alpha R}$ and $G_{2\omega}$ losses. Based on measured data, an interrogator with an

enhanced N_i of 0.487 nV/√Hz and bandwidth of 1 kHz, produces a minimum detectable signal (MDS) of $V_m \sim 15$ μV for a wireless distance of 1 cm.

Moreover, receive sensitivity is agitated by external coupling of background noise originating from power supplies (60 Hz) and environmental noise. External noise is a pervasive interference for all modern electronics, but is a strong factor in the present fully passive system as any low level background noise may be easily introduced into the demodulator and present itself as harmonic inputs into the nonlinear components and interfere with the targeted third order harmonics. However, housing of all external interrogator components into an isolated and customized demodulator circuit board may drastically suppress such interference.

Alternatively, it may also be feasible to attempt RF backscattering and harmonic mixing targeted at modulating the fundamental or second-order intermodulation (IM2) products (ie. $f_0 \pm f_m$) rather than those modulating the 2nd harmonic of the fundamental or IM3 products by reducing carrier power (P_0) saturation effects and phase noise issues surrounding these former mixing products. P_0 saturation may be relieved by incorporating carrier leakage suppression or cancellation techniques at the external interrogator front-end by directly coupling an out-of-phase carrier, as utilized for sensitive radar or RFID systems (Jung, Park, & Yeom, 2012). It may be possible to cancel out the phase noise almost entirely as generated by the carrier by mixing and downconverting with an in-phase coherent carrier as wirelessly supplied.

It may be understood that the extent to which the external interrogator must be further improvised correlates directly to the tradeoff between implant circuit complexity based on the simple fully passive scheme to this external sub-system that corresponds to

improving safety and reliability of the more critical implant component. As a result, this dramatic reassigning of circuit complexity towards the external system permits greater safety of the implant by preserving its fully passive qualities.

7.2. Multimodal multichannel neurorecording

The fully passive multichannel neurorecording work discussed in this thesis is not ready for implementation in real brains due to its large size (50 mm x 28 mm) and its low sensitivity (minimum detectable $V_m \sim 0.7$ mV_{pp}). Furthermore, the current prototype is designed to record from only 3 sites, which is far less than practical requirements and in-use (Borton, Yin, Aceros, & Nurmikko, 2013) and commercially available wireless neurorecording systems possessing > 200 channels (Triangle Biosystems International, 2013). In spite of these limitations, the multichannel neurorecording work possesses an extensive capacity for improvement and channel expansion. A large part of the limitations observed in the current prototype were anticipated as assigned to its targeted basic aims as a wireless proof of concept of supplementing optical multichannel operations onto the original fully passive single channel recorder and its intent to demonstrate functionality for wireless operation in air.

Of prevalent concern is the technical constraint in wireless optical illumination and activation of the multiple channels *in situ*, as embedded inside several manifold layers of brain tissue, bone, and skin. Biological tissue largely absorbs and scatters irradiated light at the wavelengths of practical interest (~ 300 – 2000 nm) resulting in shallow penetration of light and most of the light being attenuated before reaching targeted cortical brain tissue strata containing the recording implant device (Eggert &

Blazek, 1987) (Bashkatov, Genina, Kochubey, & Tuchen, 2006) (Meglinski & Matcher, 2002). Nevertheless, due to ever-increasing implementation of optical interrogation techniques for studying brain wiring in animals (Fenno & Deisseroth, 2014) and in brain surgery (Eggert & Blazek, 1987), optically transparent windows have been developed to safely channel light to the relevant cerebral stratum while deterring the enfolding dissipative and reflective tissue layers (Wang, Zhang, Xu, Luo, & Zhu, 2012). These biocompatible optically transparent materials may also be employed for fully passive multichannel recording of cortical neuropotentials to easily direct externally illuminated light switching modalities.

Another challenge is the impedance presented by the circuit from the electrodes in this diode mixing scheme, where the input resistance of the forward-biased diodes lies on the order of 100s – 1000s of Ohm, in contrast to that of the varactor mixer possessing ideally an open circuit impedance ~ few MOhm. This will present voltage division of the inputted neuropotentials derived by high impedance microelectrodes (eg. penetrating MEA recording probes) displaying > 10 - 100 kOhm resistance (at 1 kHz) (Prasad & Sanchez, 2012). This mismatch would lower the neuropotential voltage across the mixer diode and that is inputted to mix and produce third order harmonics. On the other hand, these low port impedance circuits may be suitable for collecting neuropotentials from low impedance electrodes such as ECoG and other types of surface or large area electrodes. A finite resistance associated with the electrode impedance was taken into account in multichannel simulations and testing by adding a ~ 5kOhm resistor in series with the emulated neuropotential voltage source.

Miniaturization towards an implantable form may be realized by monolithic integration and fabrication of the entire backscattering fully passive multichannel unit (Figure 7.2). Both basic diode and optical switches (photodiode) may be fabricated on-chip through use of foundry services. The ability to construct very small (on the order of tens of microns) and highly responsive photodiodes is exemplified by those dies produced by commercial vendors (TrueLight Corp., 2011) (Cosemi Tech., 2012). For expanding the number of recording channels, narrowband optical filters may be directly fabricated onto the photodiode switches. These narrowband filters may be in the form of Fabry Perot interference filters that are a simple construct of alternating thin films of different refractive indices (Magnusson & Wang, 1995) (Wang & Magnusson, 1994) (Semrock, 2014) (Melles Griot, 2014) (Ocean Optics, 2014). Efficient methods of fabricating a single arrayed filter having up to 256 geometrically separated spectral bands (which would correspond to 256 recording channels) through the use of only 8 photolithography masks have been recently demonstrated (Correia, Bartek, & Wolffenbuttel, 2000). Serial, near real time, acquisition of multiple recording sites is achieved by sweeping corresponding bands of light for sequential on-chip channel activation using an off shelf tunable high-speed swept light sources (Axsun, 2013) (Santec, 2014) that operate in the 0.9 – 1.4 μm band and have low FWHM (full width half maximum) to automatize the multichannel acquisition operations.

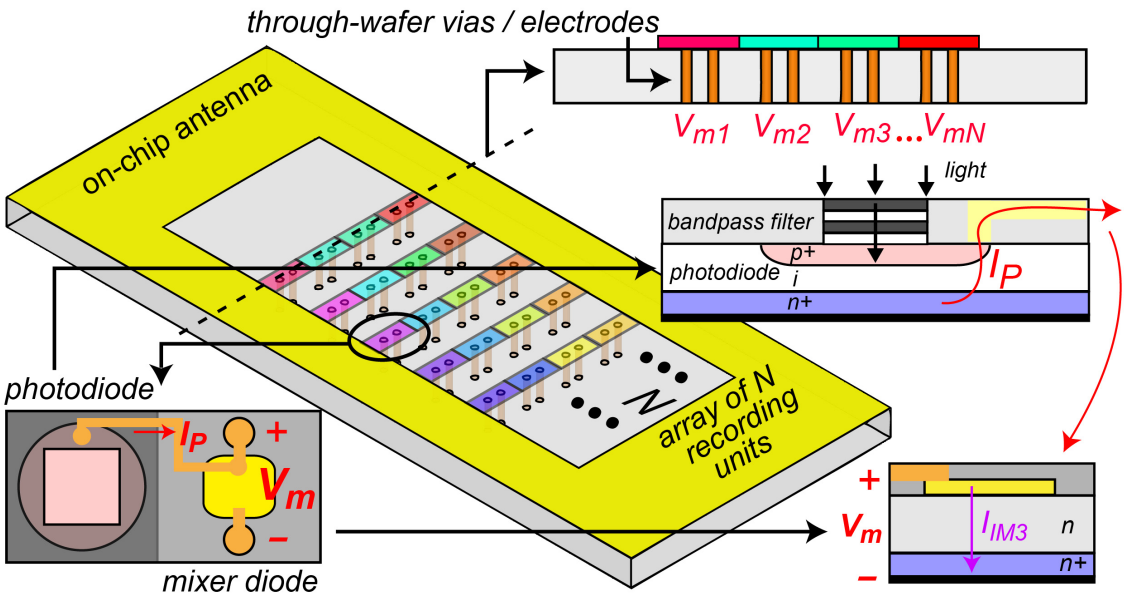

Figure 7.2. Envisioned single chip wireless fully passive multichannel neurorecording implant. A series of multichannel recording units are integrated on a single chip and share a single antenna for RF backscattering of neuropotential signals. Each channel is equipped with an optical filter embedded photodiode, mixer diode, and the recording electrodes. The photodiodes and mixer diodes are formed by p-n junctions and metal/n-type Schottky configurations, respectively. Externally supplied wavelength-specific light passes through the filter to activate underlying photodiodes and generate the photo-bias current (I_p), which is fed directly to the mixer diode of the same channel to passively generate IM3 current containing mixed neuropotentials collected from the recording electrodes. The IM3 intermodulation products are wirelessly backscattered to the external interrogator (not shown in the figure) to acquire multiple channels of neuropotential signals.

CHAPTER 8

CONCLUSION

This thesis described work on fully passive systems for wireless telemetry of brain signals (i.e. neuropotentials). These fully passive devices are envisaged as chronic brain implantable tags that allow for remote monitoring of the electrophysiological signals (i.e. neuropotentials) generated by neurons in the brain. The fully passive wireless telemetry of neuropotentials is afforded by employing RF backscattering mechanisms in conjunction with the inherent nonlinear properties of diodes. Design and computational models were used to analyze and optimize wireless backscattering and neurorecording performance and finalize structural layout of the single channel wireless neurorecording microsystem (chapter 2). The single channel device contains only 2 varactor diodes, and monolithically integrated antenna and capacitors, within a physical implant viable footprint of $12 \times 4 \times 0.5$ mm^3 as manufactured using standard microfabrication procedures (chapter 3). Measured results demonstrate the ability of the system to wirelessly record neuropotentials as low as hundreds of *microvolts* and operate at distances of few *centimeters* to the external receiver (chapter 4 and 6). Wireless measurements were also carried out using real neuropotentials generated by the sciatic nerve of a frog, demonstrating the fully passive recorder's efficacy for use in peripheral nervous systems, and in a human-head mimicking phantom to measure backscattering performance in a physiologically relevant dissipative wireless medium (chapter 4). Safety of the implanted microsystem was substantiated through computational and measured analysis of brain tissue absorbed wirelessly induced EM power in the form of SAR (chapter 5). Furthermore, the ability to incorporate multichannel functionality (to acquire

neuropotentials from multiple spatially separate sites of the brain), while preserving its fully passive features, was also demonstrated, in simulation and actual fabrication and measurement, by integration of light sensitive and selective switches (chapter 6). The fully passive microsystem's limited sensitivity (few hundreds of *microvolts* to few *millivolts*) may be insufficient for recording targeted real extracellular potentials in the brain that have amplitudes as low as tens of *microvolts*. Nevertheless, a number of possible remedies exist to improve the sensitivity for practical acquisition of cerebral neuropotentials (section 7.1). In addition, methods to increase number of recording channels while scaling down the overall footprint of the implant were discussed in section 7.2. Despite the limited functionality afforded by the fully passive implant, in its present form, over state of art wireless neurorecording technology, the fully passive system reveals a number of clear benefits useful for long term chronic use as a brain implantable device. The fully passive approach potentially provides enhanced safety and reliability over current wireless recording systems with respect to its negligible heat dissipation (by means of its fully passive classification connoting no power regulation or supply or related elements, and its near lack of resistive heat generating elements) and its innate simplicity (by means of its very small amount of circuit components – a few diodes and capacitors along with the wireless antenna link for the single channel recorder).

In spite of the formidable advantages presented by the fully passive approach, its practical application in its eventually optimized implant form may still be largely constrained due to its limited functionality as confined by its fully passive nature. That is, the system, by its fully passive nature, lacks the modular processing capabilities to

contain the variety of more sophisticated operations of current state of art recorders, such as, hybrid stimulation, spike sorting, algorithmic detection schemes, etc. (Song, et al., 2009) (Nurmikko, et al., 2010). Nonetheless, as was done with the multichannel integration (chapter 6) by means of introducing external light modalities to externalize control of multiple channels, the ability to supplement additional functions may be realized by adopting externally configurable on-chip elements. Furthermore, the actual clinical manifestation of any neurorecording system should ultimately be decided by aligning the specific medical needs to the functional as well as safety specifications of the individual system. In consequence, the fully passive system may relieve a few of the shortcomings present in current state of art and find application in areas that fervently require long term safety and reliability while necessitating only simple wireless acquisition of raw neuropotentials. One feasible application of the fully passive single channel recording microsystem may be in epilepsy detection to record large ictal activity patterns in the form of LFPs from the cortex associated with an oncoming seizure event. Such systems have been manufactured to record these ictal events from the surface with large electrodes and/or deeper brain layers with penetrating macroscopic electrodes similar to deep brain stimulation systems (Morrell & Skarpaas, 2009). These devices are in the phase of clinical trials, but still contain the risks of intracranial wiring that are used to physically wire and connect subcranially recorded signals to an extracranial battery powered circuit. The fully passive recording microsystem of this work may readily provide the ability to detect and record the LFP waveforms coinciding with seizure onset, as these manifest larger amplitudes (up to 5 mV) than the microelectrode derived neuropotentials (tens to hundreds of microvolts), and relieve the patient from the inherent

risks associated with intracranial tethering. As such, the fully passive system may provide the longer term safety and reliability aspects due to its simple structure (Constantinescu, 2003) and removal of wiring, which is an essential requirement for human application.

REFERENCES

Abbaspour-Tamijani, A., Farooqui, M., Towe, B. C., & Chae, J. (2008, August). A miniature fully-passive microwave back-scattering device for short-range telemetry of neural potentials. *30th Annual International Conference of the IEEE EMBS* (pp. 129-132). Vancouver, Canada: IEEE/EMBS.

Applied fMRI Institute. (2010, April 10). *News and Photos*. Retrieved April 10, 2010, from http://www.appliedfrmi.org/news_photos.html

Association, A. (2013). 2013 Alzheimer's Disease Facts and Figures. *Alzheimer's and Dementia, 9*(2), 1-71.

Axsun. (2013). *Axsun*. Retrieved March 14, 2014, from OCT Swept Laser Engines: http://axsun.com/products/oct-swept-lasers.php

Balanis, C. A. (1989). *Advanced Engineering Electromagnetics.* Hoboken, NJ, USA: John Wiley and Sons.

Balanis, C. A. (2005). *Antenna Theory: Analysis and Design.* Hoboken, NJ: John Wiley and Sons.

Bashkatov, A. N., Genina, E. A., Kochubey, V. I., & Tuchen, V. V. (2006). Optical properties of human cranial bone in the spectral range from 800 to 2000 nm. *Proceedings of SPIE, 6163*, 1-11.

Bauer, R. J., Cohn, M., Cotton, J. M., & Packard, R. F. (1966, April). Millimeter wave semiconductor diode detectors, mixers, and frequency multipliers. *Proceedings of the IEEE, 54*(4), 595-605.

Biopac Systems, I. (2010). *CAP100C EEG Electrode Cap Kit with Accessories*. Retrieved April 10, 2010, from CAP100C EEG Electrode Cap Kit with Accessories: http://www.electodesales.com/cap100c.html

Blount, J. P., Cormier, J., Kim, H., Kankirawatana, P., Riley, K. O., & Knowlton, R. C. (2008, September). Advances in intracranial monitoring. *Neurosurgery Focus, 25*(3), 1-8.

Booth, J. C., Ono, R. H., Takeuchi, I., & Chang, K. (2002, July). Microwave frequency tuning and harmonic generation in ferroelectric thin film transmission lines. *Applied Physics Letters, 81*(4), 718-720.

Borton, D. A., Yin, M., Aceros, J., & Nurmikko, A. (2013, February). An implantable wireless neural interface for recording cortical circuit dynamics in moving primates. *Journal of Neural Engineering, 10*, 1-16.

Chen, H., Wu, J., Hyland, B., Lu, X., & Chen, J. J. (2008, May). A low noise remotely controllable wireless telemtry system for single-unit recording in rats navigating in a vertical maze. *Medical and Biological Engineering and Computing, 46*, 883-839.

Chestek, C. A., Gilja, V., Nuyujukian, P., Kier, R. J., Solzbacher, F., Ryu, S. I., et al. (2009, August). HermesC: low-power wireless neural recording system for freely moving primates. *IEEE Transactions on Neural Systems and Rehabilitation Engineering, 17*(4), 330-338.

Cole, K. S., & Cole, R. H. (1941, April). Dispersion and absorption in dielectrics. *Journal of Chemical Phyics, 9*, 341-352.

Constantinescu, C. (2003). Trends and challenges in VLSI circuit reliability. *IEEE Micro Magazine*, 14-19.

Correia, J., Bartek, M., & Wolffenbuttel, R. F. (2000, March). High-selectivity single-chip spectrometer in silicon for operation at visible part of the spectrum. *IEEE Transactions on Electron Devices, 47*(3), 553-559.

Cosemi Tech. (2012). *Cosemi*. Retrieved March 18, 2014, from Bare Die Products: https://www.cosemi.com/Product/Bare-Die-Products

Eggert, H. R., & Blazek, V. (1987). Optical properties of the human brain tissue, meninges, and brain tumors in the spectral range of 200 - 900 nm. *Neurosurgery, 21*(4), 459-464.

Fenno, L. E., & Deisseroth, K. (2014). Neocortical circuit interrogation with optogenetics. *Optical Imaging of Neocortical Dynamics, 85*, 175-188.

Fonseca, M. A., Allen, M. G., Kroh, J., & White, J. (2006, June). Flexible wireless passive pressure sensors for biomedical applications. *Solid-State Sensors, Actuators, and Microsystems Workshop* (pp. 37-42). Hilton Head, SC: TRF.

Gabriel, C., & Gabriel, S. (1996). *Compilation of the dielectric properties of body tissues at RF and microwave frequencies.* Report for Armstrong Laboratory (AFMC), Occupational and Environmental Health Directorate, Radiofrequency Radiation Division, Texas.

Galejs, J. (1969). *Antenas in Inhomogenous Media.* London, Great Britain: Pergamon Press.

Guy, A. W. (2000, November). Analyses of electromagnetic fields induced in biological tissues by thermographic studies on equivalent phantom models. *IEEE Transactions on Microwave Theory and Techniques, 48*(1), 2094-2103.

Harrington, R. F. (1960, January). Effect of antenna size on gain, bandwidth, and efficiency. *Journal of Research of the National Bureau of Standards - D, Radio Propagation, 64D*(1), 1-12.

Harrison, R. R. (2008, July). Design of integrated circuits to observe brain activity. *IEEE Proceedings, 96*(7), 1203-1216.

Harrison, R. R., Kier, R. J., Chestek, C. A., Gilja, V., Nuyujukian, P., Ryu, S., et al. (2009, August). Wireless neural recording with single low-power integrated circuit. *IEEE Transactions on Neural Systems and Rehabilitation Engineering, 17*(4), 322-328.

Harrison, R. R., Watkins, P. T., Kier, R. J., Lovejoy, R. O., Black, D. J., Greger, B., et al. (2007, January). A low-power integrated circuit for a wireless 100-electrode neural recording system. *IEEE Journal of Solid-State Circuits, 42*, 123-133.

Hatsopoulos, N. G., & Donoghue, J. P. (2009, July). The science of neural interface systems. *Annual Review of Neuroscience, 32*, 249 - 266.

Hedderly, D. L. (1962, June). An analysis of a circuit for the generation of high-order harmonics using an ideal nonlinear capacitor. *IRE Transactions on Electron Devices*, 484-491.

Ho, M., Chen, H., Tseng, F., Yeh, S., & Lu, M. S. (2007, January). CMOS micromachined probes by die-level fabrication for exracellular neural recording. *Journal of Micromechanics and Microengineering, 17*, 283-290.

Hochberg, L. R., Serruya, M. D., Friehs, G. M., Mukand, J. A., Saleh, M., Capaln, A. H., et al. (2006, June). Neuronal ensemble control of prosthetic devices by a human with tetraplegia. *Nature, 442*, 164-171.

Hochberg, L., Bacher, D., Jarosiewicz, B., Masse, N., Simeral, J., Vogel, J., et al. (2012). Reach and grasp by people with tetraplegia using a neurally controlled robotic arm . *Nature, 485*(7398), 372-375.

Holleman, J., Yeager, D. J., Prasad, R., Smith, J. R., & Otis, B. (2008, November). NeuralWISP: a wirelessly powered neural interface with 1-m range. *Biomedical Circuits and Systems Conference* (pp. 37-40). Baltimore, MD: IEEE.

Honig, W. (1965, November 16). *Patent No. 3218638*. USA.

Hossmann, K. -A., & Hermann, D. M. (2003, January). Effects of electromagnetic radiation of mobile phones on the central nervous system. *Bioelectromagnetics, 24*(1), 49-62.

Hu, S. Y., Ko, J., & Coldren, L. A. (1997). Resonant-cavity InGaAs/InAlGaAs/InP photodetector arrays for wavelength demultiplexing applications. *Applied Physics Letters, 70*, 2347.

Huang, F. -J., Lee, C. -M., Chang, C. -L., Chen, L. -K., Yo, T. -C., & Luo, C. -H. (2011, July). Rectenna application of miniaturized implantable antenna design for triple-band biotelemetry communication. *IEEE Transactions on Antennas and Propagation, 59*(7), 2646-2653.

International Commission on Non-Ionizing Radiation Protection. (1998). Guidelines for limiting exposure to time-varying electric, magnetic, and electromagnetic fields (up to 300 GHz). *Health Physics, 74*(4), 494-522.

Ito, K., Furuya, K., Okano, Y., & Hamada, L. (2001). Development and characteristics of a biological tissue-equivalent phantom for microwaves. *Electronics and Communications in Japan, 84*(4), 1126-1135.

Janaswamy, R., Schaubert, D. H., & Pozar, D. M. (1986, September). Analysis of the transverse electromagnetic mode linearly tapered slot antenna. *Radio Science, 21*(5), 797-804.

Jung, J.-Y., Park, C.-W., & Yeom, K.-W. (2012, May). A Novel carrier leakage suppression front-end for UHF RFID reader. *IEEE Transactions on Microwave Theory and Techniques, 60*(5), 1468-1477.

Katsuki, R., Fujita, T., Liu, T., Nakatsuka, T., Nakashima, M., & Kumamoto, E. (2006, August). Tramadol, but not its major metabolite depresses compound actional potentials in frog sciatic nerves. *British Journal of Pharmacology, 149*, 319-327.

Kelley, G. R. (2011). *Parkinson's Disease Incidence and Prevalence.*

Kim, S., Bhandari, R., Klein, M., Negi, S., Rieth, L., Tathireddy, P., et al. (2009, December). Integrated wireles neural interface based on the Utah electrode array. *Biomedical Microdevices, 11*, 453-466.

Kim, S., Tathireddy, R. A., Normann, R. A., & Solzbacher, F. (2007, December). Thermal impact of an active 3-d microelectrode array implanted in the brain. *IEEE Transactions on Neural Systems and Rehabilitation Engineering, 15*(4), 493-501.

Kipke, D. R., W, S., Buzsaki, G., Fetz, E., Henderson, J. M., Hetke, J. F., et al. (2008, November). Advanced neurotechnologies for chronic neural interfaces: new horizons and clinical opportunities. *Journal of Neuroscience, 28*(46), 11830-11838.

LaManna, J. C., McCracken, K. A., Patil, M., & Prohaska, O. J. (1989). Stimulus-activated changes in brain tissue temperature in the anesthetized rat. *Metabolic Brain Disease, 4*, 225-237.

Lee, W., & Afshari, E. (2011, March). Low-noise parametric resonant amplifier. *IEEE Transactions on Circuits and Systems-I: Regular Papers, 58*(3), 479-492.

Leuthardt, E. C., Schalk, G., Wolpaw, J. R., Ojemann, J. G., & Moran, D. W. (2004, June). A brain-computer interface using electrocorticographic signals in humans. *Journal of Neural Engineering, 1*(2), 63-71.

Maas, S. A. (2003). *Nonlinear Microwave and RF Circuits.* Norwood, MA: Artech House.

Magnusson, R., & Wang, S. S. (1995, December). Transmission bandpass guided-move resonance filters. *Applied Optics, 34*(35), 8106-8109.

Marin, C., & Fernandez, E. (2010, May). Biocompatibility of intracortical microelectrodes: current status and future prospects. *Frontiers in Neuroengineering, 3*(8), 1-6.

Marrocco, G. (2007, June). RFID antennas for the UHF remote monitoring of human subjects. *IEEE Transactions on Antennas and Propagation, 55*(6), 1862-1870.

Means, D. L., & Chan, K. W. (2001). *Evaluating compliance with FCC guidelines for human exposure to radiofrequency electromagnetic fields.* Federal Communications Commission Office of Engineering and Technology OET. Federal Communications Commission Office of Engineering and Technology OET.

Meglinski, I. V., & Matcher, S. J. (2002, October). Quantitative assessment of skin layers absorption and skin reflectance spectra simulation in the visible and near-infrared spectral regions. *Physiological Measurement, 23*, 741-753.

Melles Griot. (2014). *Melles Griot*. Retrieved March 11, 2014, from Products: http://www.mellesgriot.com/products/Overview

Merli, F., Bolomey, L., Zurcher, J. -F., Corradini, G., Meurville, E., & Skriveryik, A. K. (2011, October). Design, realization, and measurements of a miniature antenna for implantable wireless communication systems. *IEEE Transactions on Antennas and Propagation, 59*(10), 3544-3555.

Messenger, G. C., & McCoy, C. T. (1957, June). Theory and operation of crystal diodes as mixers. *Proceedings of the IRE*, 1269-1283.

Minas, G., Wolfenbuttel, R. F., & Correla, J. H. (2006). An array of highly selective Fabry-Perot optical channels for biological fluid analysis by optical absorption

using a white light source for illumination. *Journal of Optics A: Pure and Applied Optics, 8*, 272-278.

Morrell, M., & Skarpaas, T. L. (2009, April). Intracranial stimulation therapy for epilepsy. *Neurotherapeutics: The Journal of the American Society for Experimental NeuroTherapeutics, 6*, 238-243.

Nair, D. R. (2008). Chronic subdural electrodes in the management of epilepsy. *Clinical Neurophysiology, 119*, 11-28.

Nicolelis, M. (2008). *Methods for neural ensemble recordings (2nd ed.).* CRC Press.

Nikitin, P. V., & Rao, K. V. (2006, December). Theory and measurement of backscattering from RFID tags. *IEEE Antennas and Propagation Magazine, 48*(6), 212-218.

Nurmikko, A., Donoghue, J., Hochberg, L., Patterson, W., Song, Y.-K., Bull, C., et al. (2010, March). Listening to Brain Microcircuits for Interfacing With External World—Progress in Wireless Implantable Microelectronic Neuroengineering Devices. *Proceedings of the IEEE, 98*(3), 375-388.

Ocean Optics. (2014). *Ocean Optics*. Retrieved March 14, 2014, from Light Sources: http://www.oceanoptics.com/Products/lightsources.asp

Okano, Y., Ito, K., Ida, I., & Takahashi, M. (2000, November). The SAR evaluation method by a combination of thermographic experiments and biological tissue-equivalent phantom. *IEEE Transactions on Microwave Theory and Techniques, 48*(1), 2094-2103.

Penttila, K., Keskilammi, M., Sydanheimo, L., & Kivikoski, M. (2006, February). Radar cross-section analysis for passive RFID systems. *IEEE Proceedings on Microwave Antennas and Propagation, 153*(1), 103-109.

Perlin, G. E., & Wise, K. D. (2009, January). Ultra-compact integration for fully-pasive implantable neural microsystems. *22nd International Conference on Micro Electro Mechanical Systems* (pp. 228-231). Sorrento, Italy: IEEE.

Poon, A. S., O'Driscoll, S., & Meng, T. H. (2010, May). Optimal Frequency for Wireless Power Transmission Into Dispersive Tissue . *IEEE Transactions on Antennas and Propagation, 58*(5), 1739-1750.

Prasad, A., & Sanchez, J. C. (2012, March). Quantifying long-term microelectrode array functionality using chronic in vivo impedance testing. *Journal of Neural Engineering, 9*, 1-12.

Riistama, J., Aittokallio, E., Verho, J., & Lekkala, J. (2009, December). Totally passive wireless biopotential measurement sensor by utilizing inductively coupled resonance circuits. *Sensors and Actuators A: Physical, 157*, 313-321.

Rizk, M., Bossetti, C. A., Jochum, T. A., Callender, S. H., Nicolelis, M. A., Turner, D. A., et al. (2009, March). A fully-implantable 96-channel neural data acquisition system. *Journal of Neural Engineering, 6*, 1-14.

Roland, J., Brunner, P., Johnston, J., Schalk, G., & Leuthardt, E. C. (2010). Passive real-time identification of speech and motor cortex during awake craniotomy. *Epilepsy and Behavior, 18*, 123-128.

Roland, J., Miller, K., Freundenberg, Z., Sharma, M., Smyth, M., Gaona, C., et al. (2011). The effect of age on human motor electrocorticographic signals and implications for brain–computer interface applications. *Journal of Neural Engineering, 8*, 1-10.

Salam, M. T., Sawan, M., & Nguyen, D. K. (2010, September). Low-power implantable device for onset detection and subsequent treatment of epileptic seiqures: a review. *Journal of Healthcare Engineering, 1*, 169-184.

Santec. (2014). *Santec*. Retrieved March 14, 2014, from Swept Test System: http://www.santec.com/en/products/instruments/tunablelaser/sts-510

Schwerdt, H. N., Bristol, R. E., & Chae, J. (2014, March). Miniaturized passive hydrogel check valve for hydrocephalus treatment. *IEEE Transactions on Biomedical Engineering, 61*(3), 814-820.

Schwerdt, H. N., Bristol, R., & Chae, J. (2012, June). Hydrogel check valve with non-zero cracking pressure for use as a potential alternative hydrocephalus treatment method. *Solid-State Sensors, Actuators, and Microsystems Workshop* (pp. 137-140). Hilton Head Island, SC: TRF.

Schwerdt, H. N., Chae, J., & Miranda, F. A. (2012, July). Wireless performance of a fully passive neurorecording microsystem embedded in dispersive human head phantom. *IEEE International Symposium on Antennas and Propagation (APSURSI)* (pp. 1-2). Chicago, IL: IEEE.

Schwerdt, H. N., Miranda, F. A., & Chae, J. (2012, June). A fully passive wireless backscattering neuro-recording microsystem embedded in dispersive human head medium. *IEEE Electron Device Letters, 33*(6), 908-910.

Schwerdt, H. N., Miranda, F. A., & Chae, J. (2013, May). Analysis of electromagnetic fields induced in operation of a wireless fully passive backscattering neurorecording microsystem in emulated human head tissue. *IEEE Transactions on Microwave Theory and Techniques, 61*(5), 2170-2176.

Schwerdt, H. N., Xu, W., Shekhar, S., Abbaspour-Tamijani, A., Towe, B., & Chae, J. (2010, June). A Fully-Passive Wireless Microfabricated Neuro-Recorder. *Solid-State Sensors, Actuators, and Microsytems Workshop* (pp. 258-259). Hilton Head Island, SC: TRF.

Schwerdt, H. N., Xu, W., Shekhar, S., Abbaspour-Tamijani, A., Towe, B., Miranda, F., et al. (2011, October). A fully-passive wireless microsystem for recording of neuropotentials using RF backscattering methods. *IEEE/ASME Journal of Microelectromechanical Systems, 20*(5), 1119-1130.

Schwerdt, H. N., Xu, W., Shekhar, S., Miranda, F., & Chae, J. (2011, June). Preliminary Thermal Characterization of a Fully-Passive Wireless Backscattering MEMS Neuro-Recorder. *International Conference on Solid-State Sensors and Actuators (Transducers)* (pp. 1228-1231). Beijing, China: IEEE .

Semrock. (2014). *Semrock*. Retrieved March 14, 2014, from Semrock Products: http://www.semrock.com/Products.aspx

Sodagar, A. M., Perlin, G. E., Yao, Y., Najafi, K., & Wise, K. D. (2009, September). An Implantable 64-Channel Wireless Microsystem for Single-Unit Neural Recording. *IEEE Journal of Solid State Circuits, 44*(9), 2591-2604.

Sodagar, A. M., Perlin, G. E., Yao, Y., Wise, K. D., & Najafi, K. (2007, June). An implantable microsystem for wireless multi-channel cortical recording. *International Solid-State Sensors, Actuators, and Microsystems Conference* (pp. 69-72). Lyon, France: IEEE.

Sodagar, A. M., Wise, K. D., & Najafi, K. (2007, June). A fully integrated mixed-signal neural processor for implantable multichannel cortical recording. *IEEE Transactions on Biomedical Engineering, 54*(6), 1075-1088.

Song, Y. K., Borton, D. A., Park, S., Patterson, W. R., Bull, C. W., Laiwalla, F., et al. (2009, June). Active microelectronic neurosensor arrays for implantable brain communication interfaces. *IEEE Transactions in Neural Systems and Rehabilitation Engineering, 17*(4), 339-345.

Towe, B. C. (2007, May). Passive backscatter biotelemetry for neural interfacing. *3rd International Conference in Neural Engineering* (pp. 144-147). Honolulu: IEEE/EMBS.

Triangle Biosystems International. (2013). *Triangle Biosystems*. Retrieved March 10, 2014, from Products: http://www.trianglebiosystems.com/products.html

TrueLight Corp. (2011). *TrueLight Corporation*. Retrieved March 14, 2014, from Products: http://www.truelight.com.tw/en/products/Products.aspx

Vidal, N., & Lopez, J. M. (2010, August). Changes in electromagnetic field absorption in the presence of subcutaneous implanted devices: minimizing increases in absorption. *IEEE Transactions on Electromagnetic Computations, 52*(3), 545-555.

Vorobiev, A., Rundqvist, P., Khamchane, K., & Gevorgian, S. (2003, October). Silion substrate integrated high Q-factor parallel-plate ferroelectric varactors for microwave/millimeter wave applications. *Applied Physics Letters, 83*(15), 3144-3146.

Wang, J., Zhang, Y., Xu, T. H., Luo, Q. M., & Zhu, D. (2012, March). An innovative transparent cranial window based on skull optical clearing . *Laser Physics Letters, 9*(6), 469-473.

Wang, S. S., & Magnusson, R. (1994, June). Design of waveguide-grating filters with symmetrical line shapes and low sidebands. *Optics Letters, 19*(12), 919-921.

Wansch, R. (2001, December). Smal antennas for wireless micro-systems. *Active and Passive Electronic Components, 25*, 71-82.

Ward, M. P., Rajdev, P., Ellison, C., & Irazoqui, P. P. (2009, May). Towards a comparison of microelectrodes for acute and chronic recordings. *Brain Research, 1282*, 183-200.

Waziri, A., Schevon, C. A., Cappell, J., Emerson, R. G., McKhann, G. M., & Goodman, R. R. (2009, March). Initial surgical experience with a dense cortical microarray in epileptic patients undergoing craniotomy for subdural electrode implantation. *Neurosurgery, 64*(3), 540-545.

Wheeler, H. A. (1947, March). Fundamental limitations of small antennas. *IEEE Proceedings of the Institute of Radio Engineers*, 1479-1484.

Wise, K. D., Sodagar, A. M., Yao, Y., Gulari, M. N., Perlin, G. E., & Najafi, K. (2008, July). Microelectrodes, microelectronics, and implantable neural microsystems. *IEEE Proceedings, 96*(7), 1184-1202.

Wisneski, K. J., Anderson, N., Schalk, G., Smyth, M., Moran, D., & Leuthardt, E. C. (2008, November). Advanced neurotechnologies for chronic neural interfaces: new horizons and clinical opportunities. *Stroke, 39*(12), 3351-3359.

Yngvesson, K. S., Schaubert, D. H., Korzeniowski, T. L., Kollberg, E. L., Thungren, T., & Johansson, J. F. (1985). Endfire tapered slot antennas on dielectric substrates. *IEEE Transactions on Antennas and Propagation, 33*(12), 1392-1400.